Southern Illinois University Carbondale
OpenSIUC

Dissertations Theses and Dissertations

12-1-2014

TOMOGRAPHIC IMAGE RECONSTRUCTION: IMPLEMENTATION, OPTIMIZATION AND COMPARISON IN DIGITAL BREAST TOMOSYNTHESIS

Shiyu Xu
Southern Illinois University Carbondale, shiyu.xu@gmail.com

Follow this and additional works at: http://opensiuc.lib.siu.edu/dissertations

Recommended Citation

Xu, Shiyu, "TOMOGRAPHIC IMAGE RECONSTRUCTION: IMPLEMENTATION, OPTIMIZATION AND COMPARISON IN DIGITAL BREAST TOMOSYNTHESIS" (2014). *Dissertations.* Paper 979.

This Open Access Dissertation is brought to you for free and open access by the Theses and Dissertations at OpenSIUC. It has been accepted for inclusion in Dissertations by an authorized administrator of OpenSIUC. For more information, please contact opensiuc@lib.siu.edu.

TOMOGRAPHIC IMAGE RECONSTRUCTION: IMPLEMENTATION, OPTIMIZATION AND COMPARISON IN DIGITAL BREAST TOMOSYNTHESIS

by

Shiyu Xu

B.S., Beihang University, 2004
M.S., Florida Internation University, 2008
M.S., Beihang University, 2009

A Dissertation
Submitted in Partial Fulfillment of the Requirements for the
Doctor of Philosophy Degree

Department of Electrical and Computer Engineering
in the Graduate School
Southern Illinois University Carbondale
December 2014

DISSERTATION APPROVAL

TOMOGRAPHIC IMAGE RECONSTRUCTION: IMPLEMENTATION,
OPTIMIZATION AND COMPARISON IN DIGITAL BREAST TOMOSYNTHESIS

By

Shiyu Xu

A Dissertation Submitted in Partial

Fulfillment of the Requirements

for the Degree of

Doctor of Philosophy

in the field of Electrical and Computer Engineering

Approved by:

Dr. Henri Schurz

Dr. Lalit Gupta

Dr. Spyros Tragoudas

Dr. Shaikh S. Ahmed

Dr. Ying Chen, Chair

Graduate School
Southern Illinois University Carbondale
7th October 2014

AN ABSTRACT OF THE DISSERTATION OF

Shiyu Xu, for the Doctor of Philosophy degree in Electrical and Computer Engineering, presented on 7th October 2014, at Southern Illinois University Carbondale.

TITLE: TOMOGRAPHIC IMAGE RECONSTRUCTION: IMPLEMENTATION, OPTIMIZATION AND COMPARISON IN DIGITAL BREAST TOMOSYNTHESIS

MAJOR PROFESSOR: Dr. Ying Chen

Conventional 2D mammography was the most effective approach to detecting early stage breast cancer in the past decades of years. Tomosynthetic breast imaging is a potentially more valuable 3D technique for breast cancer detection. The limitations of current tomosynthesis systems include a longer scanning time than a conventional digital X-ray modality and a low spatial resolution due to the movement of the single X-ray source. Dr. Otto Zhou's group proposed the concept of stationary digital breast tomosynthesis (s-DBT) using a Carbon Nano-Tube (CNT) based X-ray source array. Instead of mechanically moving a single X-ray tube, s-DBT applies a stationary X-ray source array, which generates X-ray beams from different view angles by electronically activating the individual source prepositioned at the corresponding view angle, therefore eliminating the focal spot motion blurring from sources. The scanning speed is determined only by the detector readout time and the number of sources regardless of the angular coverage spans, such that the blur from patient's motion can be reduced due to the quick scan. S-DBT is potentially a promising modality to improve the early breast cancer detection by providing decent image quality with fast scan and low radiation dose.

DBT system acquires a limited number of noisy 2D projections over a limited angular range and then mathematically reconstructs a 3D breast. 3D reconstruction is faced with the challenges of cone-beam and flat-panel geometry, highly incomplete sampling and huge reconstructed volume. In this research, we investigated several representative reconstruction methods such as Filtered backprojection method (FBP), Simultaneous algebraic reconstruction technique (SART) and Maximum likelihood (ML). We also compared our proposed statistical iterative reconstruction (IR) with particular prior and computational technique to these representative methods. Of all available reconstruction methods in this research, our proposed statistical IR appears particularly promising since it provides the flexibility of accurate physical noise modeling and geometric system description. In the following chapters, we present multiple key techniques of statistical IR to tomosynthesis imaging data to demonstrate significant image quality improvement over conventional techniques. These techniques include the physical modeling with a local voxel-pair based prior with the flexibility in its parameters to fine-tune image quality, the pre-computed parameter κ incorporated with the prior to remove the data dependence and to achieve a predictable resolution property, an effective ray-driven technique to compute the forward and backprojection and an over-sampled ray-driven method to perform high resolution reconstruction with a practical region of interest (ROI) technique. In addition, to solve the estimation problem with a fast computation, we also present a semi-quantitative method to optimize the relaxation parameter in a relaxed order-subsets framework and an optimization transfer based algorithm framework which potentially allows less iterations to achieve an acceptable convergence.

The phantom data is acquired with the s-DBT prototype system to assess the performance of these particular techniques and compare our proposed method to those representatives. The value of IR is demonstrated in improving the detectability of low contrast and tiny micro-calcification, in reducing cross plane artifacts, in improving resolution and lowering noise in reconstructed images. In particular, noise power spectrum analysis (NPS) indicates a superior noise spectral property of our proposed statistical IR, especially in the high frequency range. With the decent noise property, statistical IR also provides a remarkable reconstruction MTF in general and in different areas within

a focus plane. Although computational load remains a significant challenge for practical development, combined with the advancing computational techniques such as graphic computing, the superior image quality provided by statistical IR will be realized to benefit the diagnostics in real clinical applications.

ACKNOWLEDGMENTS

I would like to thank Dr. Ying Chen for her invaluable assistance and insights leading to the research project, in particular for her great support, encouragement and helps for my research and career. My sincere thanks also goes to all my other committee members including Dr. Henri Schurz, Dr. Lalit Gupta, Dr. Spyros Tragoudas and Dr. Shaikh S. Ahmed, for their patience and understanding during the four years of effort that went into the production of this paper.

I greatly appreciate our lab collaborators at the University of North Carolina. Dr. Otto Zhou and Dr. Jianping Lu provided me great comments to conduct my experiments and analyze the results.

A special thanks also to Dr. Debashish Pal and Dr. Guangzhi Cao in the CT system and advanced algorithm at GE Healthcare. As my mentors when I was interning at GE healthcare, they broadened my perspectives and enriched my academic background, which is extremely helpful in my research.

Lastly, I would like to bring my personal thanks to brothers and sisters in church, my parents, and my wife Qing Wu, for their unchangeable love and care.

TABLE OF CONTENTS

Abstract ii

Acknowledgments v

List of Tables ix

List of Figures x

1 Introduction 1

- 1.1 Clinical Motivation 1
- 1.2 Conventional mammography and limitations 2
- 1.3 Digital Breast Tomosynthesis 4
- 1.4 State-of-art stationary Digital Breast Tomosynthesis 6
- 1.5 Image reconstruction and computation 8

2 Implementation of representative reconstruction methods in digital breast tomosynthesis 13

- 2.1 Deterministic reconstruction methods 14
  - 2.1.1 Filtered backprojection reconstruction 15
  - 2.1.2 Algebraic reconstruction technique 17
- 2.2 Statistical iterative reconstruction 20
  - 2.2.1 Maximum likelihood reconstruction 20

3 Modeling of statistical iterative reconstruction 25

- 3.1 Statistical model for image reconstruction 25
- 3.2 Geometric configuration and forward and backprojection model 27
- 3.3 ROI reconstruction with super resolution 30

4 A pre-computed backprojection based Modified regularization 35

- 4.1 Method for characterizing the smoothing parameter λ 35
  - 4.1.1 Pixel property 37
  - 4.1.2 Noise property 38

4.2 Simulation experiments 40
4.3 Phantom experience 43
4.4 Discussion 48
5 Parameter optimization of generalized Gaussian Markov Random Field regularization 52
5.1 Comparison study of selected parameters 52
5.2 Image reconstruction with breast phantom 54
5.3 Discussion 57
6 Method for the parameter optimization of ordered subsets (OS) separable parabolic surrogate algorithm (SPS) 58
6.1 Algorithm of OS method 58
6.2 Semi-quantitative optimization on a simulated phantom 60
6.3 Simulation experiments 66
6.4 Discussion 72
7 Local convergence analysis of the optimization transfer and successively over-relaxation optimization transfer 73
7.1 Optimization transfer 73
7.2 Convergence rate analysis 74
7.3 Alternative optimization transfer 79
    7.3.1 Adaptive successively over-relaxation 81
    7.3.2 Constant successively over-relaxation 82
7.4 Simulation experiments 83
7.5 Phantom study 87
7.6 Discussion 88
8 Image quality assessment 90
8.1 System description 90
8.2 Reconstructions for comparison study 90

8.3 Improvement in detectability 93
8.4 Performance for in-plane resolution/noise trade-offs 99
8.5 Reduction of cross-plane artifacts 100
8.6 Noise power spectrum analysis 101
8.7 Modulation Transfer Function (MTF) 106
  8.7.1 System MTF 107
  8.7.2 Relative reconstruction MTF 108
9 Conclusions and Discussions 115
Vita 129

LIST OF TABLES

4.1 Half Width of $\frac{2}{3}$ Magnitude of MTF versus λ 47

4.2 Standard deviation versus λ 48

5.1 CNR and in-plane MTF for SIR-ρ-OT with selected parameter combinations . 53

8.1 Comparison of noise, CNR and in-plane MTF for SIR-ρ-OT and the reference methods 101

LIST OF FIGURES

1.1 A typical geometric configuration of the s-DBT system. 7

2.1 Sampling density calculation in spatial frequency domain. 16

3.1 Influence function of the gGMRF regularizer with different parameters. 27

3.2 DBT imaging system: (a) front view; (b) side view. 28

3.3 Ray-driven model: (a) ray-driven forward model; (b) ray-driven backprojection model. 29

3.4 Ray-driven forward model for voxel and sub-voxel: (a) ray-driven model for voxel; (b) ray-driven model for sub-voxel; (c) over-sampled ray-driven model for sub-voxel. 33

3.5 A circular mask, which is formed by projecting the ROI boundary along the ray beam, indicates the minimum data set required to reconstruct the voxels in ROI. 34

4.1 Geometric configuration of Digital Breast Tomosynthesis with multiple parallel X-ray beams. 41

4.2 Average MTF of the focus plane reconstructed by the PL method with a basic quadratic penalty from the projections with a uniform incident value of $y_i = 1$ 42

4.3 Average MTF of the focus plane reconstructed by PPL method from the projections with a non-uniform incident value with $y_i \gg 1$ 43

4.4 Standard deviation of the focus plane reconstructed by the PL method with a basic quadratic penalty from the projections with a expected incident value of $\theta_i = 1$ 44

4.5 Standard deviation of the focus plane reconstructed by PPL method from the projections with a expected incident value of $\theta_i \gg 1$ 45

4.6 FOVs of PPL 46

4.7 FOVs of MLEM 46

4.8 FOVs of FBP 46
4.9 FOVs of SART 46
4.10 Comparison of ASFs reconstructed by SART, MLEM and PPL 49
4.11 Comparison of normalized PSFs reconstructed by SART, MLEM and PPL . . 50
5.1 Pixel precision measured along micro-calcification on a focus plane reconstructed by SIR-ρ-OT with selected parameter combinations. (a) shows PSF curves; (c) shows MTF curves 53
5.2 Measurement of PSF and CNR. (a) demonstrates the micro-calcification which is used to measure PSF; (b) shows a mass object and its background to calculate CNR 54
5.3 Reconstructed mass between our proposed methods with various parameter choices and some representative methods. (a) FBP (b) statistical IR with $p = 1.8, c^p = 2$ (c) statistical IR with $p = 1.61, c^p = 3.5$ (d) statistical IR with quadratic regularization (e) OS-EM (f) SART 56
5.4 Reconstructed micro-calcification between our proposed methods with various parameter choices and some representative methods. (a) FBP (b) statistical IR with $p = 1.8, c^p = 2$ (c) statistical IR with $p = 1.61, c^p = 3.5$ (d) statistical IR with quadratic regularization (e) OS-EM (f) SART 56
6.1 Objective function as a function of iteration with OS-PPL-λ16 62
6.2 Comparisons of noise versus contrast with iteration increasing between OS-PPL and representative methods 63
6.3 Comparisons of ASF between OS-PPL with 15 iterations and representative methods 64
6.4 Comparisons of ASF between OS-PPL with 20 iterations and representative methods 65
6.5 relaxed OS-PPL-λ16-sub25-r12 reconstruction on the focus plane at the height of $35mm$. 67

6.6 FBP reconstruction on the focus plane at the height of $35mm$. 68

6.7 relaxed OS-SPS reconstruction with $\lambda = 100000$ weighting a quadratic penalty on the focus plane at the height of $35mm$. 69

6.8 relaxed OS-MLEM reconstruction the focus plane at the height of $35mm$. . . . 70

6.9 Comparisons of noise versus contrast between OS-PPL and representative methods on the testing phantom. 71

7.1 Geometry configuration of Digital Breast Tomosynthesis with multiple parallel X-ray beams. 84

7.2 Comparisons of the objective functions of PC-SPS and proposed TCR. 85

7.3 Comparisons of the objective functions of OS-blended PC-SPS and OS-blended TCR. 86

7.4 ROIs with ρ-OT with 5 iterations 88

7.5 ROIs with PC-SPS with 8 iterations 88

8.1 A focus plane reconstructed by FBP 92

8.2 A focus plane reconstructed by OS-EM 93

8.3 A focus plane reconstructed by SIR-ρ-OT 94

8.4 A focus plane reconstructed by SART 95

8.5 Comparison of micro-calcification in mass reconstructed by different methods. (a) shows results reconstructed by FBP; (b) shows results reconstructed by SIR-ρ-OT; (c) shows results reconstructed by OS-EM; (d) shows results reconstructed by SART; 96

8.6 Comparison of fibrils in mass reconstructed by different methods. (a) shows results reconstructed by FBP; (b) shows results reconstructed by SIR-ρ-OT; (c) shows results reconstructed by OS-EM; (d) shows results reconstructed by SART; 98

8.7 Zoomed focus plane with a mass and several granular micro-calcifications. (a) shows results reconstructed by SIR-ρ-OT with low resolution; (b) shows results reconstructed by SIR-ρ-OT with high resolution; (c) shows results reconstructed by FBP; 99

8.8 Zoomed focus plane with a circular mass and six tiny micro-calcifications. (a) shows results reconstructed by SIR-ρ-OT with low resolution; (b) shows results reconstructed by SIR-ρ-OT with high resolution; (c) shows results reconstructed by FBP; 99

8.9 In-plane MTF measured along micro-calcification on a focus plane reconstructed by SIR-ρ-OT, FBP, SART and OS-EM 100

8.10 Comparison of ASF curves of the selected mass in the results reconstructed by FBP, SIR-ρ-OT, OS-EM and SART. 102

8.11 Comparison of ASF curves of the selected micro-calcifications in the results reconstructed by FBP, SIR-ρ-OT, OS-EM and SART. 103

8.12 A reconstructed plane for NPS measurement 105

8.13 Mean-subtracted NPS analysis for different reconstruction methods 106

8.14 Projection MTF of the stationary Digital Breast Tomosynthesis 107

8.15 Regions of simulated impulses for relative reconstruction MTF 108

8.16 Normalized reconstruction MTF for the entire focus-plane along V direction . 110

8.17 Normalized reconstruction MTF for the entire focus-plane along U direction . 111

8.18 Normalized reconstruction MTF for the chest wall area along V direction . . . 112

8.19 Normalized reconstruction MTF for the central column area along V direction 113

8.20 Normalized reconstruction MTF for the far-away chest wall area along V direction 114

CHAPTER 1

INTRODUCTION

1.1 CLINICAL MOTIVATION

Breast cancer is the second most common type of cancer in women and the second leading cause of cancer-related deaths among women [76]. One in eight women in the United States will develop breast cancer during her lifetime [16]. Approximately 200,000 women in the United States are diagnosed with breast cancer each year, and the disease causes about 40,000 deaths annually [16]. X-ray mammography is currently the most effective method of detecting early stage breast cancer, and has played an important role in reducing the breast cancer rate. It has been shown that the use of screening mammography has reduced mortality from breast cancer by $20\% - 40\%$ [30, 31].

Breast cancer is the result of DNA damage or mutation that leads to uncontrolled cell proliferation. However, the actual etiology remains poorly understood and it is impossible to foresee who will develop breast cancer [49]. Based on the severity, breast cancer is ranged from 0 to IV [13]. How well the patients could be cured after being treated for breast cancer depends on many factors. Generally, the more advanced stage the cancer is, the poorer healed the patients could be. For women with stage I, II, or III breast cancer, the main goal is to heal the cancer and keep it from returning. For women with stage IV cancer, the goal is to improve symptoms and help them live longer. In most cases, stage IV breast cancer cannot be cured. The 5-year survival rate refers to the number of patients who live at least 5 years after their cancer is found in report [76]. According to it, the 5-year survival rates for persons with breast cancer who are appropriately healed are as follows: (1) 93% for Stage 0; (2) 88% for Stage I; (3) 81% for Stage IIA; (4) 74% for Stage IIB; (5) 67% for Stage IIIA; (6) 41% for Stage IIIB; (7) 49% for Stage IIIC; (7) 15% for Stage IV.

Therefore, early detection is viewed as the best hope to decrease breast cancer mortality by allowing intervention at earlier stage of cancer progression [6, 98, 64]. Improving breast technologies may permit breast cancer to be detected at a smaller size and earlier stage, hence reducing the number of women who die each year from the cancer. Thus, tremendous efforts have been made in the incremental improvements in imaging technologies in the field of breast cancer detection.

1.2 CONVENTIONAL MAMMOGRAPHY AND LIMITATIONS

Conventional mammography is a two-dimensional (2D) breast imaging method relying on a pair of 2D x-ray images of the breast, which are obtained from two different directions: top-to-bottom and side-to-side. The breast is pulled away from the body, and compressed between two plastic plates. In regular screen film mammography, two x-ray views for each breast are recorded on film. It is suggested that screen-film mammography is and will continue to be a valuable tool for detection and diagnosis of breast cancer [98]. However, screen-film mammography has some limitations on displaying the finest features due to inadequate contrast, therefore resulting in a limited sensitivity for the detection of breast cancer with dense breast [64]. Film does not have a linear sensitivity to photon-flux [73], there is a narrow range over which it can detect small difference in contrast. Also film requires processing time and storage space. Another limitation is the effect of structural noise due to film granularity, degrading the visibility of microcalcifications and other fine breast structures [98]. These limitations can be effectively overcome with a digital mammography system.

In digital mammography these two views of images (from top to bottom and from side to side) are recorded on a high-resolution digital detector whose size is about the same as a film-screen cassette (18cm 24cm or 24cm 30cm). With digital mammography, a electronic x-ray detector is used to record the breast image and to convert the image into a digital picture. After the digital mammogram is stored on a computer, it can be processed and displayed on a soft copy or hard copy device. One advantage of digital mammography is that its digital form allows the radiologist to alter the range and contrast of the image while viewing. Also, digital mammograms lend themselves to processing by Computer Aided Detection (CAD) systems that act to assist the radiologist in making diagnosis. The studies by Pisano et al. [64] suggested that the overall diagnostic accuracy of digital and film mammography for breast cancer was similar, but digital mammography is more accurate in a sub-population of women with dense breasts. The improved performance in a digital mammography system is mainly associated with the x-ray detector and the display device. Therefore, despite the convenience of digital images obtained with digital mammography, and despite the superior performance of a digital detector, its clinical diagnostic efficacy is only a slight improvement on that obtained with conventional screen-film systems. Mammographic features characteristic of breast cancer are masses, particularly ones with irregular margins [14], clusters of microcalcifications, and architectural distortions of breast structures. In conventional 2D mammography using either screen film or digital detectors, the cancer lesions present in one plane of the three-dimensional (3D) breast are sometimes difficult to visualize because of confounding anatomical structures in planes of above and below the one of interest. A major limitation in conventional mammographic technique is that superimposed normal breast tissues generate a structure noise that obscures the breast cancer, especially in a dense breast, increasing the false-negative rate. Even without other sources of radiation or instrumentation noise, a cancer can be hidden by the anatomical background. It is this structure noise also termed anatomical variability that accounts for the only slight advantage of digital mammography over screen-film in spite of the superior detector performance of digital mammography. It has been shown that 30% of breast cancer may be missed by conventional (digital and screen-film) mammography [60]. On the other hand, the overlapped tissue structures may look like a cancerous tumor on a mammogram, and can be mistaken for abnormalities, causing false-positive callbacks for further diagnosis or even biopsy. In 2004, National Cancer Institute reported that up to 12% normal breasts were mistakenly read as having breast cancer.

1.3 DIGITAL BREAST TOMOSYNTHESIS

Compared with traditional 2D mammography, three-dimensional (3D) digital breast tomosynthesis (DBT) imaging system [23, 22, 17, 102] have the potential to improve conspicuity of structures by removing the visual clutter associated with overlying anatomy. The mammographic tomosynthesis reconstruction methods make it possible to distinguish the cancer from its overlying breast tissues, even for the problematic dense breast cases. This may prove to be greatly helpful in enabling better detection of breast cancer.

Attempts to developing 3D imaging methods to separate objects from overlying anatomical structure go back to the early 20th century [23]. In 1917, Radon introduced the famous Radon transformation of tomography, describing the mathematics of generating internal object planes from twodimensional projection data [67]. In 1932, Ziedses des Plantes led the pioneering effort in conventional linear tomography and Ernest Twining contributed to its clinical prominence [23]. Early tomography systems utilized a linear, opposing motion of the xray tube and the film receptor to generate a focal plane. The procedure had to be repeated if more than one focal plane was needed. This led to high dose to the patients. Secondly, the modality was not capable of sufficiently suppressing outofplane blur [23]. In 1969, Garrison et al. developed a prototype "three dimensional roentgenography" device [23, 39] which was the first full implementation of Ziedses des Plantess concepts. Two years later, Miller et al. published their own discrete tomography results, which they called "photographic laminography" [57]. In 1972, D.G. Grant reported a prototype three-dimensional image projector based on circular image acquisition geometry [40]. Grant also named the new circular backprojection device "tomosynthesis," referring to the capability to retroactively create an infinite number of arbitrary tomograms [23]. More improvements were achieved after Grant and Millers work to speed up the filmbased tomosynthesis procedure time, including coded-aperture imaging [48, 41], also known as “short time tomosynthesis”, ”flashing tomosynthesis (FTS)” [59, 79], and “tomoscopy” [72]. In the late 1960s, fluoroscopic tomography was implemented successfully [52]. Researchers began to use fluoroscopic devices to acquire discrete projection images and stored them in individual video channels for postacquisition electronic tomosynthesis reconstruction [5]. Finally, in the late 1990s, the advent of digital xray acquisition technology made it possible to acquire a series of lowdose projection images from different locations of an xray source to provide the depth information for tomosynthesis reconstruction [23, 18, 79].

Recently, many healthcare manufacturers are actively developing digital breast tomosynthesis devices. Most of current DBT prototype system designs re-utilize the conventional mammography design with associated mechanical, electrical and sensor techniques [62]. The X-ray tube typically rotates along an a prescribed path above a fixed flat-panel detector to acquire projection images at specified positions with limited view angle and limited view number. This kind of design is called as partial iso-centric. The typical total angular range of breast tomosynthesis imaging is less than 50°, and the number of projection images is limited under 49 for a low total dosage of radiation. Because the sampling is highly incomplete, the depth resolution is limited. Therefore, tomosynthesis does not produce the isotropic spatial resolution achievable with Computed Tomography (CT). However, due to the usage of cone-beam X-ray and flat panel detector, the resolution of a transversely reconstructed plane is often superior to CT [22]. In addition to DBT, tomosynthesis has been applied to a wide variety of clinical applications over the years, which includes dental imaging, angiography, and imaging of the chest and bones. In February 2011, the USA FDA approved Hologic, Inc. to market its Selenia Dimensions 2D Full Field Digital Mammography (FFDM) and Digital Breast Tomosynthesis (DBT) system. This DBT system has been the first commercially available mammography system that provides 3D images of the breast for breast cancer screening and diagnosis.

In 2014, a comparison study [38] using Tomosynthesis in Combination with Digital Mammography was led by Sarah M. Friedewald, MD of the Caldwell Breast Center, Advocate Lutheran General Hospital in Park Ridge, Illinois . A total of 454,850 examinations (281,187 conventional mammograms compared to 173,663 3D Tomosynthesis exams) were included in the study. Significant findings include: (1) 41% increase in the detection of invasive breast cancers. ($p < .001$) (2) 29% increase in the detection of all breast cancers. ($p < .001$) (3) 15% decrease in women recalled for additional imaging. ($p < .001$) (4) 49% increase in Positive Predictive Value (PPV) for a recall (The PPV for a recall increased from 4.3 to 6.4%). ($p < .001$) (5) 21% increase in PPV for biopsy (The PPV for a breast biopsy increased from 24.2 to 29.2%). ($p < .001$) (6) No significant change in the detection of ductal carcinoma in situ (DCIS).

1.4 STATE-OF-ART STATIONARY DIGITAL BREAST TOMOSYNTHESIS

The limitations of current tomosynthesis systems include a longer scanning time than a conventional digital X-ray modality and a low spatial resolution. Both result from the limitations of the current X-ray tube technology where a single X-ray tube is mounted on a rotating gantry and moves along an arc above objects over a certain angular range. Image blur due to both source movement and patient motion is a major factor degrading the spatial resolution. For a continuous tube motion design, the higher the scanning speed, the larger the distance the X-ray tube travels during a fixed exposure time and the larger the X-ray focal spot blurring. In addition, longer time scanning will increase the probability of motion blur from patients. The amount of blur which can be tolerated limits the scanning speed and angular coverage.

To conquer the limitations, literature [65, 82] proposed the concept of stationary digital breast tomosynthesis (s-DBT) using a Carbon Nano-Tube (CNT) based X-ray source array. Instead of mechanically moving a single X-ray tube, s-DBT applies a sta-

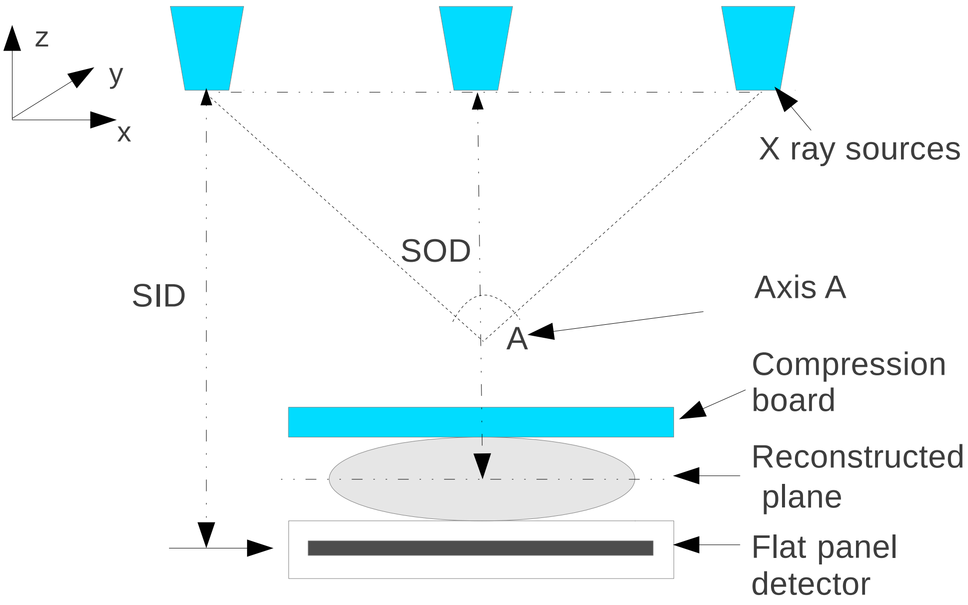

Figure 1.1. A typical geometric configuration of the s-DBT system.

tionary X-ray source array, which generates X-ray beams from different view angles by electronically activating the individual source prepositioned at the corresponding view angle, therefore eliminating the focal spot motion blurring from sources. The scanning speed is determined only by the detector readout time and the number of sources regardless of the angular coverage spans, such that the blur from patient's motion can be reduced due to the quick scan. More importantly, the spatially distributed multi-beam X-ray sources also enable the potentials to improve image qualities by wide varieties of flexible distributions of the multi-beam sources [5].

Fig. 1.1 illustrates the geometric configuration of s-DBT. Multiple X-ray sources are distributed at the locations where view angles are equal to each other corresponding to Axis A. The whole source array appears in a straight line parallel to the detector. Trigger signals are used to activate each X-ray source one by one to acquire the whole projection dataset. Thereby no X-ray tubes motion is required. Source to image distance (SID) denotes the perpendicular distance between X-ray source and detector surface. Source to object distance (SOD) indicates the perpendicular distance between the X-ray source and the center of the breast which stays compressed between the compression board and the air gap above the detector. The transversal planes are reconstructed to represent the 3D breast volume.

1.5 IMAGE RECONSTRUCTION AND COMPUTATION

Among current reconstruction techniques in tomographic imaging, both analytical reconstructions and iterative reconstruction (IR) are being studied and applied. One classical analytical reconstruction is Filtered Back Projection (FBP)[83] based on Fourier theorem, which guarantees a precise signal reconstruction at a sampling rate satisfying Nyquist-Shannon Theorem, but it will introduce reconstruction error from highly incomplete frequency information [15]. To mitigate the reconstruction error, several revised versions of FBP such as FBP with post-processing and FBP with modified ramp filter [101] were proposed. One of the IRs in tomographic reconstruction is Simultaneous Algebraic Reconstruction Technique (SART) [4, 3] which applies a Ordered Subsets (OS) method to solve a unweighted least square model, which may lead to over-fitting to the noisy data and artifacts from low dose measurement and non-convergence to the global optimal. Signal statistics in X-ray Computed Tomography (CT) follows Poisson distribution for mono-energetic CT and compound Poisson for polyenergetic CT [84, 25]. Statistical IR such as Maximum Likelihood (ML) was proposed. The problem of ML reconstruction is usually ill posed [10]. The likelihood alone rarely determines a satisfactory solution and the image reconstructed from ML is very noisy. Thus, it is necessary to regularize the solution by imposing a prior or regularization, such as Maximum a posterior (MAP) or Penalized Weighted Least Squares (PWLS) [50, 51, 63, 29, 36, 25, 26]. One simple regularization method supposes that images are global smooth, and enforces a roughness penalty on the solution by adding a quadratic function to the negative log-likelihood. But this assumption is often unsatisfactory, since many images are not globally smooth. They have region boundaries across which the image values can vary rapidly. The quadratic regularization causes edges to become blurred. In many images, small differences between neighboring pixels are often with noise, while large differences are due to the presence of edges. This assumption has formed the basis for many edge-preserving regularization. Most edge-preserving regularization methods rely on information from a local neighborhood to determine the presence of edges, i.e., the penalty assigned to each pixel or clique of pixels depends solely on pixel values within a small fixed neighborhood, such as the Huber function [35, 33] and q-generalized Gaussian Markov random field (q-GGMRF) [80] which increase less rapidly than the quadratic function for sufficiently large arguments. Recently total variation as a local regularization has received much attention because of the introduction of compressed sensing, which allows images to be reconstructed from small amounts of data [81]. Equipped with these advanced techniques, statistical IR exhibits particularly promising. Recent commercial IR technique applied in computed tomography (CT), Model based iterative reconstruction (MBIR) [80, 100], significantly improves image quality (IQ) compared with conventional analytical techniques. It offers the potential of combined noise reduction, high spatial resolution, contrast enhancement and artifact reduction for low-dose imaging or enhanced image clarity for improved diagnostic confidence, which would expand CT applications.

The main obstacle for statistical IR applied in clinical applications is the fact that to solve the objective function is computationally intensive compared to analytical reconstruction methods due to multiple iterations needed for convergence and each iteration involves forward/back-projections using a complex geometric system model. Optimization transfer (OT) [29] is a typical framework to find out the optimal of the objective function, which converts a high dimensional optimization to a parallel 1-D update by transferring the target optimization to a set of ‘bounded’ and separable surrogate functions. Compared to the iterative coordinate descent (ICD) algorithm [12], OT based methods, such as expectation maximization (EM) and separable parabolic surrogate (SPS) allow a naturally parallel computation, but suffer the low convergence rate which leads to more iterations. Literature [29] proposed non-separable parabolic surrogates with optimal curvatures, which produces a faster convergence yet requires a huge matrix operation. Literature [1, 77] reported ordered subsets SPS (OS-SPS), which gains an initial acceleration but induces a divergence in a limited circle. Even a relaxed OS can not guarantee the global optimal. A exponential power based larger step size was applied to Maximum likelihood expectation maximization (ML-EM) reconstruction in Literature [44]. However without monotonicity, this algorithm has potential problem with stability. In addition, the particular technique is not applied in MAP framework which is more general in tomographic reconstruction. The idea of over-relaxation was mentioned in literature[100] for the model based iterative reconstruction (MBIR) within ICD algorithm, where a relaxation within $[1, 2]$ was to enlarge the step size, however a larger step does not guarantee to produce a faster convergence and might take the risk of divergence. In literature [9], we proposed a successive increasing over-relaxation algorithm based on the knowledge of a convergence rate matrix. This algorithm exhibits tremendous properties of parallel computation, monotonic and global convergence with fast rate. In tomosynthesis, 3D image reconstruction is more challenged by the cone beam (CB) geometry, the highly incomplete and non-symmetric sampling and the huge reconstructed volume. Analytical tomosynthesis reconstruction for this particular geometry still needs to be fully understood. As an attempt to provide more flexibility in the reconstruction choices, ML method has been introduced and compared with conventional reconstructions [102, 85]. MAP based statistical iterative reconstruction (IR) technique was also studied with DBT system [1, 2, 3], where a modified penalty function was proposed for the data independent resolution. An edge-preserved regularizer was introduced as well as adjustable parameters for a non-linearly tunable trade-off between resolution and noise [6]. The introduction of statistical IR methods to tomosynthesis, much of the effort has been devoted to demonstrating the feasibility of the proposed techniques and illustrating some of its benefits in the general case [102, 85, 1, 2, 3, **?**].

The dissertation presents the implementation, optimization and comparison of several representative reconstruction algorithms and the proposed statistical iterative reconstruction (IR) method for DBT 3D image reconstruction. Multiple key techniques in statistical IR are proposed and further optimized for the particular application. the superior IQ provided by these promising techniques is going to be realized to benefit the diagnostic in real clinical applications.

This dissertation is organized as follows. Chapter 2 provides the theoretical reviews and implementations of several representative tomosynthesis reconstruction methods including FBP, SART and OS-MLEM. Chapter 3 addresses a general Maximum a posterior (MAP) modeling for statistical IR. The edge preserved prior is introduced with the design of the influence functions flexible enough to provide sufficient control over desired IQ. The implementation of the statistical model relies on the technique of forward and backprojection upon the imaging system. A practical implementation of it is demonstrated based on an efficient ray-driven method. ROI reconstruction with high resolution with an oversampled ray-driven technique is proposed to leverage the benefit of the proposed statistical IR. In Chapter 4, I shall introduce a modified prior model by inserting a precomputed parameter κ. Such a technique allows a predictable IQ and uniform resolution. Simulation results illustrates the effectiveness of it and provide a look-up table for further usage. Chapter 5 provides a method to optimize the flexibility of the edge preserved prior model upon IQ assessment tools. Visual comparisons are presented with different parameters choices and those representative methods. Both Chapter 6 and Chapter 7 discuss efficiently computational methods to solve the statistical IR. Chapter 6 introduces a semi-quantitative method to optimize the diminishing relaxation parameter for a convergent ordered-subsets computational framework with fast rate. But the convergent solution is not guaranteed the exact global optimal solution due to the usage of partial dataset. Thereby chapter 7 further develops the convergence theorem for optimization transfer (OT) with full dataset each iteration. Moreover, based on these theorems, the successively increasing over-relaxation OT (sir-OT) algorithm is summarized and demonstrated with a superior and monotonic convergence. Phantom study indicates that the hybrid of sir-OT and ordered-subsets present a great potential to be a parallelizable algorithm with fast and monotonic convergence rate. In Chapter 8, comprehensive evaluations are performed on reconstruction results of breast phantom, noise power spectrum phantom and simulated phantom, to assess the IQ improvement of the proposed statistical IR compared to those representative ones. Assessment tools with both spatial domain and frequency domain are involved. In the last chapter, we summarize our contributions and discuss the future work and directions.

CHAPTER 2

IMPLEMENTATION OF REPRESENTATIVE RECONSTRUCTION METHODS IN DIGITAL BREAST TOMOSYNTHESIS

The goal of transmission tomography, including tomosynthesis breast imaging, is to obtain an estimate of the 3D attenuation coefficients μ of the imaged object (patient). Given the measured noisy projection data y, a reconstruction step is needed to compute this estimate.

There are many reconstruction methods available, and they can be classified into two categories: deterministic reconstruction and statistical reconstruction. The image model includes Poisson photon noise, electronic noise (detector noise), scatter and a polyenergetic x-ray source. Different reconstruction methods handle these differently.

The deterministic reconstruction methods ignore Poisson photon noise and detector noise since they do not use a noise model. Various deterministic methods are available. They can be divided into two categories: analytical and linear algebraic. Analytical methods such as the filtered backprojection (FBP) algorithm try to invert the imaging operator in the continuous domain based on simplified imaging models. Linear algebraic methods such as the algebraic reconstruction technique (ART) and simultaneous algebraic reconstruction technique (SART) can incorporate sophisticated imaging models via the A matrix. In tomosynthetic mammography, the necessities of a short-scan and low-dose result in noisy projection data due to a low number of collected counts. Poisson noise is a concern, therefore the reconstruction problem naturally becomes a statistical problem. The statistical reconstruction methods incorporate the Poisson noise into its model and can also incorporate detector noise. Statistical methods (methods using a noise model) of image reconstruction often outperform deterministic algorithms in terms of image quality [61, 80]. The major impediment to their implementation transmission tomographic systems has been their heavy computational burden. We shall discuss the mathematical formulations for some popular image reconstruction algorithms in the two categories of deterministic and statistical algorithms and emphasize their applications and problems in breast tomosysnthesis.

2.1 DETERMINISTIC RECONSTRUCTION METHODS

Deterministic approaches to transmission tomography begins with estimating the line integrals from the ideal model Equation 4.1 and then applies algorithms to the collection of line-integral estimates:

$$p_i = \int_{L_i} \mu(r) dl, i = 1, ..., M \tag{2.1}$$

where p_i denotes the line integral of attenuation coefficients of the voxels along the i-th ray path. One obtains the estimate g_i of p_i by log-transform as follows:

$$g_i = log \frac{b_i}{y_i - r_i}, \tag{2.2}$$

where y_i are noisy measurement data. According to Bear's law, g_i are identical to p_i if there is no noise present. Since Poisson photon noise is ignored in deterministic methods, ideally we have

$$g_i = p_i. \tag{2.3}$$

One then reconstructs estimates μ from g_i using some deterministic algorithm. For the discrete case, we rewrite Eq. 2.3:

$$g_i = [A\mu]_i = \sum_{j=1}^{N} a_{ij}\mu_j, i = 1, ..., M, j = 1, ..., N, \tag{2.4}$$

which could also be represented as

$$A\mu = g, \tag{2.5}$$

where g is a line integral vector with M elements. This linear system model is the basis for deterministic methods. The reconstruction is a inverse problem and its goal is to solve this linear system, where A and g are known and is unknown. In tomosynthesis, Eq. 2.5 is $A_{tomo}\mu = g$.

2.1.1 Filtered backprojection reconstruction

In the simple Backprojection method, one takes the line integral at each pixel in the projection and smears it back along the path of the incident ray. If this process is performed for each pixel in a projection and for all projection views, one can obtain a simple backprojected estimate of the object. Consider a 2D object with parallel-beam projections. If we had a delta function object, the backprojected reconstruction appear as a spoke pattern and its Fourier transform falls off linearly as the radial spatial frequency increases. Filtering the 2D spoke pattern image by a 2D ramp filter will restore the backprojection to the true object. By the central slice theorem [7], one could equivalently do this filtering in the projection domain. Filtering the projection image by multiplying its Fourier transform by a ramp function (proportional to radial spatial frequency) and then backprojecting them, one can reconstruct the point, and by linearity, an entire object. This process is referred to as filtered backprojection (FBP). The 2D FBP algorithm for complete parallel-beam angular sampling is well known and described in many textbooks [7, 47] and we will not give the mathematical description here.

The 2D FBP methods for parallel and fan-beam projections are frequently used in transmission and emission CT [72], in which a large number of projection images acquired over 360° / 180° are used to reconstruct cross-sectional images. With a large number of projections, the information in the object is well sampled and the corresponding spatial frequency domain is well sampled, so the object can be restored by combing the information from all projections. In 2D FBP methods, the Fourier central slice theorem [7] is a fundamental key. With a parallel-beam approximation, the Fourier transform of a projection yields a plane through the 2D Fourier space of the object along the direction perpendicular to the x-ray beam [7]. As the x-ray source and the detector are rotated around the object, a set of data is swept out in 2D Fourier space. The central slice theorem holds for a projection at any angle. For limited angle acquisitions, the theorem tells us which parts of Fourier space are not being sampled.

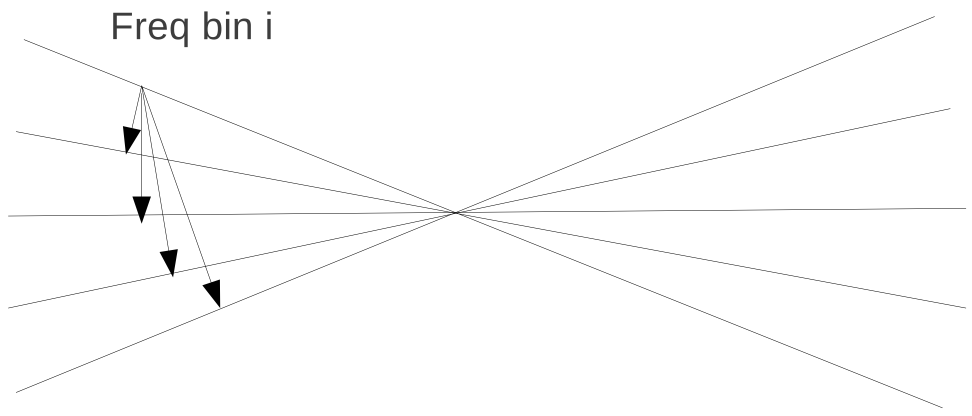

Figure 2.1. Sampling density calculation in spatial frequency domain.

FBP methods also exist for 3D data, and these can be applied to the tomosynthesis problems. As in 2D, 3D FBP reconstructions obey a form of central slice theorem. In tomosynthetic reconstruction, only a limited angular range is swept during acquisition, not all of the volume of 3D Fourier space is sampled. The main limitation for tomosynthesis is the incomplete angular sampling of the object. The cone-beam geometry is used in breast tomosynthesis. The relation between the cone-beam projections and the Radon transform was presented by Smith [74], and the solution to the general cone-beam reconstruction was also provided. For 3D cone-beam breast tomosynthesis, the Feldkamp method [32], an approximation of the cone-beam FBP algorithm, was explored by Wu et al. [86] but their reconstruction results were very noisy, along with artifacts. The result of the Feldkamp algorithm indicates that the low-frequency contrast restoration should be considered. A prototype digital tomosynthesis mammography system using a modified FBP method was reported in [68], but no details were given.

In our implementation, a specific 2D ramp filter was designed based on the sampling density, which is calculated as the inverse of the shortest distance from a sampled point in Fourier space to sampled points from another view [78, 53, 32] as shown as Fig. 2.1. Briefly speaking, the developed FBP algorithm involved the following steps: 1) Apply 1-D Fourier transformation on each column (along tube alignment direction) of the original projection images into frequency space. 2) Multiply the inverse sampling density ramp filters with the corresponding Fourier Transformed projection column by column. 3) Apply a Hanning filter to reduce high frequency noise and ring effect along each column. 4) Inverse Fourier transform the filtered projection. 5) Backproject the filtered projection in spatial space for reconstruction.

A Hanning filter was applied to reduce the amplification of high frequency noise [86, 18, 55]. The applied Hanning filter was:

$$w(i) = a + (1-a)cos(\frac{2\pi i}{N}), \tag{2.6}$$

where i is the individual frequency bin in the total points of N in frequency space. a = 0.6 was chosen as a good compromise of resolution and noise.

2.1.2 Algebraic reconstruction technique

As another example of deterministic reconstruction methods, algebraic methods with the system model Eq. 2.5 are often used. In algebraic reconstruction techniques, the tomographic inverse problem is to solve the large-scale system of linear equations of Eq. 2.5 with N variables and M equations. Under ideal conditions, such simultaneous equations could be solved exactly by matrix inversion:

$$\mu = (A^T A)^{-1} A^T g. \tag{2.7}$$

However, the inverse of $(A^T A)$ does not usually exist. $N >> M$ leads to an ill-posted problem which has no unique solution. As we discussed in section 2.1.1, FBP method solves the inverse problem of Eq. 2.1 by central slice theorem, which is mathematically accurate upon a continuous form of μ. However, the accuracy can not be held when the expression of Eq. 2.1 is discretized by Eq. 2.5. In fact, this discretization can not be avoided since the finite representative of μ. The discrete form of FBP reconstruction could be presented as

$$\mu = A^T (A A^T)^{-1} g, \tag{2.8}$$

where the linear operator $(AA^T)^{-1}$ on projection g is equivalent to a convolution between a ramp filter kernel and the projection data. This equivalence is not quite accurate since the operator is never a strictly circulant matrix. The convolved results are then projected back to the attenuation coefficient vector μ by operator A^T. To accurately solve the discrete model represented by Eq. 2.5, iterative methods are applied. To implement such a method, one can first make the initial guess at the solution represented as vector $\mu^{(0)}$ in the M -dimensional space. In most cases, one can simply set all the initial to be zero. This initial guess is projected on the hyperplane represented by the first equation in Eq. 2.5 giving $\mu^{(1)}$. Then $\mu^{(1)}$ is projected on the hyperplane represented by the second equation in Eq. 2.5 to yield $\mu^{(2)}$ and so on. When $\mu^{(n-1)}$ is projected on the hyperplane represented by the i-th equation in Eq. 2.5 to yield $\mu^{(n)}$, the process can be mathematically described by

$$\mu_j^{(n)} = \mu_j^{(n-1)} - \frac{q_i - g_i}{< a_i, a_i >} a_{ij}, \tag{2.9}$$

where

$$q_i =< \mu^{(n-1)}, a_i >, \tag{2.10}$$

and μ_j is the j-th component of μ. The new value of the j-th component is obtained by correcting its current value $\mu_j^{(n-1)}$ by $\Delta\mu_j(n)$, which is

$$\Delta\mu_j^{(n)} = \frac{< \mu^{(n-1)}, a_i > - g_i}{< a_i, a_i >} a_{ij}, \tag{2.11}$$

While g_i is the measured line-integral along the ith ray, $< \mu^{(n-1)}, a_i >$ can be understood to be the computed line-integral for the same ray based on the $(n-1)$-th solution. The correction $\Delta\mu_j^{(n)}$ to the j-th voxel is obtained by first calculating the difference between the measured line-integral and the computed line-integral, normalizing this difference by $< a_i, a_i >$ and then assigning this value to all voxels in the ith ray, each assignment being weighted by the corresponding a_{ij} [19].

The linear attenuation coefficients are updated at each ray, therefore ART converges fast to a least squares solution which can be very noisy for severely ill-posed inverse problem such as limited-angle tomosynthetic reconstruction [102]. There are some variations on its computer implementation. ART has been modified to other methods such as simultaneous algebraic reconstruction technique (SART) [47] and simultaneous iterative reconstruction technique (SIRT) [47]. In SART, the correction terms are simultaneously applied for all the rays in one projection, and the linear attenuation coefficient of each voxel is updated after all rays passing through this voxel at one projection view are processed; while in SIRT, all projection rays are calculated and applied to a correction factor, and the update is performed after all rays in all projection views are processed. SIRT converges slowly because its update is averaged over all projection rays and the reconstruction could be overly smoothed. We shall describe the SART method in detail. As mentioned above, for SART, the value update of each voxel is performed after all rays at one projection view are processed. The number of updates in one full iteration is equal to the number of projection views K, and also is called as the number of sub-iterations. Let $\mu_j^{n,k}$ denote the estimated linear attenuation coefficient of the jth voxel at the end of the k sub-iteration of the nth iteration. The initial and final update values at one iteration are assigned as follows:

$$\mu_j^{n,1} = \mu_j^{n-1}, \mu_j^{n} = \mu_j^{n,K}, \tag{2.12}$$

where μ_j^{n} is the estimate at the end of the n-th iteration, which is equal to the estimate after all K projection views are processed. Let G_j denote the index set of the measured line integrals passing through the j-th voxel at the k-th projection angle. The update of the linear attenuation coefficient at the j-th voxel is defined as follows:

$$\mu_j^{n,k+1} = \mu_j^{n,k} - \lambda \frac{\sum_{i \in G_j} a_{ij} \frac{<\mu^{n,k}> - g_i}{L_i}}{\sum_{i \in G_j} a_{ij}}, \tag{2.13}$$

where λ is a relaxation factor ranged over (0, 1]. The relaxation factor is used to reduce the noise during reconstruction. In some cases, this parameter is chosen as a function of the iteration number. That is, λ decreases as the number of iterations increases. L_i could be represented as

$$L_i = \sum_{j=1}^{N} a_{ij}. \tag{2.14}$$

The choice of the initial guess is very important. This is a general problem for iterative reconstruction methods. A good choice of initial condition can speed up the convergence. An initial condition chosen to the final solution will speed up convergence. In some cases, a simple BP reconstruction serves as a good initial condition. Another problem associated with iterative reconstruction approaches is the choice of a stopping point. An appropriate stopping point determines the image quality of reconstruction. Earlier termination results in a low-contrast reconstruction, while more iterations yields more noisy estimates. Given this compromise, the optimal number of iterations is often predetermined based on visual comparison and image quality analysis. Because iterations are terminated before convergence, the iterative methods do not exactly invert Eq. 2.5.

2.2 STATISTICAL ITERATIVE RECONSTRUCTION

2.2.1 Maximum likelihood reconstruction

For a photon counting detector or a mono-energetic X-ray device, the Poisson distribution of incident photon number dominates the physical process. That is the photons flux along a projection follows Poisson distribution which can be described mathematically as

$$P_{likelihood}(Y_i = y_i|\mu) = \frac{\theta_i^{y_i} e^{-\theta_i}}{y_i!}, \tag{2.15}$$

where Y_i is a random variable counting the observed photons on the detector along i-th X-ray; y_i is one observation of Y_i; θ_i is the expectation value of the random variable Y_i, that is related to the line integral projection by Beer's law of attenuation [43]. In the classical physical model, it can be expressed as

$$\theta_i = d_i e^{-<\mu, l_i>} + r_i, \tag{2.16}$$

where d_i is the intensity of the incident X-ray; μ is a linear attenuation coefficient vector to be estimated. Each voxel is assigned an attenuation coefficient and the l_i denotes the vector of the system coefficient generated by the i-th X-ray and each voxel. The term r_i accounts for the mean number of background events and read-out noise variance [75]. The negative log-likelihood function of all observed photons on the detector can be written as [51]

$$L(\mu) = \sum_{i}^{M} \{d_i e^{-<\mu, l_i>} - y_i \log(d_i e^{-<\mu, l_i>} + r_i)\} + c, \tag{2.17}$$

under the assumption that $\{Y_i\}_{i\in[1,M]}$ are *i.i.d*, where c is a constant and M is the number of X-ray beams. Through minimizing Eq. 2.17, the optimal μ can be estimated.

To solve the problem directly is intractable. Literature [29] proposed the concept of optimization transfer, where a series of surrogate functions bounded by the objective one are conceived and in turn minimizing Eq. 2.17 has been transferred to the minimization of the surrogate ones.

We demonstrate how to motivate a surrogate for ML case, one can rewrite Eq. 2.17 as

$$L(\mu) = \sum_{i=1}^{M} \ell_i(t_i), \tag{2.18}$$

where

$$\ell_i(t_i) = d_i e^{-t_i} - y_i \log(d_i e^{-t_i} + r_i), \tag{2.19}$$

when $r_i = 0$, $\ell_i(t_i) = d_i e^{-t_i} + y_i t_i$, where $t_i =< \mu, l_i >$. It's trivial to check the convexity of $\ell_i(t_i)$ with $d_i, y_i \geq 0$. By using the equivalent transformation

$$< \mu, l_i >= \sum_{j=1}^{N} a_{ij}(\frac{l_{ij}}{a_{ij}}(\mu_j - \mu_j^n) + < \mu^n, l_i >), \tag{2.20}$$

where

$$a_{ij} = \frac{l_{ij}}{\sum_{j=1}^{N} l_{ij}}, \tag{2.21}$$

$$\sum_{j=1}^{N} a_{ij} = 1, \tag{2.22}$$

and the convex property, one can write

$$\begin{aligned} L(\mu) &\leq \sum_{i=1}^{M}(\sum_{j=1}^{N} a_{ij}\ell(\frac{l_{ij}}{a_{ij}}(\mu_j - \mu_j^n) + <\mu^n, l_i>)) \\ &= G(\mu, \mu^n), \end{aligned} \tag{2.23}$$

the induced $\mu^{(n)}$ denotes the attenuation coefficients at the n-th iteration. $G(\mu, \mu^n)$ is a surrogate function of the $L(\mu)$. Minimizing the $L(\mu)$ has been shifted to minimize the surrogate one and the solution sequence from each surrogate function will be guaranteed to approach the optimal solution of Eq. 2.17 monotonically. By applying Newton's iteration on $G(\mu, \mu^n)$

$$\mu_j^{(n+1)} = \mu_j^n - \frac{\sum_{i=1}^{M} l_{ij}(-d_i e^{-<\mu^n, l_i>} + y_i)}{\sum_{i=1}^{M}(l_{ij} \sum_{j=1}^{N} l_{ij} d_i e^{-<\mu^n, l_i>})}. \tag{2.24}$$

One can notice that both Eq. 2.13 and Eq. 2.24 are suitable for parallel computations. All voxels can be updated simultaneously in each iteration. But the “bounded” condition of the surrogate function of ML method could produce a conservative step size for each iteration, especially when the solution approaches to the global optimal. This conservation leads to a slow convergence [9].

Literature [27] proposed an algorithm formulated using a quadratic approximation to the Poisson likelihood Eq. 2.17, which leads to a weighted least square algorithm. The simple form encouraged a faster convergent algorithm which is iterative coordinate descent (ICD) [70, 100]. Applying a second-order Taylor's expansion to $\ell_i(t_i)$ in Eq. 2.19 around the estimation $\hat{t_i}$, it yields

$$\ell_i(t_i) \approx \ell_i(\hat{t_i}) + \ell_i'(\hat{t_i})(t_i - \hat{t_i}) + \frac{1}{2}\ell_i''(\hat{t_i})(t_i - \hat{t_i}). \tag{2.25}$$

We can estimate $\hat{t_i}$ with

$$\hat{t_i} = \log(\frac{d_i}{y_i - r_i}). \tag{2.26}$$

Knowing

$$\ell_i'(t_i) = -d_i e^{-t_i} + y_i \frac{d_i e^{-t_i}}{d_i e^{-t_i} + r_i}, \tag{2.27}$$

and

$$\ell_i''(t_i) = d_i e^{-t_i} - y_i \frac{d_i e^{-t_i}(d_i e^{-t_i} + r_i) - (d_i e^{t_i})^2}{(d_i e^{-t_i} + r_i)^2}. \tag{2.28}$$

Substituting Eq. 2.19, Eq. 2.26, Eq. 2.27 and Eq. 2.28 into Eq. 2.25, we arrive at

$$\ell_i(t_i) \propto \frac{(y_i - r_i)^2}{2y_i}(t_i - \hat{t}_i)^2. \tag{2.29}$$

This resulting in the weighted least square function

$$Q(\mu) = \sum_{i=1}^{M} \frac{w_i}{2}(< \mu, l_i > - \log \frac{d_i}{y_i - r_i})^2, \tag{2.30}$$

where

$$w_i = \frac{(y_i - r_i)^2}{y_i}. \tag{2.31}$$

This quadratic form encourages a greedy search optimization method ICD [70, 100]. ICD method transfers the high dimension optimization into a sequential of one dimension problems. For example, to seek for an optimal μ_k, a partial derivative on μ_k is needed, which is

$$\frac{\partial Q(\mu)}{\partial \mu_k} = \sum_{i=1}^{M} w_i l_{ik}(\sum_{j=1}^{N} \mu_j l_{ij} - \log \frac{d_i}{y_i - r_i}) = 0. \tag{2.32}$$

Given $\mu = \mu^n$, to produce μ_k^{n+1}, an equivalent transformation is applied:

$$\sum_{i=1}^{M} w_i l_{ik}(\sum_{j=1}^{N} \mu_j^n l_{ij} - \log \frac{d_i}{y_i - r_i} + (\mu_k^{n+1} - \mu_k^n) l_{ik}) = 0. \tag{2.33}$$

Based on it, we derive μ_k^{n+1} as

$$\mu_k^{n+1} = \mu_k^n - \frac{\sum_{i=1}^{M} y_i l_{ij} e_i}{\sum_{i=1}^{M} w_i l_{ik}^2}, \tag{2.34}$$

where e_i denotes the error sinogram after each updating with the form of

$$e_i =< \mu^n, l_i > - \log \frac{d_i}{y_i - r_i}. \tag{2.35}$$

The algorithm can be described as that in every iteration n we sequentially address every voxel j in a certain order [100] and compute its attenuation by Eq. 2.35. Each voxel is calculated upon the error sinogram e_i calculated by the relevant voxels with the latest updated value. Therefore voxels updating within this algorithm is hard to be parallel. But it yields the best convergence demonstrated in literature [21], which provided practical comparisons among different algorithms. In our study, to retain the benefits from the parallel computing, instead of ICD algorithm, an OT based algorithm [9] with faster convergence rate and flexibility of updating maps will be introduced in the later chapter.

CHAPTER 3

MODELING OF STATISTICAL ITERATIVE RECONSTRUCTION

3.1 STATISTICAL MODEL FOR IMAGE RECONSTRUCTION

In transmission tomography, Compton scattering, which deflects X-ray photon from its original path, forms a randomly additional noise on detectors. This noise is more severe in tomosynthesis because of the usage of CB and flat-panel detector. Electronic noise from devices forms another source of corruption on the data. High variation is induced in the reconstructed volume by the over-fitting of the noisy data. Literature [87] developed a Bayesian inference method with the prior encouraging the data consistency of each projection. The posterior distribution of μ is written as

$$P_{post}(\mu|Y) \propto P_{likelihood}(Y|\mu)\pi(\mu). \tag{3.1}$$

Most of these priors define a probability density function for voxels to deviate from their neighbors. The constraint is imposed into the solution by adding the negative log-transformed prior to the negative log-likelihood. Such PL subjective function has the following form:

$$\Psi(\mu) = L(\mu) + \lambda R(\mu), \tag{3.2}$$

where the parameter λ controls the strength of the penalty function $R(\mu)$, which is the negative log-transformed of the prior $\pi(\mu)$. One of the most popular is Gaussian Markov random field (GMRF) prior, which is generally defined by the following function:

$$\pi(\mu) \propto \prod_{j}^{N} \prod_{k}^{N_j} \exp(\rho(\Delta_{jk})), \tag{3.3}$$

where

$$\rho(\Delta_{jk}) = -\omega_{jk} \frac{\Delta_{jk}^2}{2\sigma_\mu^2}, \tag{3.4}$$

$j \in N$ is the index of voxel; $k \in N_j$ denotes neighborhood index; σ is the standard deviation of intensity of voxels; $\Delta_{jk} = \mu_j - \mu_k$. The neighborhood mask ω_{jk} is typically defined by:

$$\omega_{jk} = \frac{1}{((x_j - x_k)^2 + (y_j - y_k)^2)^{1/2}}, \tag{3.5}$$

The quadratic penalty applies a globally smooth effect on voxels, which usually causes edges to be blurred. To improve the edge preservation, generalized Gaussian Markov Random Field (gGMRF) [11] was introduced into Digital tomosynthesis [6], which defines Eq. 3.4 as follows:

$$\rho(\Delta_{jk}) = (\frac{\Delta_{jk}}{c})^p. \tag{3.6}$$

A 3×3 neighborhood clique in the transverse reconstructed plane is applied, therefore ω_{jk} can be simplified as 1. The exponent parameter p of the gGMRF allows one to control the degree of edge preservation in the reconstruction. As long as $p > 1$, the resulting regularizer term is strictly convex. The constant c determines the approximate threshold of transition between low and high contrast regions. When $p = 2$, the regularizer term is quadratic and the reconstructed images tend to be softer. As p is reduced, the regularizer becomes non-quadratic and edge sharpness tends to be preserved. The corresponding derivative of it is known as the influence function:

$$\rho'(\Delta_{jk}) = \frac{p|\Delta_{jk}|^{p-1}}{c^p} sign(\Delta_{jk}). \tag{3.7}$$

In Fig. 3.1, we compares the influence function of the quadratic regularizers with several edge-preserving gGMRF priors. In the quadratic cases ($p = 2$), the influence functions are linear around the origin, which controls textures in a uniform manner. Reduced p retains better edge-preserving characteristics, as influence function tends to be constant for larger argument. The value c controls the inflexion point. Higher c pushes the edge preserving behavior towards the origin. For example, to maintain the similar influence to the quadratic with $c^p = 1$ under the difference of 0.01, which is considered as the upper boundary of noise variation, the c^p values for the $p = 1.8, p = 1.7, p = 1.61$ are set as $2.5, 3.5, 5.3$.

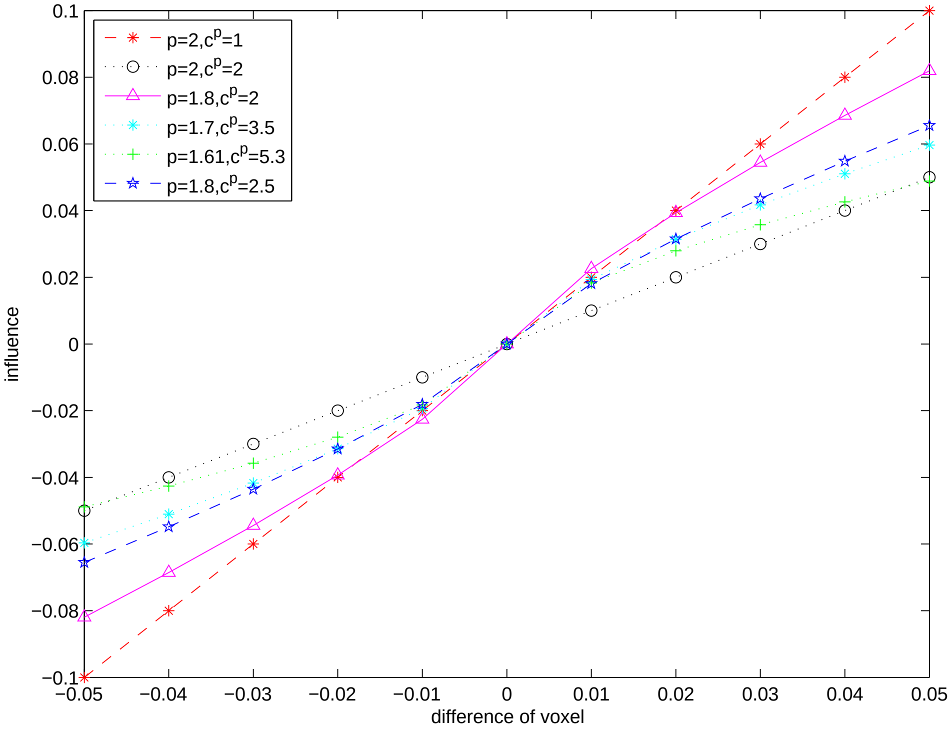

Figure 3.1. Influence function of the gGMRF regularizer with different parameters.

3.2 GEOMETRIC CONFIGURATION AND FORWARD AND BACK-PROJECTION MODEL

As shown in Fig. 3.2, a typical DBT system acquires $11 \sim 25$ projections by rotating the X-ray tube around the center of rotation over $< 50^o$ angular. The breast and the detector are stationary during the acquisition. The tube usually operated at $20 \sim 40$ kVp generates cone beam X-ray to cover the whole object. The collimator is shifted during the acquisition to confine the x-ray illumination area to the detector. The motion of the collimator is synchronized with the motion of the tube. The x-ray dose for a tomosynthesis exam is comparable to a single mammogram. The flat panel detector with a large pixel array and small pixel size is used to record the images. The anti-scatter grid is usually not used. In clinical tomosynthesis imaging, the breast of the patient is compressed in the same way as in mammography. The total image acquisition time is usually about

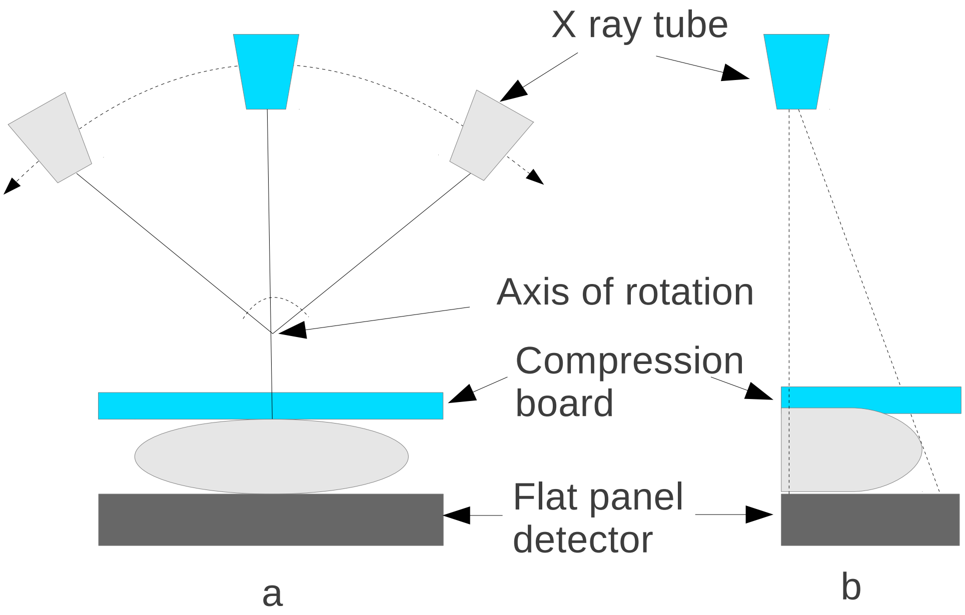

Figure 3.2. DBT imaging system: (a) front view; (b) side view.

$5 \sim 8$ s.

The crucial advantage of statistical IRs is that they allow any choice of system coefficient which is needed in statistical model described as Eq. 2.17. Any scanning geometry such as the cone beam and plat panel detector can be accurately modeled by proper computation of the vector of system coefficient. The model can be designed to realistically represent the scanner, although this may come at the cost of great computational expense. The calculation of system coefficients essentially in the forward and backward model lies at the core of any efficient implementation of IR and often drive computation time and reconstruction accuracy. One of the models to calculate the system coefficient is distance driven (DD) [54] which accurately takes account into the detector response and the voxel response. This method leads to a fast implementation without degrading the frequency response and is considered to be the state of art approach. On the other hand, DD technique is developed along with voxel-based iterative algorithm [100] such as ICD where voxel calculation in one iteration needs the related error sinograms to be updated by other voxels. The inherent relevance makes voxel-based algorithm hard to be paral-

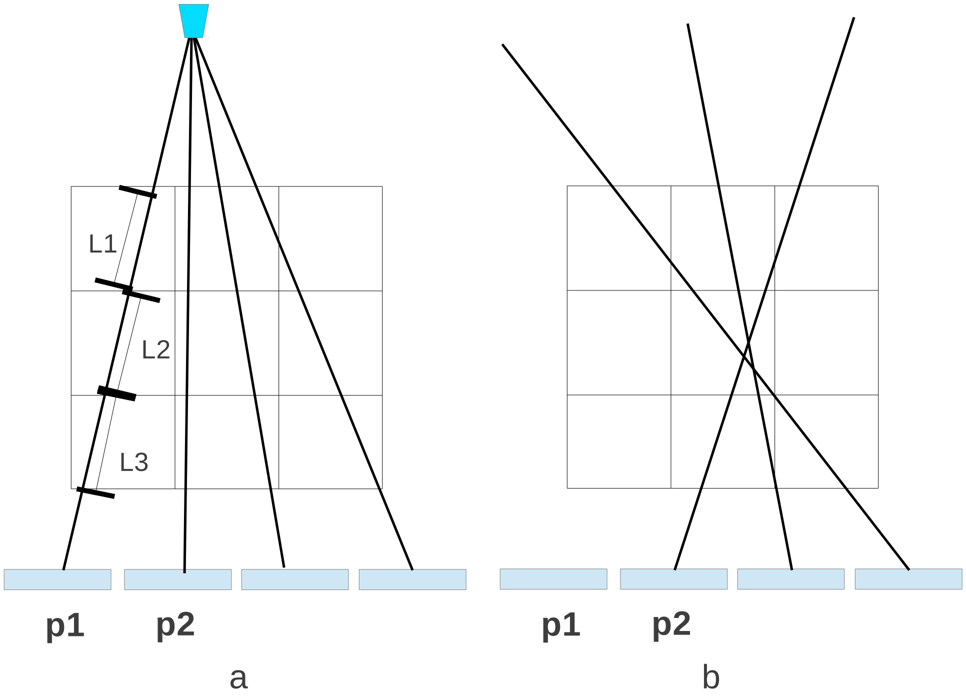

Figure 3.3. Ray-driven model: (a) ray-driven forward model; (b) ray-driven backprojection model.

lel. Another type of algorithm such as conjugate gradient (CG) [58] or ordered subsets (OS) [28] requires a full independent forward and backprojection for each iteration. This kind of method is convergent slower than ICD but easy to be implemented in parallel. For this particular situation, we applied and optimized ray-driven method to implement the forward and backprojection. A typical 2-D ray-driven forward model is demonstrated in Fig. 3.3 (a) where the image space is meshed up into voxel and the ray is modeled by a line connecting the source and the center of each pixel on detector. The expected projection data p_1 is formulated as

$$p_1 = L_1\mu_1 + L_2\mu_2 + L_3\mu_3, \tag{3.8}$$

where μ_j is linear attenuation coefficient of the j-th voxel along the ray path. An efficient ray-driven method is proposed based on the idea of literature [2]. A traversal algorithm to locate the voxels passed by a ray is set upon the ray equation: $\hat{u} + t\hat{v}$, where $\hat{u}$ is the start point of the ray and $\hat{v}$ denotes the ray direction. The ray is broken into intervals of t, each of which spans the whole voxel. To determine the t, the ray length crossing the first vertical voxel boundary and the ray length intersecting the first horizontal voxel boundary are compared. The minimum of these two will indicate how much the ray travels and still remain in the current voxel. The intersected length between the ray and the current voxel is calculated by subtracting last t from the current t. The boundary through which the ray reaches out the current voxel is recognized to indicate the next traversal voxel whose index is retrieved by +1 or -1 along with the current voxel index. A forward projection along a ray is performed by the inner product of intersection length vector and the corresponding linear attenuation coefficient. The backprojection of a voxel is typically calculated by averaging the projection values indexed by all the rays passing through this voxel as shown in 3.3 (b). Specifically, assuming that there are a total of M rays going through the j-th voxel over all projection views, the backprojection of j-th voxel b_j is formulated as

$$b_j = \frac{\sum_{i=1}^{M} l_{ij} p_i / L_i}{\sum_{i=1}^{M} l_{ij}}, \tag{3.9}$$

where p_i denotes the projection data on the i-th detector element; l_{ij} denotes the length of intersection of the i-th ray model and j-th voxel; L_i is the total length of the ray model intersecting within the whole volume.

3.3 ROI RECONSTRUCTION WITH SUPER RESOLUTION

Statistical IR can recover fine details and small features in the reconstruction more accurately than conventional algorithms. In order to fully benefit from this higher spatial resolution, IR reconstruction requires a higher spatial sampling rate, or equivalently smaller voxels, to represent fine details such as micro-calcification and fibrils. In this section, we apply ray-driven method on an oversampled detector elements with a higher resolution. Intersected ray number and voxel number are significantly increased, such that extra computational time is required. Region-of-interest (ROI) reconstruction is applied to reduce the computing time by concentrating the computation only on the small regions of the image that contain fine details.

In DBT system, the voxel size to be reconstructed within image plane is usually the same as the size of detector element. To increase the spatial resolution, voxels are needed to be divided into sub-voxels. The size of sub-voxel becomes smaller than the detector element size. In this case, original ray-driven model, which represents a ray by a line connecting the source and the center of corresponding detector element, is not accurate enough. It causes the resolution loss and known chess grid effect [56]. Fig. 3.4 demonstrates the reason of the problem and shows a potential solution as well. Fig. 3.4 (a) presents the forward model of a single voxel whose size is equal to the size of detector element. The dotted lines along the two boundary of the detector element represents the actual ray coverage along its path per detector element. In this case, the intersection between the voxel and the line which connecting the source and the center of the detector is accurate enough to be applied to forward and backprojection. In Fig. 3.4 (b), one voxel is divided into four sub-voxels in order to quadruple the resolution. According to the ray-driven model, the forward projection p is written as:

$$p = l_1^s \mu_1^s + l_2^s \mu_2^s + l_4^s \mu_4^s, \tag{3.10}$$

where l_j^s denotes the ray intersection with the corresponding sub-voxel j whose attenuation coefficient is μ_j^s. According to Eq. 3.10, only sub-voxels 1, 2, 4 are taken into account along the ray path. However the dotted line indicates all of these sub-voxels should contribute to the intensity reduction of the present ray. In this case, the ray model fails to present the actual effect of the ray. An over-sampled ray-driven method [103] may solve the problem. Instead of modeling the ray as one line, double lines, each of which connects the source and quarters of a detector element shown in Fig. 3.4 (c) , are applied, where the intensity reduction for the detector element d3 is modeled by the forward projection with the double lines, which is

$$p = \frac{1}{2}(l_{11}^s \mu_1^s + l_{13}^s \mu_3^s + l_{14}^s \mu_4^s) + \frac{1}{2}(l_{22}^s \mu_2^s + l_{24}^s \mu_4^s). \tag{3.11}$$

As to l_{ij}^{s}, $i \in 1, 2$, denotes each of the double lines for the current specific detector element. Compared with Eq. 3.10, Eq. 3.11 presents more accuracy in terms of forward model.

The disadvantage of this over-sampled ray-driven method is that it can significantly increase the computational cost of IR, since more rays are required to be considered and many more voxels are needed to be reconstructed. A full reconstruction with over-sampled ray-driven method is not very practical in real. Fortunately, the exhausted computation to reconstruct the whole volume is not necessary, since details which are interesting only locates in small region or ROI. Lots of efforts has been done for ROI reconstruction in CT [42, 99] to gain more details in the target field of view (TFOV) and to reduce the exhausted computational cost. A typical method needs two-path reconstructions. The first path is applying a pilot reconstruction of full field of view (FFOV) with a lower resolution and in the second path, smaller voxels in the TFOV are updated based on the error sinograms yielded by the pilot reconstruction. The mis-match of voxel size leads to certain reconstruction error. The amount of it usually depends on the implementation. Compared with CT, the image slice, which is parallel to the detector plane, is reconstructed transversely in DBT system. The number of slices is relatively few which ranges from 30 to 60. The angular range is typically less than 30°. These specific features allow a direct ROI reconstruction without any reconstruction mis-match. The key of this technique is to generate a mask on each projection data set in order to reduce the number of effective rays and the number of related voxels. As demonstrated in Fig. 3.5, ROI in the plane p is marked by a circle which centers at e (x_e, y_e, z_e) with the radius of r_e. The region within the circle is meshed up into the voxels with required size. The circle is projected on the projection data set according to the tube position s (x_s, y_s, z_s) to form a circular mask, which locates at the center of c (x_c, y_c, z_c). z_c is 0 in the current coordina-

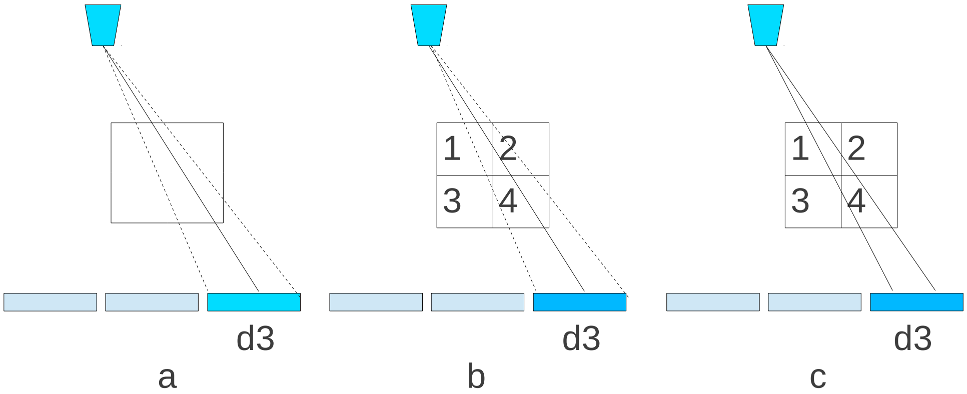

Figure 3.4. Ray-driven forward model for voxel and sub-voxel: (a) ray-driven model for voxel; (b) ray-driven model for sub-voxel; (c) over-sampled ray-driven model for sub-voxel.

tion system. (x_c, y_c) could be represented mathematically as:

$$x_c = x_e - \frac{(x_s - x_e)z_e}{z_s - z_e},$$
$$y_c = y_e - \frac{(y_s - y_e)z_e}{z_s - z_e}, \tag{3.12}$$

with the radius of

$$r_c = r_e \frac{z_s}{z_s - z_e}. \tag{3.13}$$

The circular mask on the projection indicates the minimum data set required to reconstruct the voxels in ROI. The mask is slightly changed for each projection data set as the view angle varies. Because only a small region in a projection is activated, the number of rays to be taken into the forward projection and the number of voxels to be updated in the backprojection are significantly reduced. More importantly, since we apply a uniform voxel size along each ray path, there is no mis-match of voxel size and no reconstruction error consequently. The ROI reconstruction is introduced together with the super resolution technique to attack the computational complexity and to obtain high spatial details.

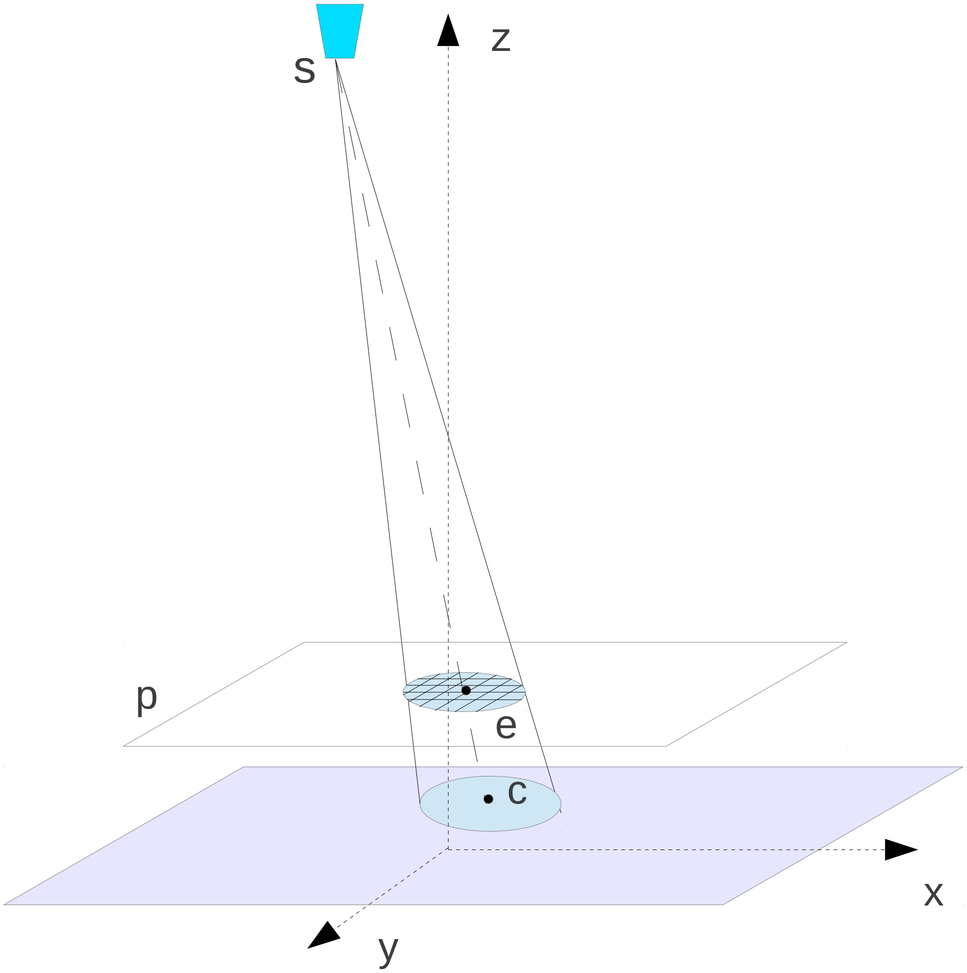

Figure 3.5. A circular mask, which is formed by projecting the ROI boundary along the ray beam, indicates the minimum data set required to reconstruct the voxels in ROI.

CHAPTER 4

A PRE-COMPUTED BACKPROJECTION BASED MODIFIED REGULARIZATION

4.1 METHOD FOR CHARACTERIZING THE SMOOTHING PARAMETER λ

In Eq. 3.2, the penalty $R(\mu)$ takes a form of

$$R(\mu) = \sum_{j=1}^{N} \sum_{k \in N_j} \rho(\mu_j - \mu_k), \tag{4.1}$$

Where N_j is the neighbors of the j-th voxel. The function $\rho(t)$ is defined as Eq. 3.6. For a quadratic case, ρ can be formulated as follows

$$\rho(\mu_j - \mu_k) = \frac{1}{2}(\mu_j - \mu_k)^2, \tag{4.2}$$

which results in a consistent smoothing on adjacent voxels. Through minimizing Eq. 3.2, the optimal estimation of μ can be shown in the following form

$$u^* = \arg\min_{\mu \geq 0} \Phi(\mu). \tag{4.3}$$

It's intractable to solve it directly. However, separated parabolic surrogate (SPS) introduced in [29, 28] which leads to an iterative solution, with parallel computation and monotonic convergence. The basic idea of SPS is by constructing a series of separable parabolic functions lower bounded by the objective function, the optimal value can be approached by the solution of the surrogate one at each iteration. By applying SPS on Eq. 3.2 and the quadratic penalty Eq. 4.1, the approximation of the solution at the $(n+1)$-th iteration can be written as

$$\mu_j^{(n+1)} = \mu_j^{(n)} - \frac{\sum_{i=1}^{M} l_{ij}(-d_i e^{-<\mu^{(n)}, l_i>} + y_i) + \lambda \sum_{k \in N_j}(\mu_j^{(n)} - \mu_k^{(n)})}{\sum_{i=1}^{M}(l_{ij} \sum_{j=1}^{N} l_{ij} d_i e^{-<\mu^{(n)}, l_i>}) + 2\lambda |N_j|}, \tag{4.4}$$

where $|N_j|$ is the cardinality of the subset N_j. The solution sequence of the surrogates converges to the optimal value of the objective function monotonically. A small curvature of the surrogate function, but still satisfying bounding condition, can yield a faster convergence. by replacing $d_i e^{-<\mu^{(n)},li>}$ in the denominator of Eq. 8.1 as y_i. a precomputed curvature in [29] is conceived, which may lead to a faster convergence, yet "almost always" monotonic decreasing.

In practical application, to finding a proper smoothing parameter λ in (8.1) is not trivial. The main reason is that the impulse response and the noise of the reconstructed results are data-dependent, such that λ yields unpredictable effects on resolution properties. To reduce the data dependence, the authors of the paper [37] proposed a modified penalty function and demonstrated that the impulse response of the reconstructed results is only dominated by λ, which is written as

$$R_m(\mu) = \sum_{j=1}^{N} \kappa_j \sum_{k \in N_j} \omega_{jk} \kappa_k \rho(\mu_j - \mu_k), \tag{4.5}$$

where ω is a weighted coefficient assigned to ψ. κ_j is formulated for emission tomography as follows:

$$\kappa_j = s_j \sqrt{\frac{\sum_{i=1} g_{ij}^2 q_i}{\sum_{i=1} g_{ij}^2}}, \tag{4.6}$$

In X-ray transmission tomography, s_i, g_{ij}, q_i are translated to $s_i = 1$, $i \in [1, M]$, $g_{ij} = l_{ij}$ and $q_i = y_i$. To reduce the computational complexity, we propose a simplified version as follows:

$$R_m(\mu) = \sum_{j=1}^{N} \kappa_j^2 \sum_{k \in N_j} \frac{(\mu_j - \mu_k)^2}{2}, \tag{4.7}$$

where

$$\kappa_j^2 = \frac{\sum_{i=1}^{M} l_{ij}^2 y_i}{\sum_{i=1}^{M} l_{ij}^2}, \tag{4.8}$$

since the condition of $\kappa_k \approx \kappa_j$ is obviously held in the neighbors. κ^2 is roughly equivalent to BackProjection (BP) reconstruction on the data y_i. In this chapter, we refer to the Pre-computed BP based Penalized Likelihood method as PPL applying κ^2 to absorb the data-related terms in resolution properties, such that the smoothing effect of λ can be evaluated in advance by studying simulated data. With a selective λ, PPL can produce image reconstructions with desired image qualities. By applying SPS on PPL method, the iterative solution of it is formulated by revising (8.1) as follows

$$\mu_j^{(n+1)} = \mu_j^{(n)} - \frac{\sum_{i=1}^{M} l_{ij}(-d_i e^{-<\mu^{(n)},l_i>} + y_i) + \lambda\kappa_j^2 \sum_{k\in N_j}(\mu_j^{(n)} - \mu_k^{(n)})}{\sum_{i=1}^{M}(l_{ij}\sum_{j=1}^{N} l_{ij} d_i e^{-<\mu^{(n)},l_i>}) + 2\lambda\kappa_j^2|N_j|}, \tag{4.9}$$

where κ^2 can be calculated before the iteration.

4.1.1 Pixel property

Furthermore, to demonstrate the data independence of the impulse response of PPL, we study the analytical relationship between the impulse response and the smoothing parameter λ for PL method, which is derived in the literature [37]

$$L^j(\mu) \approx [A^T D(y_i) A + \lambda R]^{-1} A^T D(y_i) A e^j, \tag{4.10}$$

where $L^j(\mu)$ denotes an impulse response yielded from an impulse signal at the j-th voxel, which has the form of

$$L^j(\mu) \approx \frac{\partial \mu(y_i)}{\partial \mu_j},$$

$\mu(y_i)$ is an estimator of μ on a noiseless measurement y_i. A is a coefficient matrix according to the system geometry. If a ray-tracing method is used, A is composed of l_{ij} denoting the length of the intersection between the i-th X-ray and the j-th voxel. $D(y_i)$ is a diagonal matrix with the entry y_i. R is the Hessian matrix of $R(\mu)$. e^j is the j-th unit vector.

From (4.10), one can see that the impulse response $L^j(\mu)$ depends not only on the system geometry and the smoothing parameter λ but also on the datasets associated with the object and incident X-ray. We substitute R_m in (4.7) to (4.10). By applying an analogous deduction in the literature [37], $L^j(\mu)$ has a data independent approximation as follows:

$$L^j(\mu) \approx [A^T I A + \lambda R]^{-1} A^T I A e^j, \tag{4.11}$$

where I is identical matrix. One can see that the data $D(y_i)$ is degraded to I as R_m, the Hessian matrix of $R_m(\mu)$, is transformed to R, the Hessian matrix of $R(\mu)$ with a basic quadratic penalty. That means the effect of λ in PPL on the impulse response reconstructed from arbitrary measurements y_i is equivalent to the one reconstructed by a penalized-likelihood method with a basic penalty from a uniform background with $y_i = 1$. In other words, the data dependence of pixel property has been eliminated by applying the modified penalty (4.7).

4.1.2 Noise property

Thanks to the studies in literature [37, 34], the noise property is represented as the covariance on reconstructed voxels

$$\begin{aligned} Cov(\mu) \;&\approx\; [A^T D(\theta_i) A + \lambda R]^{-1} A^T Cov(y_i) A \\ &\quad\; [A^T D(\theta_i) A + \lambda R]^{-1}, \end{aligned} \tag{4.12}$$

where θ_i is expressed as (2.16). From the equation, one can see that the covariance depends on the geometric configuration, smoothing parameter λ and the data. In our model, the Poisson distribution dominates the physical process, hence $Cov(y_i) = D(\theta_i)$, since $y_i, i \in [1, M]$ is *i.i.d.* The variance can be expressed by

$$Var(\mu_j) = (e^j)^T Cov(\mu) e^j. \tag{4.13}$$

By inducing the modified penalty and applying the similar deduction in the literature [37], we can obtain the formula as follows:

$$\begin{aligned} Var(\mu_j) \;&\approx\; (e^j)^T [A^T D(\theta_i) A + \lambda R_m]^{-1} A^T D(y_i) A \\ &\quad\; [A^T D(\theta_i) A + \lambda R_m]^{-1} (e^j) \\ &\approx\; \frac{V^j_{unit}}{\kappa_j^2}, \end{aligned} \tag{4.14}$$

where

$$V_{unit}^{j} = (e^{j})^{T}[A^{T}IA + \lambda R]^{-1}A^{T}IA[A^{T}IA + \lambda R]^{-1}(e^{j}). \tag{4.15}$$

From (4.14), one can conclude that the variance of the j-th voxel reconstructed by PPL method on a measurement with a unknown mean and unknown standard deviation can be quantified as V_{unit}^{j} divided by κ^2. V_{unit}^{j} denotes the variance of the j-th voxel reconstructed by a penalized-likelihood method with a basic penalty from the measurement y_i with a unit mean and unit standard deviation.

According to the discussions above, by applying PPL method, resolution properties are only dependent on λ in a fixed geometric configuration, such that desired resolution can be obtained by applying a proper λ evaluated in advance by studying simulated data. In deed, we establish a simulation based two-step procedure for λ selection and image reconstructions. In STEP 1, projections are simulated to generate mappings from λ to resolution properties. This procedure is executed just at the stage of system design when the system geometry is fixed.

STEP 1:

1: Set a range of λ.

2: Start from $k = 1$

3: Tiny balls respectively distributed in nine square regions are used as the reference phantom. These balls are assembled with the attenuation coefficients of $0.05mm^{-1}$. Projections are simulated with the phantom and a uniform incident value of $y_i = 1$ in the same system configuration with the real one.

4: Run (8.1) with the simulated projections with each λ and record average Modulation Transfer Function (MTF) on the k-th plane in a corresponding table.

5: If k does not go through all planes, then set $k = k + 1$ and go to 3.

6: Simulate projections from Poisson distribution with $\theta_i = 1, i \in [1, M]$.

7: Run (8.1) with the simulating data with each λ and record standard deviation on each plane into a corresponding table.

In STEP 2, before image reconstruction, one can choose a desired λ referred to the tables generated from item 4 and item 7 to meet the resolution requirement. Then, the reconstruction is preformed along with the determined λ. This step can be summarized as follows

STEP 2:

1: Find a λ satisfying the pixel precision and noise reduction in the real application.

2: Run (4.9) with the imaging projections with chosen λ.

4.2 SIMULATION EXPERIMENTS

To get a practical illustration of the two-step procedure, we set up a virtual system with the same geometric configuration as a real limited angle X-ray tomography system.

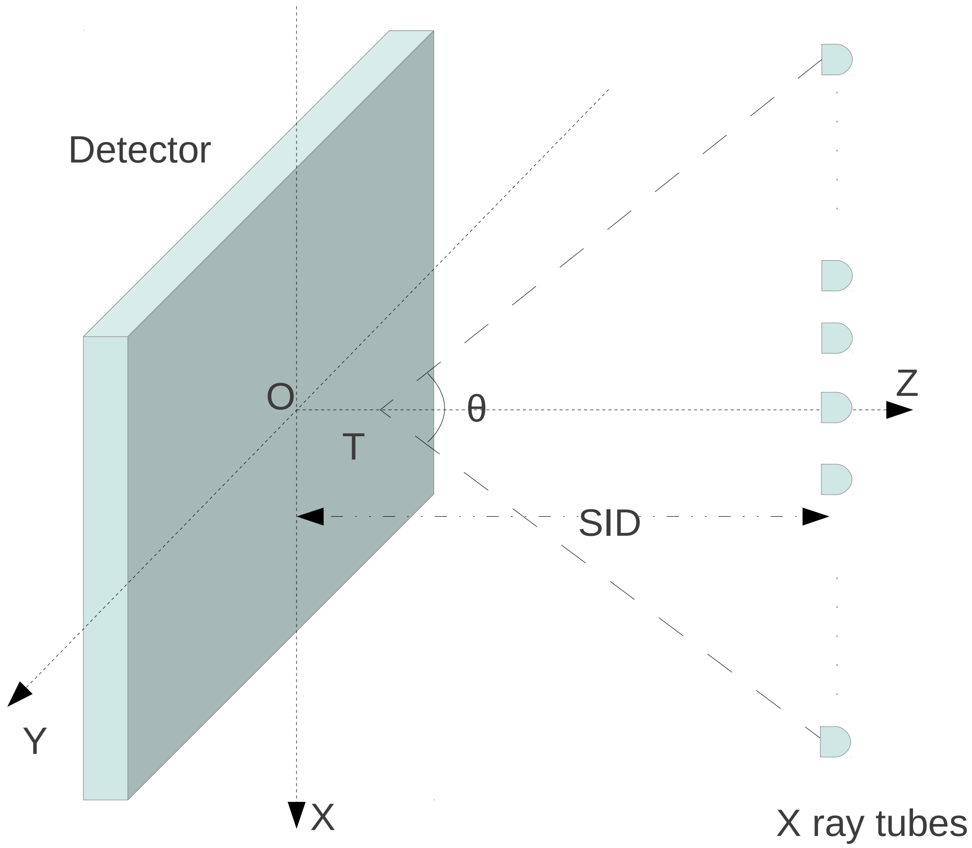

Figure 4.1. Geometric configuration of Digital Breast Tomosynthesis with multiple parallel X-ray beams.

Fig. 4.1 demonstrates the geometric configuration of a Digital Breast Tomosynthesis referred to the literature [65]. The detector size is $286.72mm$ by $286.72mm$ with the pixel size of $0.56mm$ by $0.56mm$. O is the origin of the three dimensional coordinate system which is located at the center of the detector. The source to image distance (SID) along Z direction is set as $692.8mm$ and 25 x-ray beams are positioned in a straight line parallel to the detector plane along the X axis. The middle one of the 25 beams is located on Z axis and the linear spacing between these beams varies to provide a 2° angular spacing around the rotation center T. The system provides $\theta = 48^\circ$ coverage around T. The testing phantom has the same structure, but different attenuation coefficient with the reference one in STEP 1. The focus plane is placed at the plane with $40mm$ away from the detector. The testing dataset is generated by using ray-tracing method with non-uniform

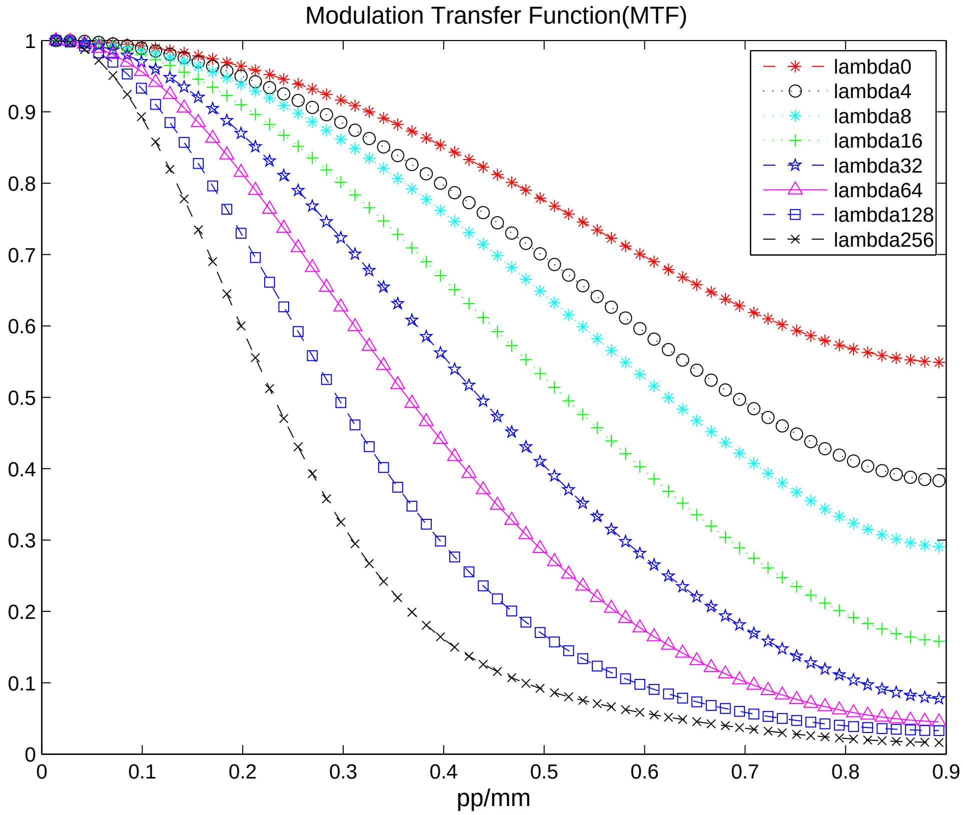

Figure 4.2. Average MTF of the focus plane reconstructed by the PL method with a basic quadratic penalty from the projections with a uniform incident value of $y_i = 1$

incident value of $y_i \gg 1, i \in [1, M]$.

After STEP 1, average Modulation Transfer function (MTF) of impulse response reconstructed with $\lambda \in \{0, 4, 8, 16, 32, 64, 128, 256\}$ over the reference phantom are drawn in Fig. 4.2. Fig. 4.4 presents the noise estimation of the system, which is represented as the standard deviation of voxel reconstructed with the range of λ. According to Fig. 4.2, table 4.1 is generated by mapping λ to Half Width of two third Magnitude of MTF. Fig. 4.4 is also represented as table 4.2. By applying STEP 2. MTF of the focus plane reconstructed by PPL with the same range of λ from the testing phantom is presented in Fig. 4.3. The testing phantom for noise property is generated from the Poisson distribution with $\theta_i \gg 1$. Fig. 4.5 shows the noise measurement on the focus plane reconstructed by PPL.

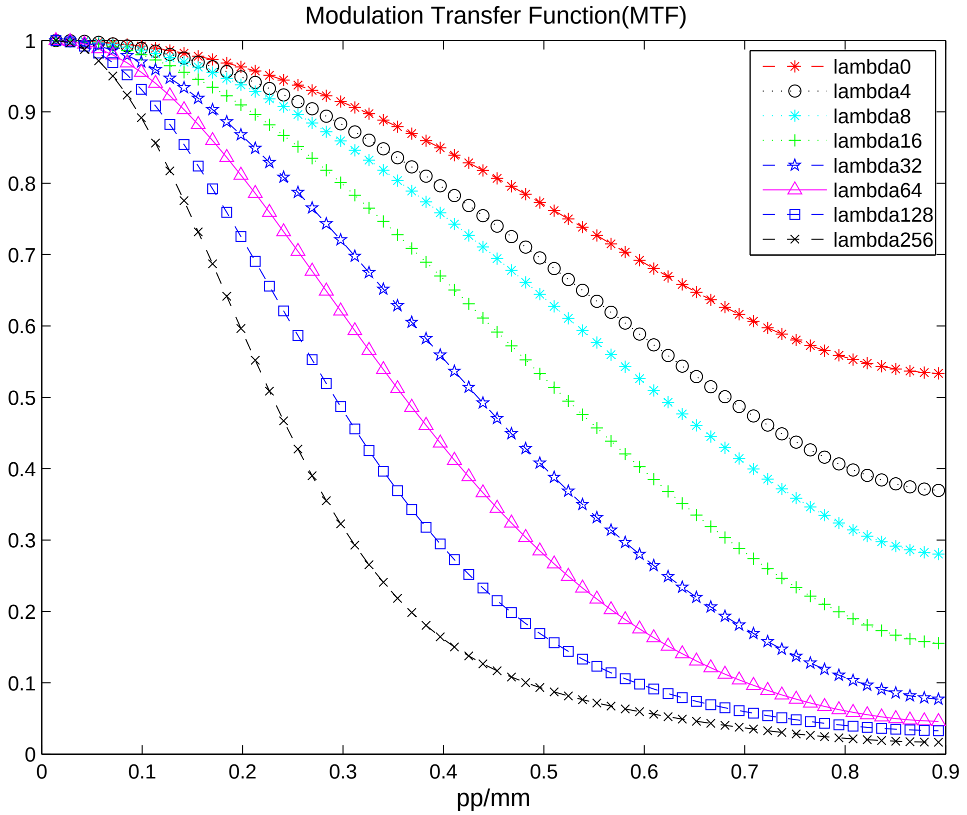

Figure 4.3. Average MTF of the focus plane reconstructed by PPL method from the projections with a non-uniform incident value with $y_i \gg 1$

From Fig. 4.3, one can see that the MTFs are almost the same as those in Fig. 4.2, which means the pixel property reconstructed by PPL method is data independent and exactly identical with the one got from PL method with a basic quadratic penalty on the uniform measurement. Fig. 4.5 shows that the declining trend of the standard deviation of noise is consistent with the one shown in Fig. 4.4. The ratio between them is nearly 1.5×10^2 which is equal to the mean value of κ_j^2 on the focus plane.

4.3 PHANTOM EXPERIENCE

To perform PPL reconstruction with the breast phantom, we collected the data with the s-DBT prototype system. The geometric configuration is shown in Fig. 4.1. The origin O of the 3-D coordinate system is located at the center of the detector. A flat panel

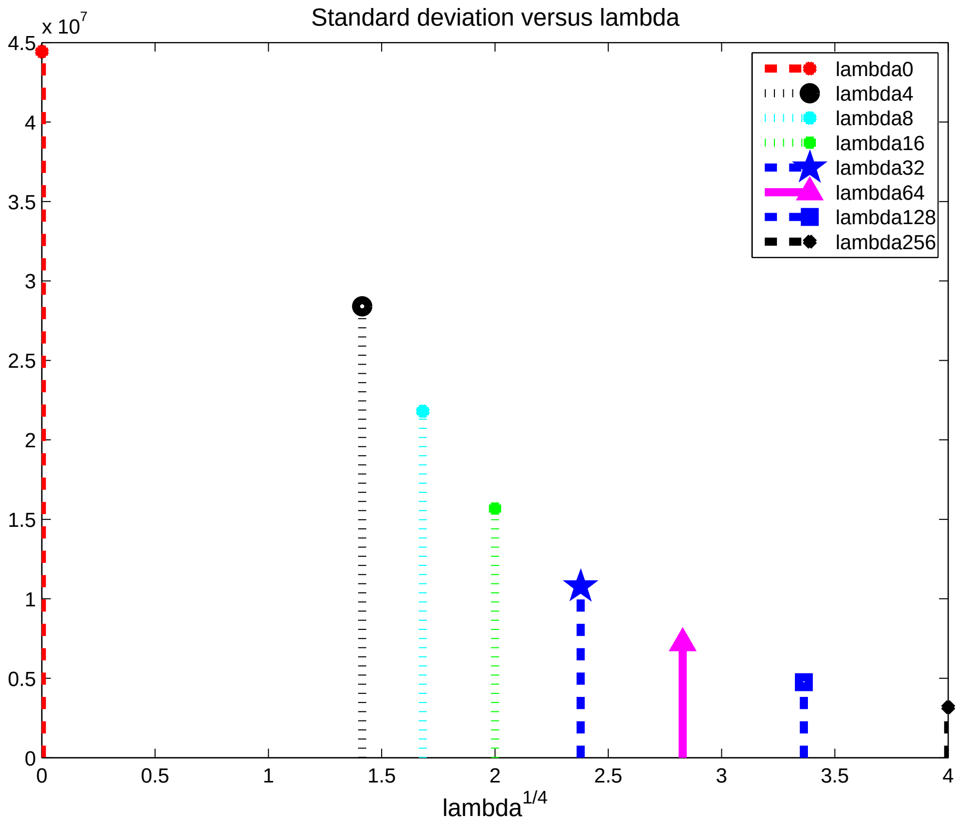

Figure 4.4. Standard deviation of the focus plane reconstructed by the PL method with a basic quadratic penalty from the projections with a expected incident value of $\theta_i = 1$

detector is used for imaging acquisition. With a 140μm pixel pitch, the total image size is 2048x1664. In the current study, the multiple X-ray beams are positioned along a straight line parallel to the detector plane and the middle beam is projected to C on the detector surface. The source is designed to have 15 X-ray beams spanning a angular coverage of 14.00^o. The linear spacing between the X-ray beams varies to provide an even angular spacing at a source-object distance (SOD) of 64.99cm. A 3-D tissue equivalent breast phantom was employed. The phantom was placed 2.5cm away from detector surface plane. The images were acquired using: 28KVp, molybdenum filter, molybdenum target and total dose of 100mAs (6.67mAs per view).

Along with STEP 2, $\lambda = 8$ is chosen, which implies that the pixel precision drops

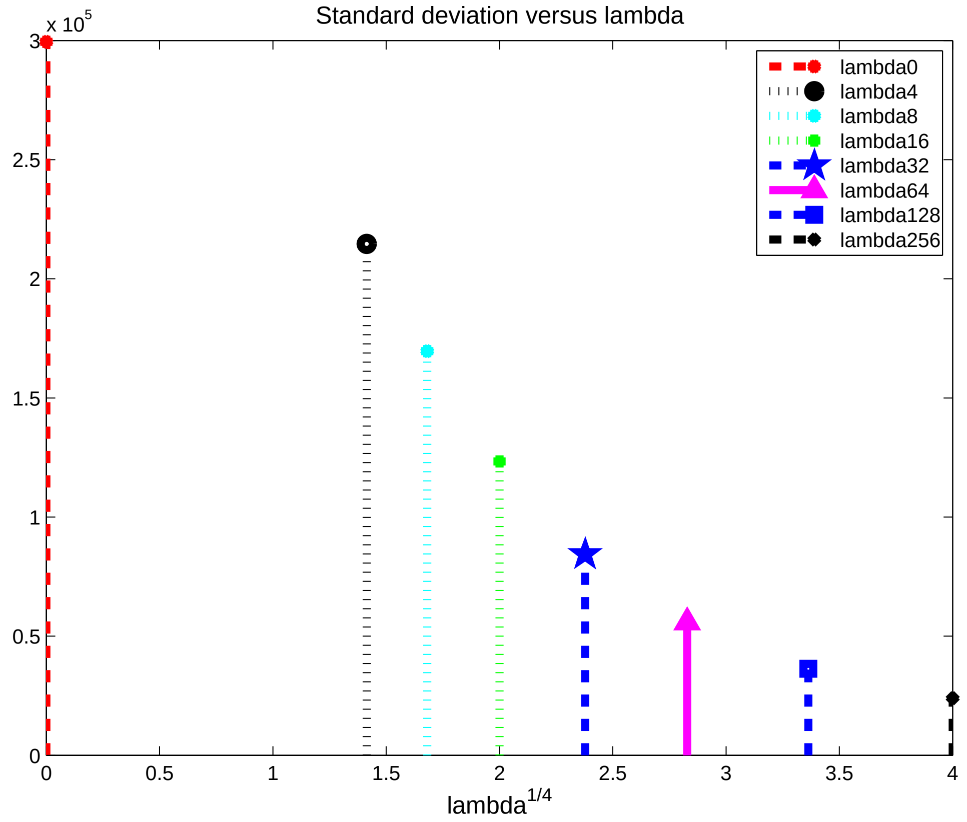

Figure 4.5. Standard deviation of the focus plane reconstructed by PPL method from the projections with a expected incident value of $\theta_i \gg 1$

25.53% and the noise is reduced by 50.29% compared to the choice of $\lambda = 0$, which makes PPL degrading to ML-EM method. 40 slices through the phantom are produced from 2.5cm to 6.5cm with 1mm resolution in the coordinate system. The iterative solution of PPL (4.9) with 20 times iterations is applied to approach the optimal. FBP with Gaussian post-filter, MLEM with 20 iterations and SART methods with 10 iterations are also employed for the comparisons. All iterative methods are initiated by FBP.

Figs. 4.6-4.9 show 4 groups of Field of View (FOV) on the reconstructed plane at 2cm away from the bottom of the phantom, which are (1) circular mass in a flat background (CMF), (2) micro-calcifications in a flat background (MCF), (3) multiple micro-calcifications within a circle (MCC) and (4) circular mass in a complex background

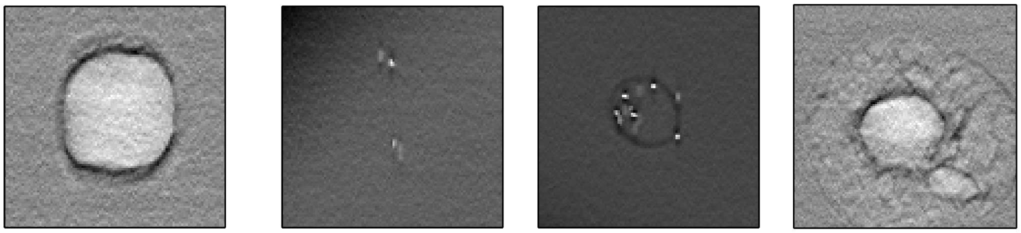

Figure 4.6. FOVs of PPL

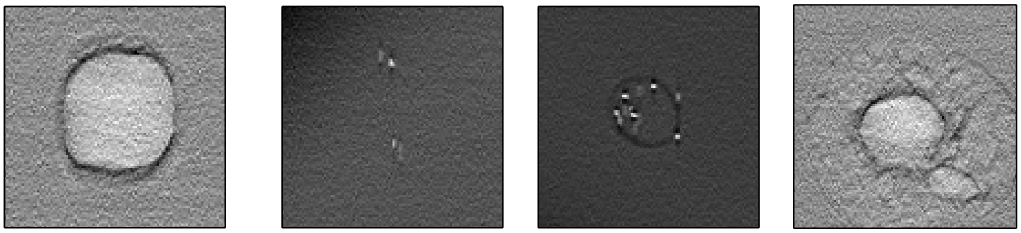

Figure 4.7. FOVs of MLEM

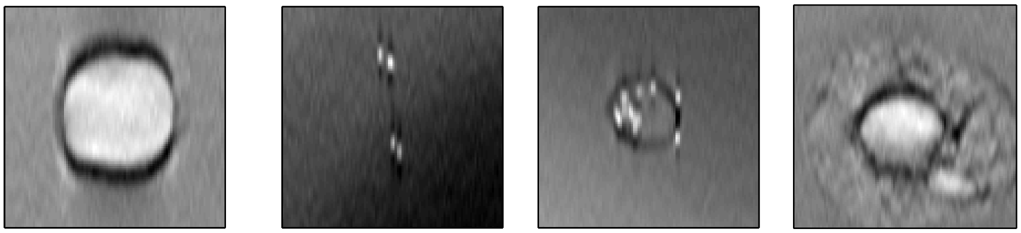

Figure 4.8. FOVs of FBP

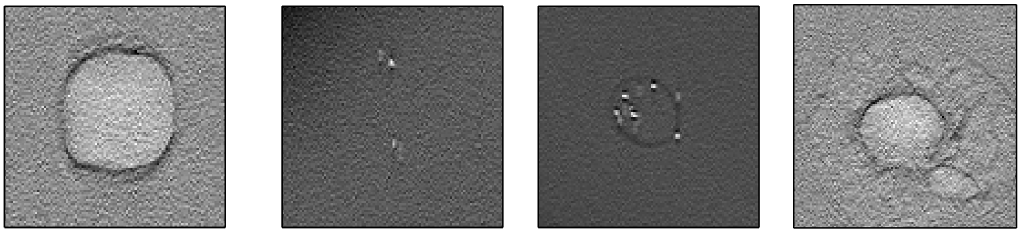

Figure 4.9. FOVs of SART

Table 4.1. Half Width of $\frac{2}{3}$ Magnitude of MTF versus λ

λ	Half Width	Pixel Precision Drop (%)
0	0.635472	0.000000
4	0.525515	17.303263
8	0.478106	26.763620
16	0.397181	37.498289
32	0.330624	47.971842
64	0.275509	56.645008
128	0.223154	64.883809
256	0.176390	72.242692

(CMC). Fig. 4.6 shows the results reconstructed by PPL method. Fig. **??** shows the results reconstructed by ML-EM method. Fig. 4.8 shows the results reconstructed by FBP with Gaussian post-filter. Fig. 4.9 shows the results reconstructed by SART method.

From the CMF group, one can see that FBP with Gaussian post-filter leads to the worst sharpness of edges and the most artificial effects. ML-EM and SART provide slightly sharper edge than PPL. However, the noise of PPL is much more suppressed than ML-EM and SART. The higher image contrast and lower noise result in a prominent Contrast Noise Ratio (CNR) for the results from PPL. In the CMC group, detail in the background is glossed by the high noise in SART and ML-EM, while PPL presents more detail in the complex background due to the high CNR. In the MCF and MCC groups, PPL shows a comparable sharpness of micro-calcifications with SART and ML-EM, which also confirms the normalized PSFs shown in Fig. 4.11 measured across one of the micro-calcifications. We also compare the Artifacts Spread Functions (ASFs) shown

Table 4.2. Standard deviation versus λ

λ	Std.	Std. Drop (%)
0	44431105.332625	0.000000
4	28404617.148036	36.070424
8	21797860.046811	50.940091
16	15677423.612897	64.715207
32	10786101.586691	75.723985
64	7217356.036651	83.756074
128	4757971.747843	89.291350
256	3176508.576684	92.850710

in Fig. 4.10 to measure the structure removal from the out-of-planes, where the ASF of PPL outperform the one from SART.

4.4 DISCUSSION

In this study, we proposed PPL method, which is a PL with a simplified version of the modified penalty [37]. PPL can lead to a data-independent reconstruction in terms of resolution properties. By an analogous derivation, the data-related terms are eliminated in both impulse response and standard deviation. Therefore, the effects of λ on resolution properties can be predicted. A simulation based two-step procedure was proposed to perform image reconstructions with predictable image quality. The effectiveness and robustness of the reconstruction strategy are validated by the simulation experiments. we also compared PPL reconstruction with several representative methods with the current s-DBT. In the comparison, PPL with a selective parameter provides prominent image qualities with controllable resolution, high contrast and low noise compared to the others.

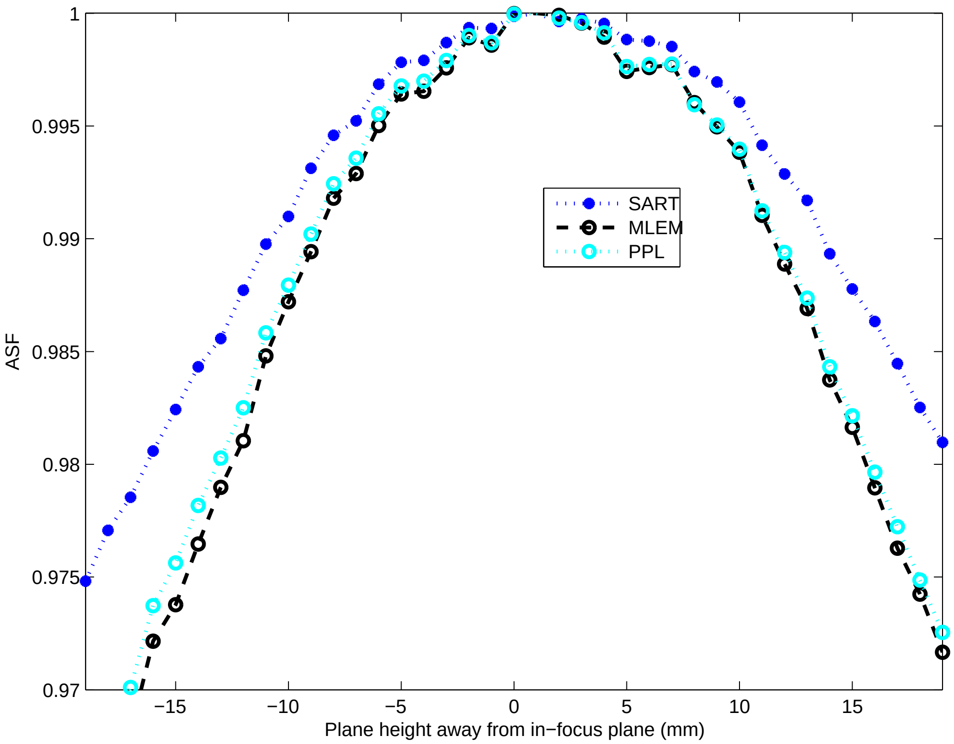

Figure 4.10. Comparison of ASFs reconstructed by SART, MLEM and PPL

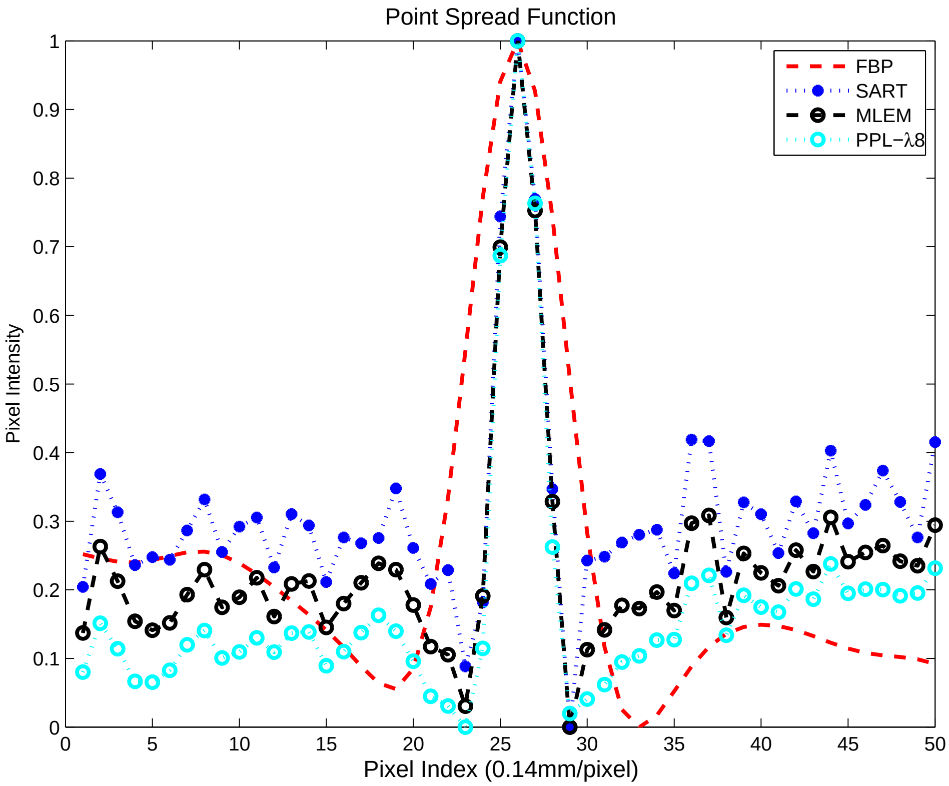

Figure 4.11. Comparison of normalized PSFs reconstructed by SART, MLEM and PPL

Therefore, the enhanced CNR from PPL method benefits both micro-calcifications and mass on the breast-equivalent phantom. A thorough IQ evaluation of PPL method will be given in the later chapter.

CHAPTER 5

PARAMETER OPTIMIZATION OF GENERALIZED GAUSSIAN MARKOV RANDOM FIELD REGULARIZATION

5.1 COMPARISON STUDY OF SELECTED PARAMETERS

The form of the gGMRF prior depends on two parameters: p controls the degree of curvature in the influence function in low and high contrast regions and c determines the threshold between the two. In order to seek for an optimal parameter combination, the reconstructed results of a breast phantom with a homogeneous tissue background are investigated with different parameter combinations, which are $p = 2, c^p = 1$; $p = 1.8, c^p = 2$; $p = 1.8, c^p = 2.5$; $p = 1.7, c^p = 3.5$ and $p = 1.61, c^p = 5.3$. Point spread function (PSF) and Contrast to noise ratio (CNR) as estimation tools are measured in these results.

The PSF curves presented in Fig. 5.1 (a) are measured by crossing the isolated micro-calcification demonstrated in Fig. 5.2 (a). These curves are then fitted into the Gaussian functions to remove the noise. The Fourier transform of the fitted function is modulation transfer function (MTF) as shown in Fig. 5.1. The resolution frequency at 50% MTF peak is used to describe the in-plane pixel precision. As discussed in section II, the smaller p tends to introduce more edge-preserving behavior towards high contrast region and automatically the inflexion point is pushed towards high contrast which leads to more smoothing in low contrast region. By increasing c, the inflexion is pulled to a smaller value in order to improve the low contrast detectability. Among all parameter combinations for SIR-ρ-OT, parameter $p = 1.61, c = 5.3$ presents the best frequency response.

CNR is calculated to investigate the contrast sensitivity by subtracting the mean value in the background marked as region 1 from the mean value of the mass region marked as 2 and dividing the standard deviation of region 1 as shown in Fig. 5.2 (b).

The half width of 50% MTF and CNR above are summarized in Tab. 5.1 where the

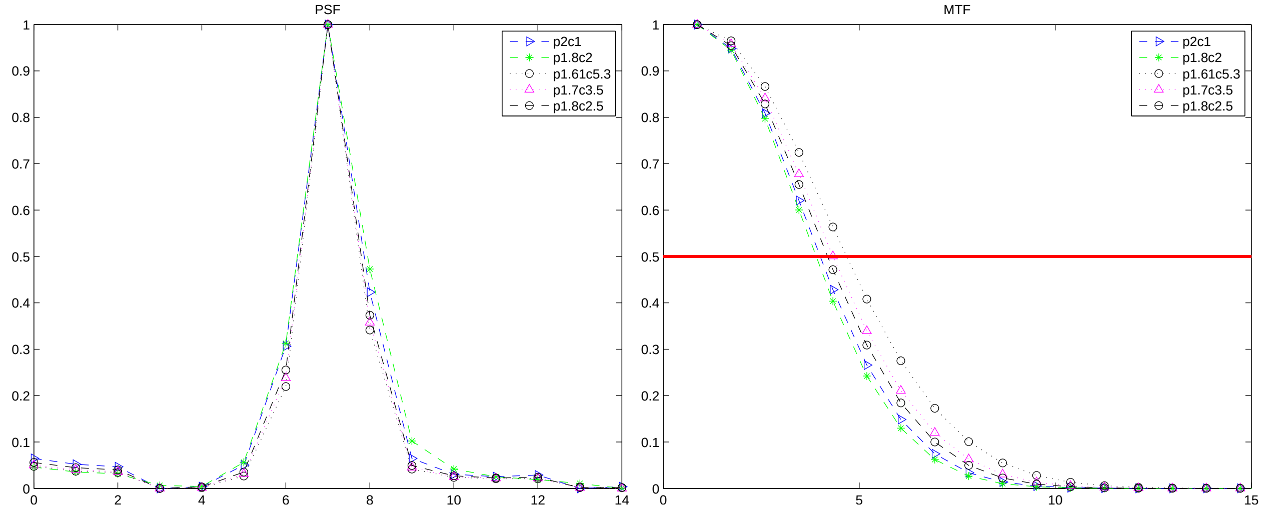

(a) (b)

Figure 5.1. Pixel precision measured along micro-calcification on a focus plane reconstructed by SIR-ρ-OT with selected parameter combinations. (a) shows PSF curves; (c) shows MTF curves

Table 5.1. CNR and in-plane MTF for SIR-ρ-OT with selected parameter combinations

parameters	CNR	HWHM of MTF
$p = 2$, $c = 1$	6.1601	4.0063
$p = 1.8$, $c^p = 2$	12.4267	3.9041
$p = 1.8$, $c^p = 2.5$	6.5769	4.1951
$p = 1.7$, $c^p = 3.5$	7.3294	4.3324
$p = 1.61$, $c^p = 5.3$	7.5906	4.6825

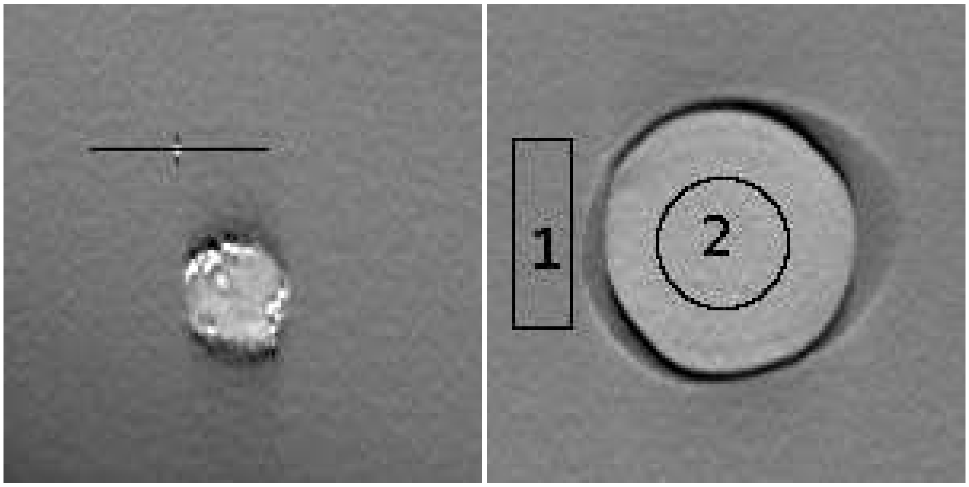

(a) (b)

Figure 5.2. Measurement of PSF and CNR. (a) demonstrates the micro-calcification which is used to measure PSF; (b) shows a mass object and its background to calculate CNR

parameter combination of $p = 1.61, c^p = 5.3$ leads to the highest resolution and also produces the second highest CNR. The parameter combination $p = 1.8, c^p = 2$ produces the highest CNR but give the worst pixel precision. Upon these observations, it appears that $p = 1.61, c^p = 5.3$ gives a good compromise between resolution and contrast sensitivity. These parameter combination potentially providing the optimal IQ will be employed in the rest experiments.

5.2 IMAGE RECONSTRUCTION WITH BREAST PHANTOM

With the choice of the strictly convex regularizer, the objective function defined in Eq. 3.2 has a unique global minimum. To estimate voxels at the unique global optimal, both ICD [100] and relaxed OS-SPS [1] can provide fast algorithms. The former produces a faster convergence on high frequency voxel with a sequential voxel update and the latter provides a parallel computation with a decent convergence rate. We choose relax OS-SPS in our application for a more flexible parallel computing framework. By applying the idea of optimization transfer [29] on GGMRF regularizer, The iterative solution is derived as follows.

$$\mu_j^{(n+1)} = \mu_j^{(n)} - \frac{\sum_{i=1}^{M} l_{ij}(-d_i e^{-<\mu^{(n)},l_i>} + y_i) + \lambda\kappa_j^2 \sum_{k\in N_j} \frac{p|\mu_j^{(n)}-\mu_k^{(n)}|^{p-1}}{c^p} sign(\Delta)}{\sum_{i=1}^{M}(l_{ij}\sum_{j=1}^{N} l_{ij} d_i e^{-<\mu^{(n)},l_i>}) + 2p(p-1)\lambda\kappa_j^2 \sum_{k\in N_j} \frac{|\mu_j^{(n)}-\mu_k^{(n)}|^{p-2}}{c^p}}. \quad (5.1)$$

In the implementation, voxels are able to be processed simultaneously due to the mutual independence update. One forward projection and one backward projection are required in one iteration. Ray-driven method is employed in forward model. In addition, κ is pre-calculated with a backprojection-equivalent computation prior to all iterations.

To study the effects of our proposed regularizer on image quality, we apply statistical IR with the regularizer with $p = 1.8, c^p = 2$, $p = 1.61, c^p = 3.5$ and $p = 2, c = 1$ on tomosynthesis phantom data, and then compare them other representative methods such as filtered backprojection (FBP) and ordered subsets maximum likelihood expectation minimization (OSEM). λ in OS-PPL is set as 8 according to our previous study [3]. To guarantee global convergence, all iterative methods are initialized by three-time iterations of OS method and followed by a non-OS method for ten-time iterations.

The data was collected with the sDBT prototype system [65, 82]. Scatter correction technique [45] is applied with the data to improve the high and low contrast. The origin of the 3-D coordinate system is located at the center of the detector. A flat panel detector is used for image acquisition. With a 140μm pixel pitch, the total image size is 2048x1661. The multiple X-ray beams are positioned along a straight line parallel to the detector plane. The source is designed to have 15 X-ray beams spanning a distance of 32.38cm from end to end. The linear spacing between the X-ray beams varies to provide an even 2° angular spacing. A 3-D breast phantom is placed on a stage with a 2.54 cm air gap. The images were acquired using: 28KVp, molybdenum filter, molybdenum target and 20mAs per projections.

Fig. 5.3 and Fig. 5.4 present mass and micro-calcifications equivalent objects in respective focus plane reconstructed by OS-PPL with our proposed regularizer and other representative algorithms. In Fig. 5.3, one can see that statistical iterative methods pro-

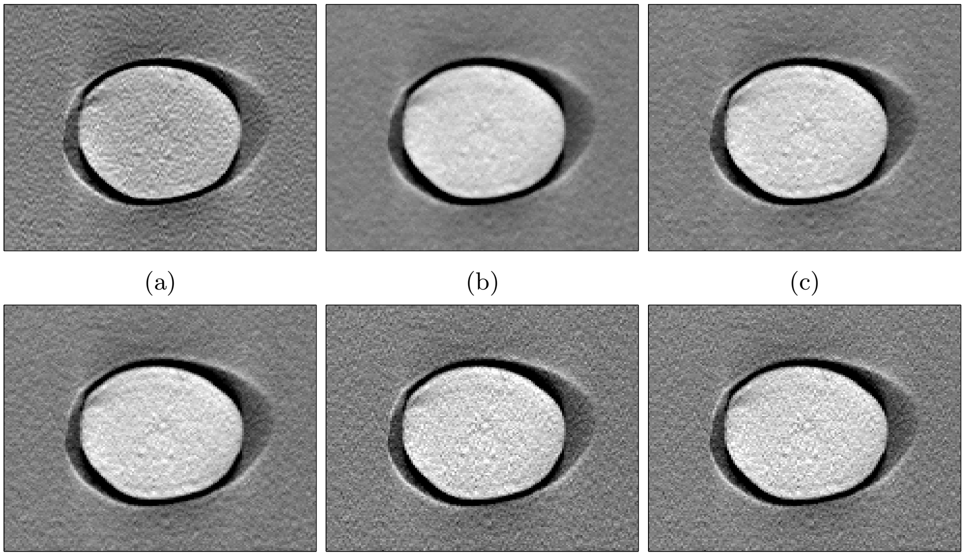
(a) (b) (c)

(d) (e) (f)

Figure 5.3. Reconstructed mass between our proposed methods with various parameter choices and some representative methods. (a) FBP (b) statistical IR with $p = 1.8, c^p = 2$ (c) statistical IR with $p = 1.61, c^p = 3.5$ (d) statistical IR with quadratic regularization (e) OS-EM (f) SART

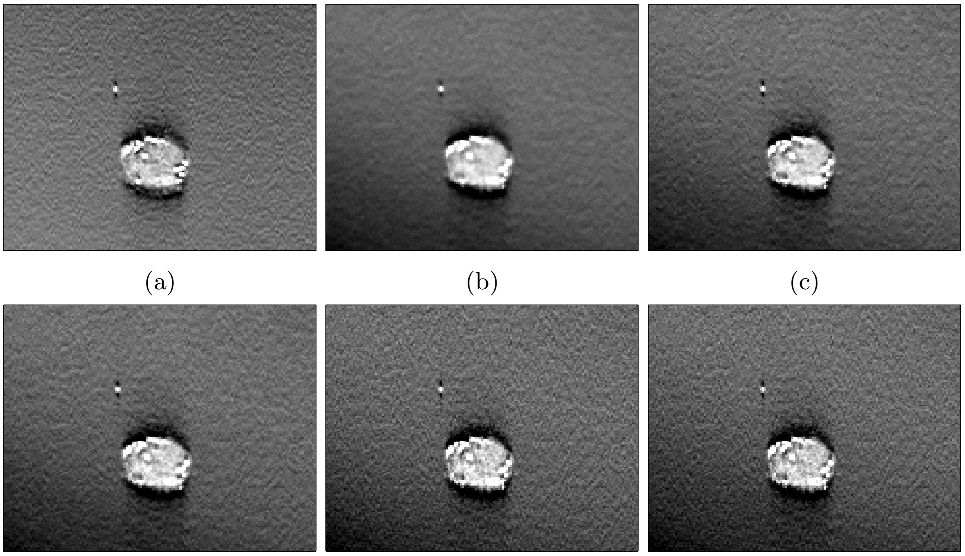
(a) (b) (c)

(d) (e) (f)

Figure 5.4. Reconstructed micro-calcification between our proposed methods with various parameter choices and some representative methods. (a) FBP (b) statistical IR with $p = 1.8, c^p = 2$ (c) statistical IR with $p = 1.61, c^p = 3.5$ (d) statistical IR with quadratic regularization (e) OS-EM (f) SART

vide better artifacts suppression around objects than FBP. In addition, the OS-PPL with $p = 1.8, c^p = 2$ presents best noise reduction among all investigated methods. In Fig. 5.4, the micro-calcifications can be clearly seen with statistical iterative methods, while FBP yields a little blurred sharpness along horizontal direction.

5.3 DISCUSSION

Statistical iterative reconstruction exhibits particular promising since it provides the flexibility of accurate physical noise modeling and geometric system description in transmission imaging system. In our previous study, OS-PPL reconstruction with a quadratic penalty was proposed to provide predictable image quality of reconstructed results, where the trade-off between resolution and noise can be controlled by adjusting the scalar λ based on a pre-computed look-up table. In this study, to reduce the noise without significant resolution loss, an edge-preserved regularizer was proposed to our OS-PPL method with a sDBT system. Two extra parameters are introduced to make tuning image quality more flexible and achievable. Influence function is presented to visualize the effect of these parameters on resolution. Experiment results show that by the proposed regularizer, resolution can be retained as much as possible while noise is reduced by tuning the parameter p and c. This benefit may allow to reduce the X-ray dose while maintaining a comparable image quality. Further experiments are needed to seek an optimal parameter combination. In addition, dose reduction experiments could be conducted with the inspiration of the edge-preserved iterative technique.

CHAPTER 6

METHOD FOR THE PARAMETER OPTIMIZATION OF ORDERED SUBSETS (OS) SEPARABLE PARABOLIC SURROGATE ALGORITHM (SPS)

6.1 ALGORITHM OF OS METHOD

Theoretically speaking, IQ is completely dominated by parameters λ, p, c in statistical IR method. But in practical applications, the optimal solution is almost impossible to be achieved. As introduced in chapter 2, an iterative method can hardly reach the optimum solution in limited iterations. To approach the convergence as much as possible in limited iterations. Ordered Subsets framework is studied with SPS algorithm in this chapter. Literature [1] indicated that OS method could speed up EM-type algorithms in the early iterations by using the sub-gradient to replace the true gradient, but usually exhibits limit-cycle like behavior near the optimal value. Next the authors proposed that by using a proper diminishing relaxation step-size, OS can yield a global convergence. The sufficient conditions on a relaxation for global convergence are the following:

$$\sum_{n}^{\infty} a_n = \infty, \sum_{n}^{\infty} a_n^2 < \infty, \tag{6.1}$$

where a_n is a relaxation parameter at the n-th iteration.

Let NS be the number of subsets. Let $S_1, ..., S_{NS}$ denote the subsets. Each S_i has M_{S_i} X-ray beams. In each iteration, the relaxation parameter is updated by:

$$a_n = \frac{1}{rn+1}, \tag{6.2}$$

which meets the sufficient conditions of global convergence. One iteration is completed when the algorithm goes through all the projections by going through all the subsets.

In our study, we employ the SPS based PPL method described in chapter 4 with OS framework. In each subset, the iterative solution is similar to (4.9) but gradient and scaled terms are calculated using the subset of data and $1/NS$ penalty. κ^2 is precomputed before iterations. We refer to the relaxed ordered subsets PPL method as relaxed OS-PPL. In our implementation, we use linked chain $RayPath_i$ to store the sparse matrix A, so that the memory consumption is reduced and accessing l_{ij} in A is also expedite. We summarize the main steps of our algorithm as follows:

```
for each pixel $j = 1, ..., N$ do
    update $\kappa^2$ by (4.8)
end for
for each iteration $n = 1, ..., Niter$ do
    update $a_n$ by (6.2)
    for each subset $s = 1, ..., NS$ do
        for each X-ray $i = 1, ..., M_{s_i}$ do
            while $RayPath_i \neq null$ do
                $att_i + = l_{ij}\mu_j$
                $len_i + = l_{ij}$
            end while
        end for
        for each X-ray $i = 1, ..., M_{s_i}$ do
            while $RayPath_i \neq null$ do
                $up_j + = l_{ij}(d_i e^{-att_i} - y_i)$
                $down_j + = l_{ij} len_i y_i$
            end while
        end for
        $\mu^{old} = \mu$
        for each pixel $j = 1, ..., N$ do
            $denom = down_j + 2\lambda|N_j|/M$
            $nom = up_j + \lambda\kappa^2 \sum_{k \in N_j}(\mu_j^{old} - \mu_k^{old})/NS$
        $\mu_j = [\mu_j^{old} + a_n * (nom/denom)]_+$
      end for
    end for
  end for
```

We can easily parallelize the algorithm by partitions of a projection image or groups of reconstructed planes.

6.2 SEMI-QUANTITATIVE OPTIMIZATION ON A SIMULATED PHANTOM

The convergence of OS-PPL lead to definite resolution properties based on the discussions above. However for 3-D reconstruction in a real application, even the relaxed OS can not guarantee the optimal in limited iterations. Moreover the undetermined parameters in relaxed OS such as a_n and subset organization may result in a convergence deviated from the true one [1]. Hence the resolution properties has a certain bias from the theoretical inevitably. Finding an optimal parameter combination is necessary for sufficient image qualities in limited iterations. It is intractable to quantify the impact of these parameters on image qualities, since they all rely on datasets. However, literature [69] revealed that the convergence of EM-type methods highly depend on the ratio of missing information to complete information. The ratio in our application is associated to the geometric configuration and weakly relevant to dataset. By studying a reasonable training set in our application, the undetermined parameters in OS are evaluated in advance and therefore the evaluated combination are ready for further usages.

With respect to the semi-quantitative evaluation, we employ objective function as a function of iteration, noise as a function of contrast and Artifact Spread Function (ASF) to represent the impacts of the parameters. To get a practical demonstration, we design an experiment by using the same system as shown in Fig. 4.1. The training phantom in the experiment is with a linear attenuation coefficient of $0.005mm^{-1}$ and with the side length of $20cm$ and the thickness of $2cm$. Two focus planes appear at the thickness of $0.5cm$ and $1.5cm$. On each of the planes, two cubes with the linear attenuation coefficients of $0.038mm^{-1}$ and $0.08mm^{-1}$ and with the side length of $6cm$ and the thickness of $0.25cm$ are located symmetrically. Four tiny ball are arranged vertically between the two cubes on each focus plane with the radii of $2.5mm$, $1.5mm$, $1.25mm$ and $0.56mm$, and with the linear attenuation coefficients of $0.02mm^{-1}$, $0.025mm^{-1}$, $0.05mm^{-1}$ and $0.1mm^{-1}$. The phantom is placed at $3cm$ away from the detector surface such that the focus planes appear at the height of 3.5cm and 4.5cm in the system. The projections are generated by a incident value under Poisson distribution and an illumination model. $\lambda = 16$ is chosen for the experiment. Through the Tables 4.2 and 4.1, one can predict that when PPL converges to the optimum, the pixel precision is approximately 0.397 with a drop of 37.5% compared to the method with $\lambda = 0$, or a ML-EM method and the noise is significantly decreased by 64.7%.

In this demonstration, we investigate the relaxation a_n with $r = 1, 4/5, 1/2, 0$ and subsets with $NS = 1, 5, 25$. All relaxed OS-PPLs run 20 iterations with a FBP initialization. For comparisons, a name rule is applied. For example, relaxed OS-PPL with $\lambda = 0$, subset of 1 and $r = 1/2$ is named as OS-PPL-λ0-sub1-r12. The curves of objective function as a function of iteration, noise as a function of contrast and Artifact Spread Function (ASF) are plotted to compare the impacts of selective parameter combinations on the convergence, image contrast and the removal of out-of-plane blur. Some representative reconstructions are also presented for the comparisons. These methods include BP, FBP, SART with a relaxation parameter, and OS-ML with subsets of 25 and $r = 1/2$.

Fig. 6.1 presents the convergence of OS-PPL and PPL. Generally speaking, OS-PPLs outperform PPL in terms of convergence in 20 iterations. Among OS methods, they diverge to different objective values in spite of the same λ. OS-PPL-λ16-sub5 has a larger value than the other two, while both OS-PPL-λ16-sub25-r45 and OS-PPL-λ16-sub25-r12 approach to a similar one, but the latter yields a faster convergence rate. The

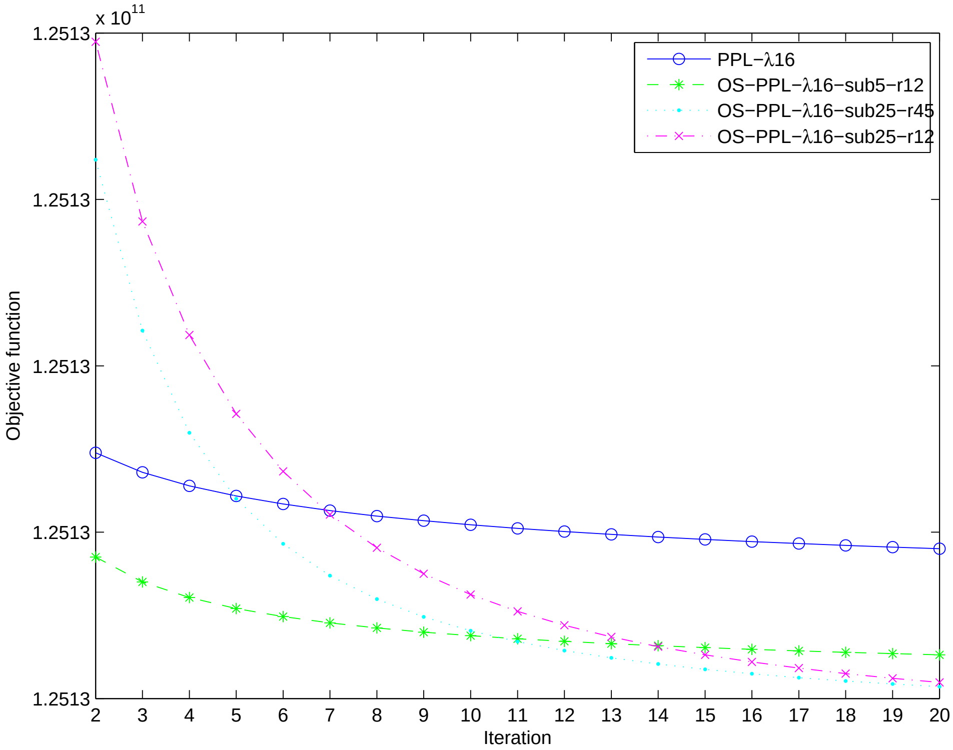

Figure 6.1. Objective function as a function of iteration with OS-PPL-λ16

observations above justify that (1) the relaxed OS-PPL methods lead to a faster convergence than PPL and (2) the parameters in OS-PPL may result in a divergence from the true one in spite of the same λ.

Fig. 6.2 shows the noise versus the image contrast as iteration increases. Noise reconstructed by SART and OS-ML increases dramatically with the incremental iterations. In a contrary, noise from OS-PPL tends to declination in the role of λ. Among OS methods, noise at the 20-th iterations approaches to a similar level due to the same λ, but has a slight deviation to each other, which confirms that the parameters in OS-PPL may lead to noise within a perturbation from the theoretical. On the other hand, the image contrast of OS methods settles in a small range around 0.016, where OS-PPL-λ16-sub25-r12 performs the best.

ASF is also employed to demonstrate the removal of out-of-plane blur of OS-PPL

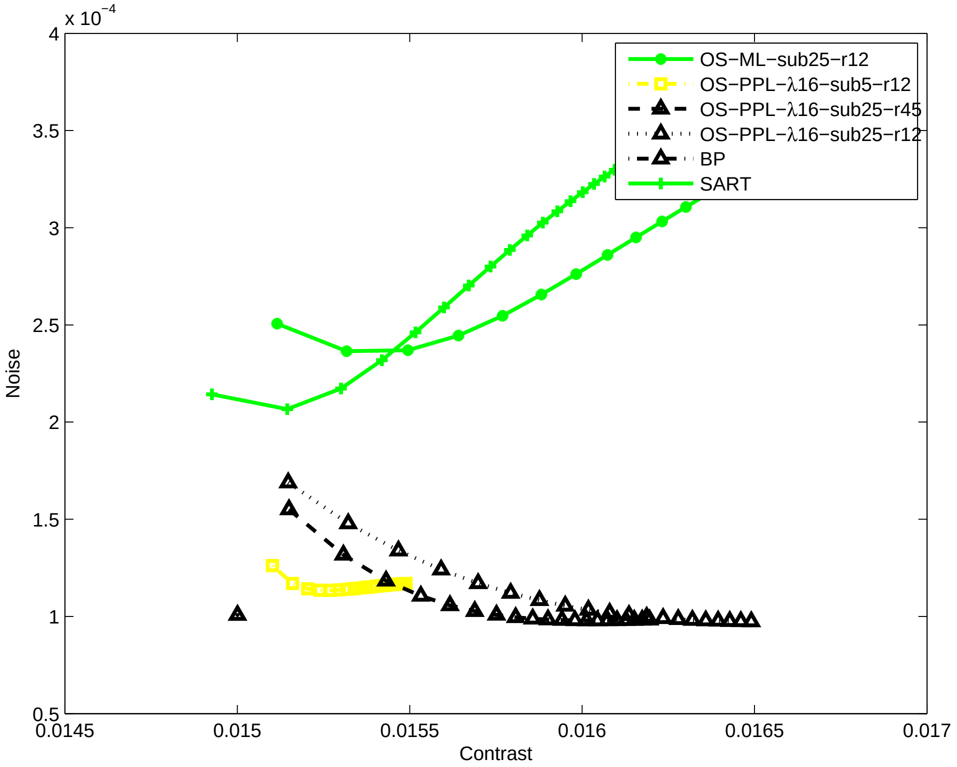

Figure 6.2. Comparisons of noise versus contrast with iteration increasing between OS-PPL and representative methods

methods with selective parameters. Figs. 6.3 and 6.4 show ASF at the 15-th and 20-th iteration respectively. In these figures, OS-ML and SART exhibit the best and similar performance. OS-PPLs with all selective combinations have no significant difference with each other. Moreover, OS-PPL with 20 iterations does not improve ASF significantly compared to the one with 15 iterations.

Based on the evaluations above, for $\lambda = 16$, one can choose subsets of 25 and $r = 1/2$ as the optimal combination, since they exhibit outstanding convergence and prominent performance of noise versus contrast. Additionally, because 20 iterations do not bring more benefits than 15 iterations in terms of noise, contrast and ASF, one can use OS-PPL with 15 iterations.

For practical applications, we perform the two-step procedure together with the semi-quantitative evaluation to obtain a desired image quality. The smoothing param-

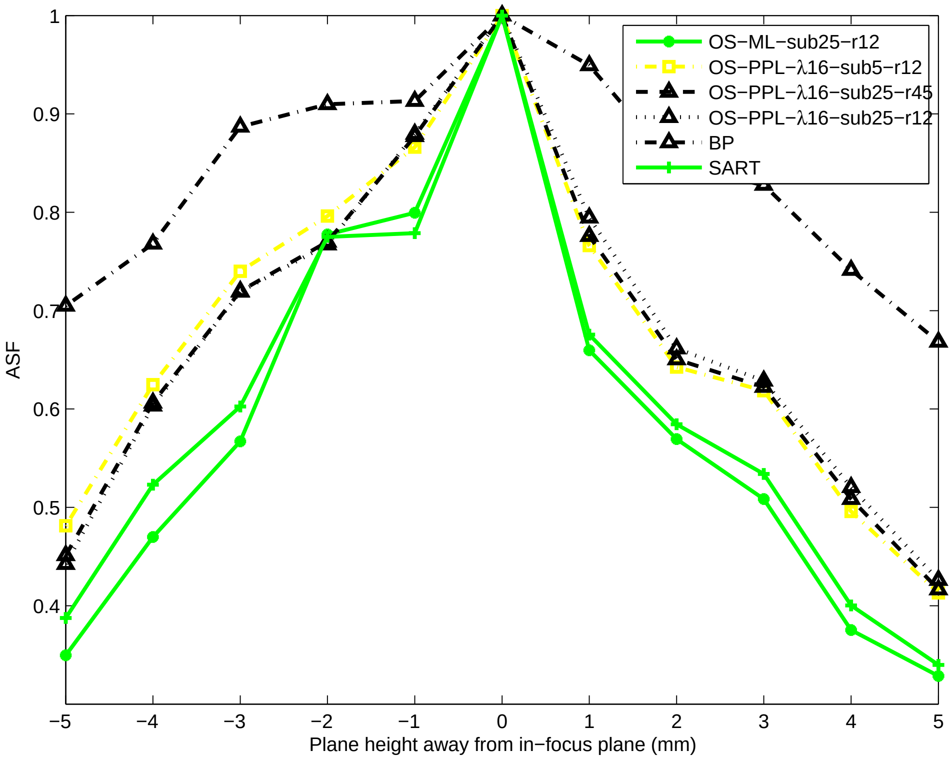

Figure 6.3. Comparisons of ASF between OS-PPL with 15 iterations and representative methods

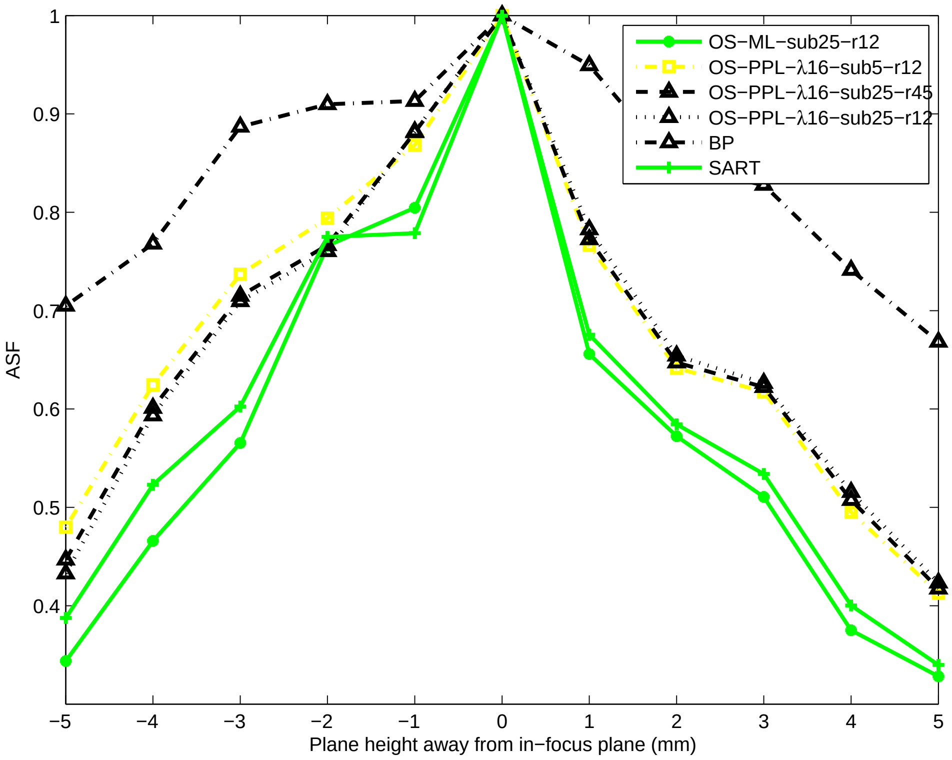

Figure 6.4. Comparisons of ASF between OS-PPL with 20 iterations and representative methods

eter λ chosen from the look-up tables generated in STEP 1 dominates the noise level and pixel precision, while the optimal parameter combination in OS evaluated through a training phantom can make practical results as consistent as possible with the theoretical one in less computational resources.

6.3 SIMULATION EXPERIMENTS

In this section, we demonstrate how the two-step procedure works with the semi-quantitative evaluation. The testing phantom used in this section is structurally identical with the training phantom, but the attenuation coefficients of objects have a 0.005 offset. This represents a practical deviation of a real object from training phantom. Visual comparisons of reconstructed results are reported between relaxed OS-PPL with chosen parameter combination and other representative methods such as FBP, OS-ML and OS-SPS [1]. Furthermore, The curve of contrast versus noise is plotted to check the consistence of the parameter impact on image qualities between testing phantom and training phantom.

In STEP 1, $\lambda = 16$ is chosen from the look-up tables 4.1 and 4.2. Based on the evaluations in Figs. 6.1, 6.2 and 6.3, OS-PPL with NS=25, $r = 1/2$ and 15 iterations produces a sufficient convergence, prominent image contrast, yet lower computational cost.

In STEP 2, OS-PPL with chosen parameter combination is applied. The focus plane reconstructed by it is shown in Fig. 6.5. For comparisons, the results from FBP, relaxed OS-SPS with $\lambda = 100000$ and a quadratic penalty, and relaxed OS-ML are shown in Figs. 6.6, 6.7, 6.8 respectively. Firstly, the image contrast between the on-plane cubes pointed by the arrows of 2 and 3 is much stronger in Figs. 6.5, 6.7, 6.8 than the ones in Fig. 6.6. Secondly, the edges pointed by the arrow 1 is enhanced clearly but shows obvious artifacts in the FBP result. Among Fig. 6.5, Fig. 6.7 and Fig. 6.8, OS-PPL and OS-SPS shows less sharp edges due to the smoothing effect of λ. But, the noise recon-

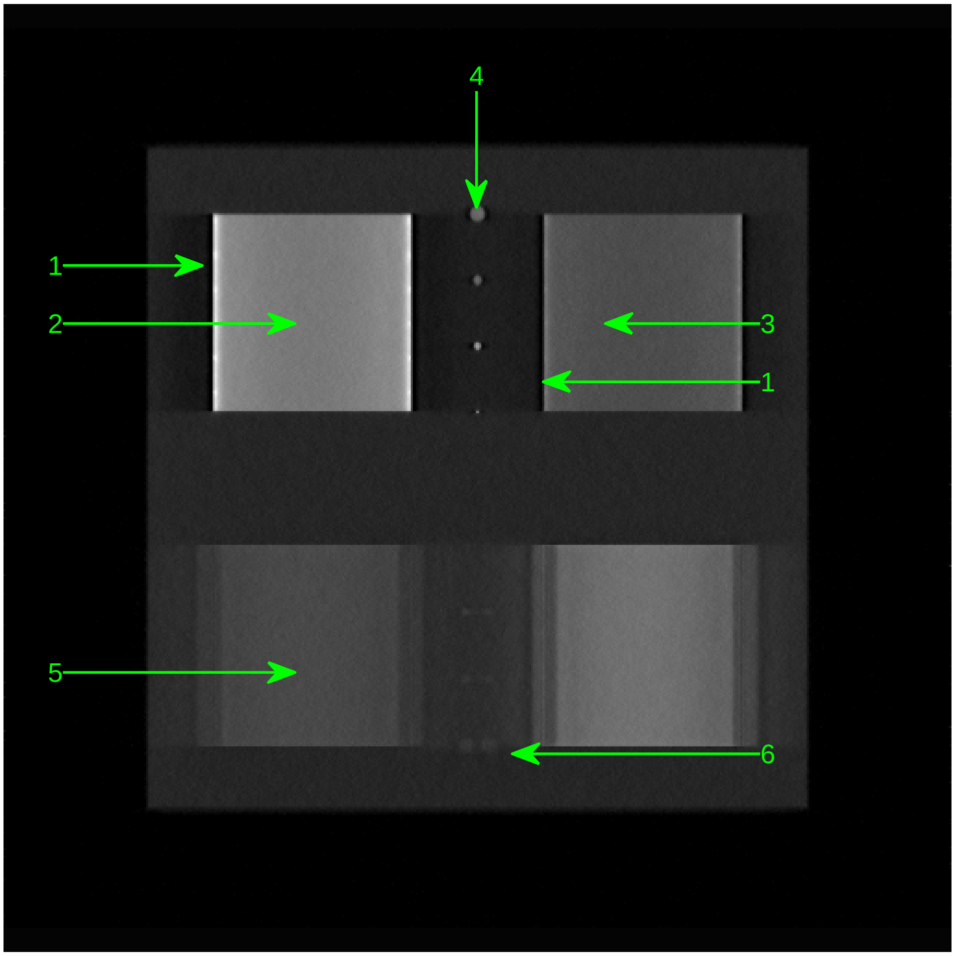

Figure 6.5. relaxed OS-PPL-λ16-sub25-r12 reconstruction on the focus plane at the height of $35mm$.

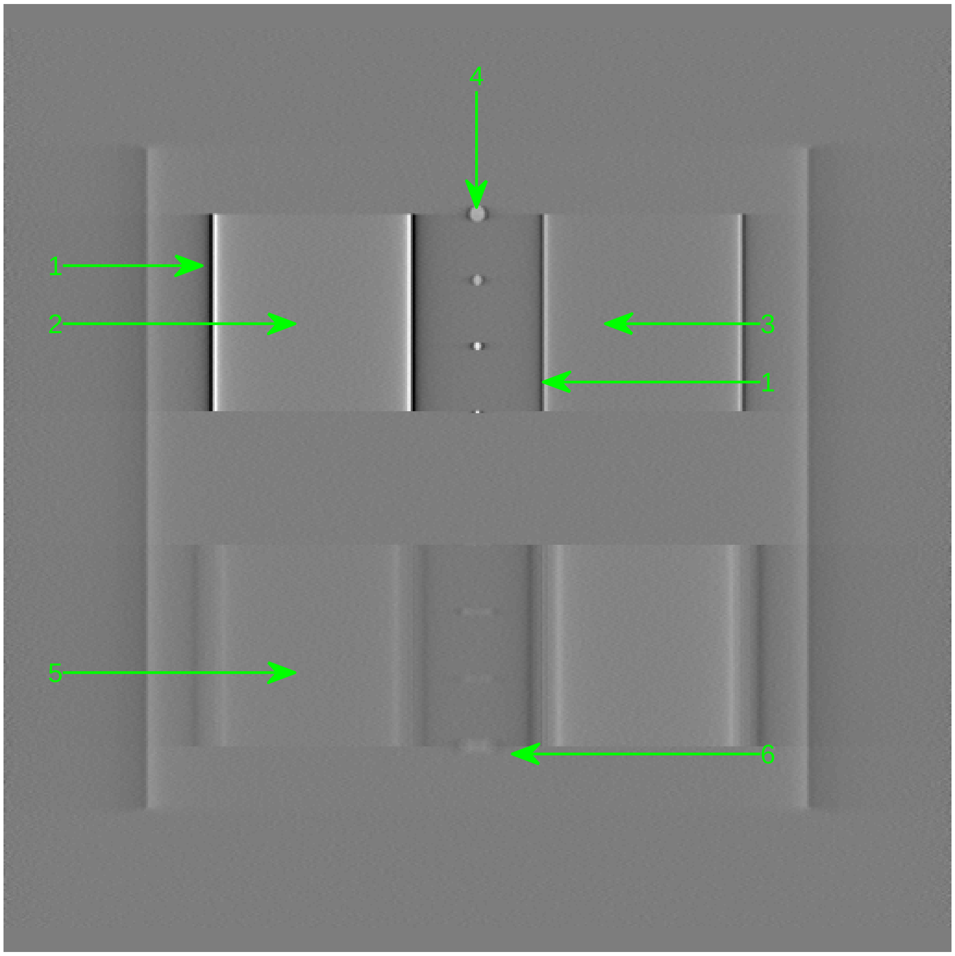

Figure 6.6. FBP reconstruction on the focus plane at the height of $35mm$.

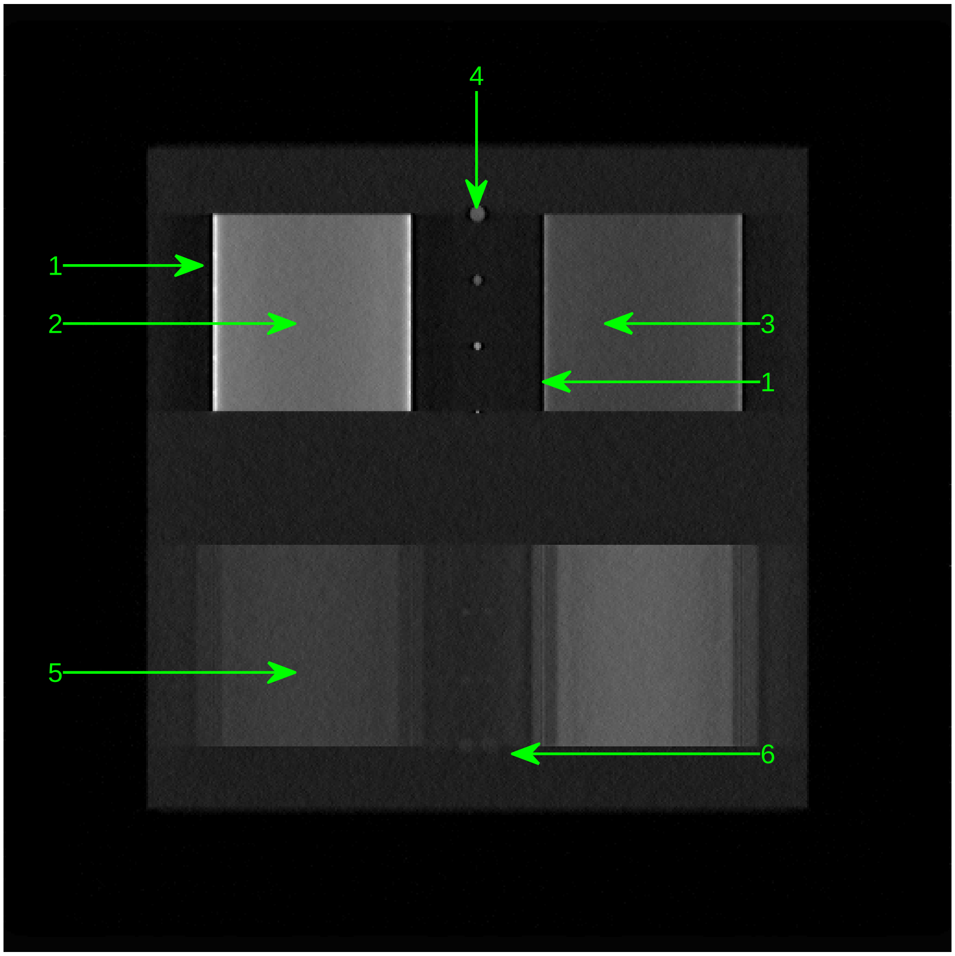

Figure 6.7. relaxed OS-SPS reconstruction with $\lambda = 100000$ weighting a quadratic penalty on the focus plane at the height of $35mm$.

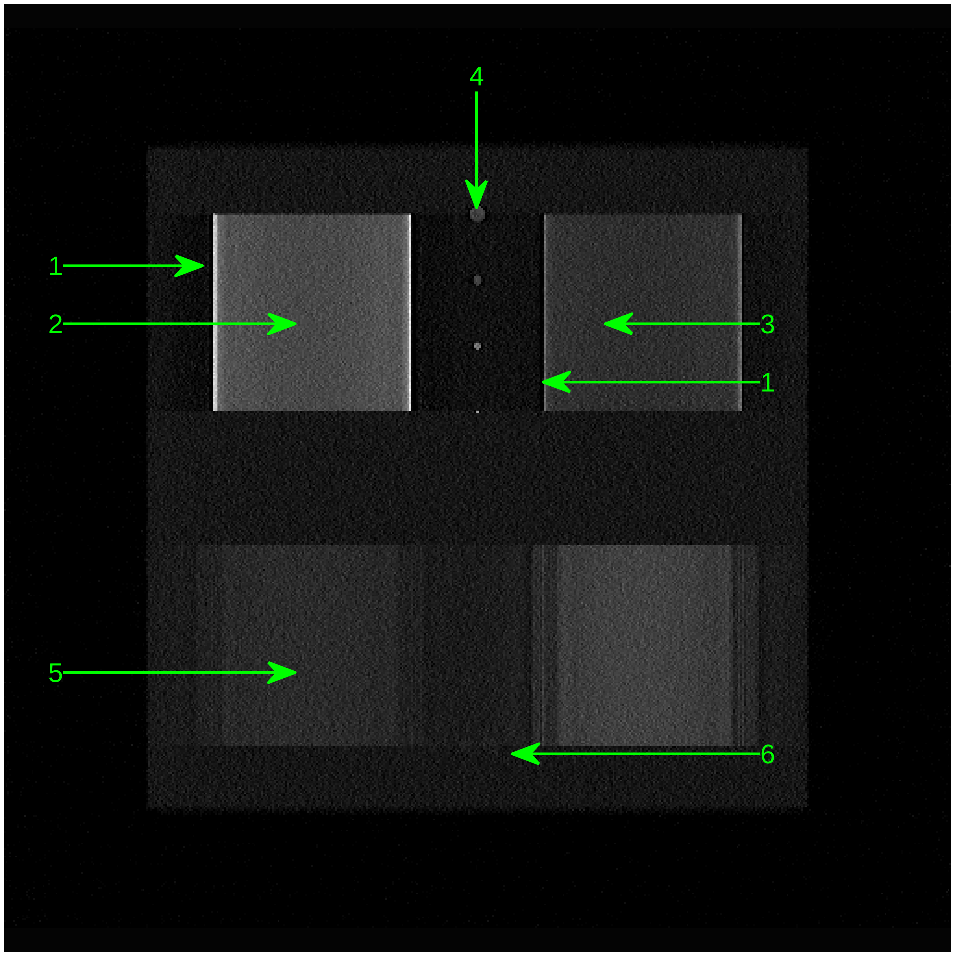

Figure 6.8. relaxed OS-MLEM reconstruction the focus plane at the height of 35mm.

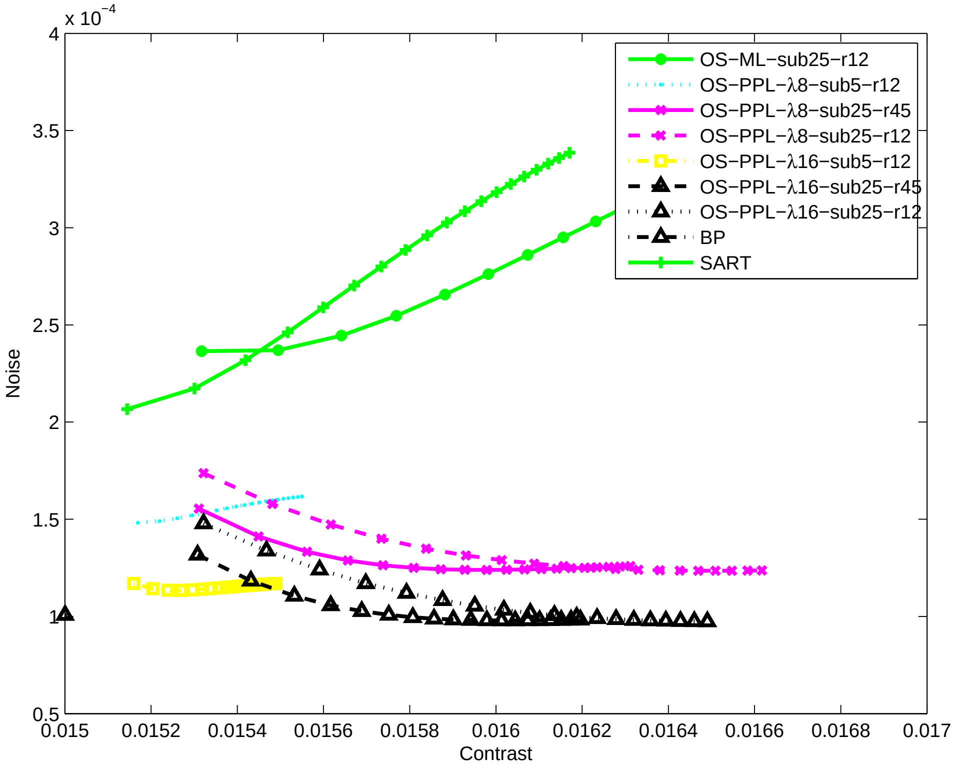

Figure 6.9. Comparisons of noise versus contrast between OS-PPL and representative methods on the testing phantom.

structed by them is much lower than the ones reconstructed by OS-ML. Additionally, although OS-SPS yields comparable resolution properties with OS-PPL, the effect of λ of OS-SPS is unpredicted. $\lambda = 100000$ is chosen by experiments, which is hard to be decided since its large range and dependence on the incident X-ray energy and objects. Last, the part pointed by the arrows of 5 and 6 are both out-of-plane blur which is “shadows” from the objects on the other planes. Although Fig. 6.6 seems to show a decent ability to remove the out-of-plane blur, the poor contrast leads to the obstacle to distinguish the objects on focus plane and out of plane.

Fig. 6.9 shows noise versus contrast of OS-PPL with selective parameters on testing phantom. As expected, OS-PPL on both testing phantom and training phantom achieve the same noise at the convergence due to the data-independent impact of λ, Moreover, the image contrast shown in Fig. 6.2 and Fig. 6.9 is quite similar at the convergence.

This confirms that the effects of relaxation factor and subset are weakly data-dependent.

6.4 DISCUSSION

In this chapter, relaxed OS framework was applied on PPL. Since the undetermined parameters in OS may lead to an image quality deviated from the theoretical, a semi-quantitative evaluation on a training phantom is proposed. The impacts of parameters are characterized by curves measured on the reconstructed training phantom. Experimental results illustrate the effectiveness of the two-step procedure and the semi-quantitative evaluation. Further work will be conducted to perform experiments on real phantom data to prove its performance in real application.

CHAPTER 7

LOCAL CONVERGENCE ANALYSIS OF THE OPTIMIZATION TRANSFER AND SUCCESSIVELY OVER-RELAXATION OPTIMIZATION TRANSFER

7.1 OPTIMIZATION TRANSFER

In the last chapter, a semi-quantitative method was proposed to optimize a relaxed OS method. However, OS based algorithm can not lead to the global convergence, even though the relaxation is applied since only partial data is used for each update of voxels. A global optimal method is usually taking up all data sets but leading to a slow convergence and intensive computation. In this chapter, a global method with a faster convergence and comparable computational intensity in each iteration will be discussed.

To motivate the new algorithm we start from minimizing the objective function (3.2), one can estimate the optimal μ^*, which is formulated as follows:

$$u^* = \arg\min_{\mu \geq 0} \Psi(\mu). \tag{7.1}$$

To solve the problem directly is intractable in real applications. Literature [29] proposed the concept of optimization transfer, where a series of surrogate functions bounded by the objective one are conceived and in turn minimizing (3.2) has been transferred to the minimization of the surrogate ones. We re-summarize the optimization transfer as a algorithm scheme for later usage:

```
for each iteration $t = 1, ..., Niter$ do
    Find an surrogate function $G(\Theta, \Phi)$ satisfying,
    (1) $G(\Theta^t, \Theta^t) = \Psi(\Theta^t)$,
    (2) $\Psi(\Theta) \leq G(\Theta, \Theta^t), \forall \Theta^t \neq \Theta$,
    we apply one step of Newton's method on the surrogate, the optimal approximation
```

at $(t+1)$-th iteration is written as

$$\Theta^{t+1} = \Theta^t - \nabla^2_\Theta G(\Theta^t, \Theta^t)^{-1} \nabla_\Theta G(\Theta^t, \Theta^t), \tag{7.2}$$

end for

Literature [29] proposed parabolic surrogates with non-separable variables and optimal surrogate curvatures, which yield a faster convergence but non-parallel computations. Literature [28, 1, 77] reported a separable parabolic surrogate (SPS) with ordered subsets (OS) accelerations. An optimal curvature, which is the minimum curvature holding the "bounded" condition, can be estimated in advance. The precomputed curvature (PC) can be applied in the demonstrated ML case by replacing $d_i e^{-<\mu^{(n)}, li>}$ in the denominator by y_i in (2.24), which produces an "almost always" monotonically decreasing algorithm. However even the PC-SPS still undergoes a sub-linear convergence. Is there a better method to outperform the optimization transfer based methods yet ensure the monotonicity and parallel computations?

7.2 CONVERGENCE RATE ANALYSIS

To answer the question, a local convergence rate of the optimization transfer is derived and is associated with quasi-Newton behavior in this section. Before that we present a simple proof sketch of the global convergence for the optimization transfer by ignoring the non-negative constraint.

Proof. Let $\Theta^{t+1} = \arg\min_\Theta G(\Theta^t, \Theta^t)$, then $\Psi(\Theta^{t+1}) = G(\Theta^{t+1}, \Theta^{t+1}) \leq G(\Theta^{t+1}, \Theta^t) \leq G(\Theta^t, \Theta^t) = \Psi(\Theta^t)$. Hence $\Psi(\Theta^t)$ decreases monotonically as $t \to \infty$. Additionally $\exists \Theta^* \in \mathbb{R}^n, \Psi(\Theta^*) \leq \Psi(\Theta^t)$ for $\Psi(\Theta)$ is convex. Therefore $\lim_{t\to\infty} \Psi(\Theta^t) = \inf \Psi(\Theta^t) = \Psi(\Theta^*)$ by the convergence of a monotonic sequence of real number. In fact, $\lim_{t\to\infty} \Theta^t = \Theta^*$ for $\Psi(\Theta)$ is continuous. □

Literature [51] reported that the local convergence of an EM method exhibited a linear gradient behavior, however no further discussion was involved to improve the performance. Literature [29] showed that through minimizing the curvature, which still hold the "bounded" condition for each surrogate function, the iterative solution gain a larger step for each iteration. Actually parabolic and "bounded" are not necessary and a more general case should be considered. To develop the idea and provide possible solutions, a local convergence theorem for the optimization transfer is proposed based on Banach fixed-point theorem.

Theorem 7.2.1. (Local convergence Theorem) *For the optimization transfer, let* $(\mathbb{R}^n, \|\|_2)$ *be a metric space. Then* $\exists A \subseteq \mathbb{R}^n$, $(A, \|\|_2)$ *is closed and bounded, such that* $\exists\ T : \Theta \mapsto \Theta'$ *is a contraction mapping on* A*. Therefore* $\exists!\ \Theta^* = T(\Theta^*, \Theta^*) \in A$ *and* $\Psi(\Theta^*) \leq \Psi(\Theta)$*.*

Proof. We define a mapping according to the iterative solution (7.2) as follows:

$$T(\Theta, \Phi) = \Theta - \nabla^2_\Theta G(\Theta, \Phi)^{-1} \nabla_\Theta G(\Theta, \Phi). \tag{7.3}$$

It is true that $\Theta^* = T(\Theta^*, \Theta^*)$ by the proof of the global convergence. For $\forall \Theta_1^{t-1}, \Theta_2^{t-1} \in \mathbb{R}^n$ where t is the t-th iteration, we can get

$$\begin{aligned}
&\Theta_1^t - \Theta_2^t = T(\Theta_1^{t-1}, \Theta_1^{t-1}) - T(\Theta_2^{t-1}, \Theta_2^{t-1}) \\
= \;\; & T(\Theta_1^{t-1}, \Theta_1^{t-1}) - T(\Theta_1^{t-1}, \Theta_2^{t-1}) \\
& + T(\Theta_1^{t-1}, \Theta_2^{t-1}) - T(\Theta_2^{t-1}, \Theta_2^{t-1}) \\
= \;\; & (\nabla_\Phi T(\Theta_1^{t-1}, \varepsilon_1) + \nabla_\Theta T(\varepsilon_2, \Theta_2^{t-1}))(\Theta_1^{t-1} - \Theta_2^{t-1}),
\end{aligned} \tag{7.4}$$

where $\varepsilon_1 = (1 - C_1)\Theta_1^{t-1} + C_1 \Theta_2^{t-1}$ and $\varepsilon_2 = (1 - C_2)\Theta_1^{t-1} + C_2 \Theta_2^{t-1}$, $C_1, C_2 \in [0, 1]$. Then we calculate $\nabla_\Phi T(\Theta, \Phi)$ and $\nabla_\Theta T(\Theta, \Phi)$ and substitute them the equation above.

$$\begin{aligned}
&\Theta_1^t - \Theta_2^t = ((-\nabla^2_\Theta G(\Theta_1^{t-1}, \varepsilon_1)^{-1} \nabla^2_{\Theta,\Phi} G(\Theta_1^{t-1}, \varepsilon_1) \\
&+ \nabla^2_\Theta G(\Theta_1^{t-1}, \varepsilon_1)^{-2} \nabla^3_{\Theta^2,\Phi} G(\Theta_1^{t-1}, \varepsilon_1) \nabla_\Theta G(\Theta_1^{t-1}, \varepsilon_1)) \\
&+ (\nabla^2_\Theta G(\varepsilon_2, \Theta_2^{t-1})^{-2} \nabla_\Theta G(\varepsilon_2, \Theta_2^{t-1}) \nabla^3_\Theta G(\varepsilon_2, \Theta_2^{t-1}))) \\
&(\Theta_1^{t-1} - \Theta_2^{t-1}).
\end{aligned}$$

Let $\Theta_1^t = \Theta^*$ and $\Theta_2^t = \Theta^t$. When $\Theta^{t-1} \to \Theta^*$, $\nabla_\Theta G(\Theta^*, \Theta^*) = 0$. Hence $\Theta^* - \Theta^t = K(\varepsilon_1, \varepsilon_2)(\Theta^* - \Theta^{t-1})$, where

$$\lim_{\Theta^{t-1} \to \Theta^*} K(\varepsilon_1, \varepsilon_2) = -\nabla_\Theta^2 G(\Theta^*, \Theta^*)^{-1} \nabla_{\Theta,\Phi}^2 G(\Theta^*, \Theta^*). \tag{7.5}$$

We can construct such a $G(\Theta, \Phi)$ that $||K(\Theta^*, \Theta^*)||_2 \leq 1$ when $\Theta \in A := N(\Theta^*)$ which is closed and bounded. T is a contraction mapping on A. So $\exists! \Theta'$ which is the fixed point by Banach fixed-point theorem, such that $\Theta' = T(\Theta', \Theta')$ where $\Theta' = \Theta^*$. □

Through the theorem, when Θ is close enough to the optimum Θ^*, there must be a contraction mapping in the form of (7.2) to guarantee the existence of the fixed point. The local convergence rate $r = \lim_{t\to\infty} \frac{||\Theta^* - \Theta^{t+1}||_2}{||\Theta^* - \Theta^t||_2} \leq ||K(\Theta^*, \Theta^*)||_2$ can be evaluated by the approximation (7.5), which is the convergence rate matrix. r is boosted as the largest eigenvalue of the convergence rate matrix $K(\Theta^*, \Theta^*)$ is approaching to 0.

To find the upper limit of the convergence rate of the optimization transfer, we associate it with the convergence behavior of quasi-Newton method by the following corollary

Corollary 7.2.2. *When (7.2) is represented as*

$$\Theta^{(t+1)} = \Theta^{(t)} - S(\Theta^{(t)}) \nabla_\Theta G(\Theta^{(t)}, \Theta^{(t)}), \tag{7.6}$$

$\lim_{\Theta^{(t)} \to \Theta^*} S(\Theta^{(t)}) = [I - K(\Theta^*, \Theta^*)] \nabla_\Theta^2 L(\Theta^*)^{-1}$ *where I is an identity matrix.*

Proof. Theorem 7.2.1 tells us the contraction mapping

$$T(\Theta, \Phi) = \Theta - \nabla_\Theta^2 G(\Theta, \Phi)^{-1} \nabla_\Theta G(\Theta, \Phi).$$

Based on it, we change (7.6) as follows

$$T(\Theta, \Theta) - \Theta \;\; = \;\; -S(\Theta) \nabla_\Theta G(\Theta, \Theta) = -S(\Theta) \nabla_\Theta L(\Theta),$$

since $\nabla_\Theta G(\Theta, \Theta) = \nabla_\Theta L(\Theta)$. Then derivatives are performed on both sides

$$\nabla_\Theta T(\Theta, \Theta) - I = -\nabla_\Theta S(\Theta) \nabla_\Theta L(\Theta) - S(\Theta) \nabla_\Theta^2 L(\Theta).$$

We know $\nabla_\Theta T(\Theta, \Theta) = K(\Theta, \Theta)$ and substitute it to the above equation and perform $\Theta \to \Theta^*$ on both sides

$$K(\Theta^*, \Theta^*) - I = 0 - \lim_{\Theta \to \Theta^*} S(\Theta) \nabla^2_\Theta L(\Theta^*).$$

The corollary has been proved

$$\lim_{\Theta \to \Theta^*} S(\Theta) = [I - K(\Theta^*, \Theta^*)] \nabla^2_\Theta L(\Theta^*)^{-1}. \tag{7.7}$$

□

From (7.7) one can see when $K(\Theta^*, \Theta^*)$ has small eigenvalues, the optimization transfer shows quasi-Newton-like convergence. In particular, if the largest eigenvalue of $K(\Theta^*, \Theta^*)$ approaches to 0, the optimization transfer turns to a quasi-Newton method which is

$$\Theta^{(t+1)} = \Theta^{(t)} - \nabla^2_\Theta L(\Theta^{(t)})^{-1} \nabla_\Theta L(\Theta^{(t)}).$$

To apply the local convergence theorem and its corollary on a particular optimization transfer based method, an example of ML-EM is given. The surrogate function $G(\mu, \mu^n)$ in (2.23) is reparameterized by:

$$G(\Theta, \Phi) = \sum_{i=1}^{M} (\sum_{j=1}^{N} \ell(\frac{l_{ij}}{a_{ij}}(\theta_j - \phi_j) + < \phi, l_i >)).$$

To check the local convergence rate of this method, we calculate $K(\Theta^*, \Theta^*)$ and estimate its eigenvalue. After derivative calculations, the form is given as follows:

$$\begin{aligned}
[K(\Theta^*, \Theta^*)]_{mn} &= -[\nabla^2_\Theta G(\Theta^*, \Theta^*)^{-1} \nabla^2_{\Theta,\Phi} G(\Theta^*, \Theta^*)]_{mn} \\
&= \begin{cases} \frac{\sum_{i=1}^M l_{im} d_i e^{-<\Theta^*, l_i>}(L_i - l_{im})}{\sum_{i=1}^M l_{im} d_i e^{-<\Theta^*, l_i>} L_i}, & \text{if } m = n \\[2ex] \frac{\sum_{i=1}^M l_{im} l_{in} d_i e^{-<\Theta^*, l_i>}}{\sum_{i=1}^M l_{im} d_i e^{-<\Theta^*, l_i>} L_i}, & \text{if } m \neq n \end{cases}
\end{aligned}$$

where $L_i = \sum_j^N l_{ij}$, which is the length of the intersection between the i-th X-ray and the object. Obviously $L_i \gg l_{ij}$, therefore the non-diagonal entries of $K(\Theta^*, \Theta^*)$ is approximated to 0, whereas the diagonal entries is close to 1. The nature of the matrix, which is $||K(\Theta^*, \Theta^*)||_2 \approx 1$, implies the ML-EM method converges sub-linearly near Θ^*.

For another example, we apply the theorem to study the convergence of OS-EM method. Let $S_1, ..., S_{NS}$ denote each subset, where NS is the number of the subsets. One iteration is completed when the algorithm goes through all the projections by going through all the subsets. For each subset, the gradient and scaled terms are calculated by using the current subset. For the i-th subset, the surrogate function $G_i(\Theta, \Phi)$ is shown as follows:

$$G_i(\Theta, \Phi) = \sum_{i=1}^{M_{S_i}} (\sum_{i=1}^{N} \ell(\frac{l_{ij}}{a_{ij}}(\theta_j - \phi_j) + < \phi, l_i >)),$$

where M_{S_i} is the number of X-ray of the i-th subset. The convergence rate matrix (7.5) is reparameterized as follows

$$K_i(\Theta^*, \Theta^*) = -\nabla^2_{\Theta} G_i(\Theta^*, \Theta^*)^{-1} \nabla^2_{\Theta,\Phi} G_i(\Theta^*, \Theta^*).$$

The convergence rate for one complete iteration is shown as below:

$$r = \lim_{t \to \infty} \frac{||\Theta^* - \Theta^t||_2}{||\Theta^* - \Theta^{t-1}||_2} \leq \prod_{i=1}^{NS} ||K_i(\Theta^*, \Theta^*)||_2,$$

which is far less than 1 and exhibits a super-linear convergence.

The analytical results for both ML-EM and OS-EM methods imply that the convergence rate highly depends on some system-related parameters, such as the incident X-ray intensity and the ratio between the mesh size and the length of X-ray intersecting with objects. A careful system design can help to improve the algorithm performance. For example, in Digital Breast Tomosynthesis [23], compressed boards can reduce the effective X-ray length, in turn may lead to a better algorithm performance. The incident energy level can also be adjusted carefully. However, we expect system-independent strategies to improve the convergence, since algorithms should not restrict the system design. In the next section, we propose an alternative optimization transfer with a new contraction mapping which breaks the limitations of the original one.

7.3 ALTERNATIVE OPTIMIZATION TRANSFER

Generally speaking, optimization transfer enjoys the strong guarantee "bounded" and never worsen the objective function, which makes the surrogate functions must be constructed with very conservative bounds, resulting in extremely slow convergence. In literature [29], the authors proposed the optimal curvature for a parabolic surrogate, which is minimum yet still "bounded". However, "bounded" is much more strict than "almost always monotonicity", which is sufficient for a global optimal. In another word, "bounded" is not necessary. To motivate an alternative optimization transfer which somewhat weakens the strong condition, we consider the contraction mapping below

$$R(\Theta, \Phi) := \Theta + \rho(T(\Theta, \Phi) - \Theta) = \Theta - \rho\nabla^2_\Theta G(\Theta, \Phi)^{-1}\nabla_\Theta G(\Theta, \Phi), \tag{7.8}$$

where $R(\Theta, \Phi)$ is the new contraction mapping which is coupled with the mapping T of the original optimization transfer. ρ is a factor re-scaling the iterative step along the gradient direction. If $\rho = 1$, the T-coupled R is degraded to the T. If $\rho > 1$, the T-coupled R gains a larger iterative step than the corresponding T. Does a larger ρ ensure "almost always monotonicity"? though it may not hold the "bounded". If so, how does it perform? To answer these questions, we need the corollary below

Corollary 7.3.1. *If T-coupled R with ρ converge to $R(\Theta^*, \Theta^*)$, then the convergence rate*

$$\begin{aligned} r &= \lim_{t\to\infty} \frac{||\Theta^* - \Theta^{t+1}||_2}{||\Theta^* - \Theta^t||_2} \\ &\leq max(|1 - \rho(1 - \lambda_{max})|, |1 - \rho(1 - \lambda_{min})|), \end{aligned} \tag{7.9}$$

where λ_{max} and λ_{min} are the largest and the smallest eigenvalues of $K(\Theta^*, \Theta^*)$.

Proof. $R(\Theta)$ is a contraction mapping, hence when $\Theta \in N(\Theta^*)$,

$$(\Theta^* - \Theta^{t+1}) = H(\Theta^*, \Theta^*)(\Theta^* - \Theta^t), \tag{7.10}$$

where $H(\Theta^*, \Theta^*) := \nabla R(\Theta^*, \Theta^*)$. Then

$$r = \lim_{t \to \infty} \frac{||\Theta^* - \Theta^{t+1}||_2}{||\Theta^* - \Theta^t||_2} \leq ||H(\Theta^*, \Theta^*)||_2$$

$H(\Theta^*, \Theta^*)$ can be shown by differentiating both sides of the new contraction mapping (7.8)

$$H(\Theta^*, \Theta^*) = I + \rho(K(\Theta^*, \Theta^*) - I),$$

where $||H(\Theta^*, \Theta^*)||_2 = \sigma_{max}$, and

$$\sigma_{max} = max(|1 - \rho(1 - \lambda_{max}|, |1 - \rho(1 - \lambda_{min})|), \tag{7.11}$$

which can be proved by the Raleigh quotient □

This corollary reveals the relationship between the convergence of T-coupled R and its counterpart T. For example, if $\lambda_{max} = 0.5$, which implies a convergence between the sub-linearity and the super-linearity, and $\rho = 2$, then the convergence rate r of the new mapping is 0, which produces a super-linear convergence. However, does this ρ ensure the global convergence? Through the corollary below, ρ in certain range is studied.

Corollary 7.3.2. *If the contraction mapping T converges to $T(\Theta^*, \Theta^*)$, then $\exists N(\Theta^*)$, such that its counterpart T-coupled R with $0 \leq \rho \leq 2$ are guaranteed to converge to $R(\Theta^*, \Theta^*)$, $\Theta \in N(\Theta^*)$.*

With the similar spirit in literature [8], we give the following sketch proof:

Proof. From Corollary 7.3.1, we know in a small region around Θ^*

$$||(\Theta^* - \Theta^{t+1})||_2 \leq \sigma_{max}||(\Theta^* - \Theta^t)||_2,$$

where σ_{max} denotes the largest eigenvalue of $H(\Theta^*, \Theta^*)$, and

$$\sigma_{max} = \max(|1 - \rho(1 - \lambda_{max})|, |1 - \rho(1 - \lambda_{min})|).$$

Any $0 \leq \rho \leq 2$, we have $\sigma_{max} \leq 1$. Therefore, T-coupled R converges to $R(\Theta^*, \Theta^*)$. $\square$

Based on the corollaries above, when $|1-\rho(1-\lambda_{max})| = |1-\rho(1-\lambda_{min})|$, a particular ρ^* called "the optimal relaxation" is produced, which yields the fastest convergence rate around Θ^*, which is

$$\rho^* = \frac{2}{2 - \lambda_{max} - \lambda_{min}}. \tag{7.12}$$

For $0 \leq \lambda_{min} \leq \lambda_{max}$, if λ_{max} is close to 1, the optimum $\rho^* > 2$, which means $0 \leq \rho \leq 2$ is not necessary and an optimal $\rho^* > 2$ may boost the convergence, when the convergence of T is extremely slow. For each iterative step, through the estimation of ρ^*, T-coupled R will shrink the distance $||\Theta^* - \Theta^{t+1}||$ by a factor of σ_{max}. After M steps, an exponential gain of $(\sigma_{max}/\ \lambda_{max})^M$ is obtained from the T-coupled R. Thus, a substantial improvement in convergence can be yielded by the T-coupled R with the optimal ρ^*. Unfortunately, direct estimation of ρ^* requires knowledge of the convergence rate matrix $K(\Theta^*, \Theta^*)$. The eigenvalues of it can be evaluated fairly efficiently using techniques similar to those used in literature [20]. However, without the optimal ρ^*, $1 \leq \rho \leq 2$ already ensures a faster convergence with a global optimal when the original mapping fells in extremely slow rate. Without exhausted computational cost on the evaluation of $K(\Theta^*, \Theta^*)$, several acceleration strategies are proposed in the next subsection.

7.3.1 Adaptive successively over-relaxation

We summarize the main steps of the algorithm scheme with an adaptive ρ as follows:

```
$\rho = 1$ and $a = \delta$ ($\delta$ can be adjusted in a specific case)
for each iteration $t = 1, ..., Niter$ do
```

```
    $\Theta_T^{t+1} = \Theta^t - \nabla_\Theta^2 G(\Theta^t, \Theta^t)^{-1} \nabla_\Theta G(\Theta^t, \Theta^t)$
    $\Theta_{TCR}^{t+1} = \Theta^t + \rho(\Theta_T^{t+1} - \Theta^t)$
    Calculate $\Psi(\Theta_T^{t+1})$ and $\Psi(\Theta_{TCR}^{t+1})$
    **if** $\Psi(\Theta_{TCR}^{t+1}) \leq \Psi(\Theta_T^{t+1})$ **then**
      $\rho* = a$ and $\Theta^{t+1} = \Theta_{TCR}^{t+1}$
    **else**
      $\rho = 1$ and $\Theta^{t+1} = \Theta_T^{t+1}$
    **end if**
  **end for**
```

In the algorithm framework, Θ_{TCR} by the contraction mapping T-coupled R can be solved along with Θ_T by the mapping T. The objective functions $\Psi(\Theta_T)$ and $\Psi(\Theta_{TCR})$ can be evaluated easily and partially free from computing Θ_T and Θ_{TCR}. Therefore few extra computations are incorporated into an original optimization transfer. The real solution Θ^{t+1} for the next iteration is determined by a update rule where if the objective value with Θ_{TCR} is less than the one with Θ_T. Θ is updated by Θ_{TCR} and ρ increases by multiplying the factor a. Otherwise Θ_T replaces Θ for the next iteration, whereas ρ is set as 1. In this way, an optimal performance is always gained in each iteration when the adaptive factor based T-coupled R method (AF-TCR) is used, so that the total acceleration ratio is significant after all the iterations. In particular, if non-negativeness is considered, the monotonicity may not be held due to the noisy data. However in practice, “almost monotonicity” is sufficient.

7.3.2 Constant successively over-relaxation

If the computational cost is critical, an alternative strategy with a free estimation can be applied. By a successive and constant step of ρ, the acceleration can also be obtained in each iteration without any extra estimation. However, it will be the slightly slow compared to adaptive one. The main steps of the conservative method is summarized as follows:

```
$\rho = 1$ and $a = \delta$ ($\delta$ can be adjusted in a specific case)
for each iteration $t = 1, ..., Niter$ do
    if $\rho >= 2$ then
        $\Theta_T^{t+1} = \Theta^t - \nabla_\Theta^2 G(\Theta^t, \Theta^t)^{-1} \nabla_\Theta G(\Theta^t, \Theta^t)$
        $\rho = 1$ and $\Theta^{t+1} = \Theta_T^{t+1}$
    else
        $\Theta_{TCR}^{t+1} = \Theta^t - \rho \nabla_\Theta^2 G(\Theta^t, \Theta^t)^{-1} \nabla_\Theta G(\Theta^t, \Theta^t)$
        $\rho * = a$ and $\Theta^{t+1} = \Theta_{TCR}^{t+1}$
    end if
end for
```

From the framework, the estimation of objective functions for the update rule is replaced by a successive and constant step of ρ, $\rho \in [1, 2]$. As the Corollary 7.3.2, $\rho \in [1, 2]$ is sufficient for a global optimal, when $\Theta \in N(\Theta^*)$. Therefore $\rho \in [1, 2]$ forces an superior rate through the contraction mapping T-coupled R in each iteration. Most importantly, the benefits from the constant factor based T-coupled R (CF-TCR) is almost free.

7.4 SIMULATION EXPERIMENTS

To assess the performance of the proposed algorithms, we perform 3-D reconstruction on a simulated dataset. A virtual system is set up to simulate a real limited angle X-ray tomography system. Fig. 7.1 demonstrates the geometric configuration of the system. The detector size is 28.672cm by 28.672cm with a 2.24mm pixel pitch. O is the origin of the 3-D coordinate system which is located at the center of the detector. The source to image distance (SID) along Z direction is set as 69.28cm and the distance between source to object (SOD) is 66.78cm. 25 x-ray beams are positioned in a straight line parallel to the detector plane along the X axis. The middle one of the 25 beams is located on Z axis and the linear spacing between these beams varies to provide a 2° an-

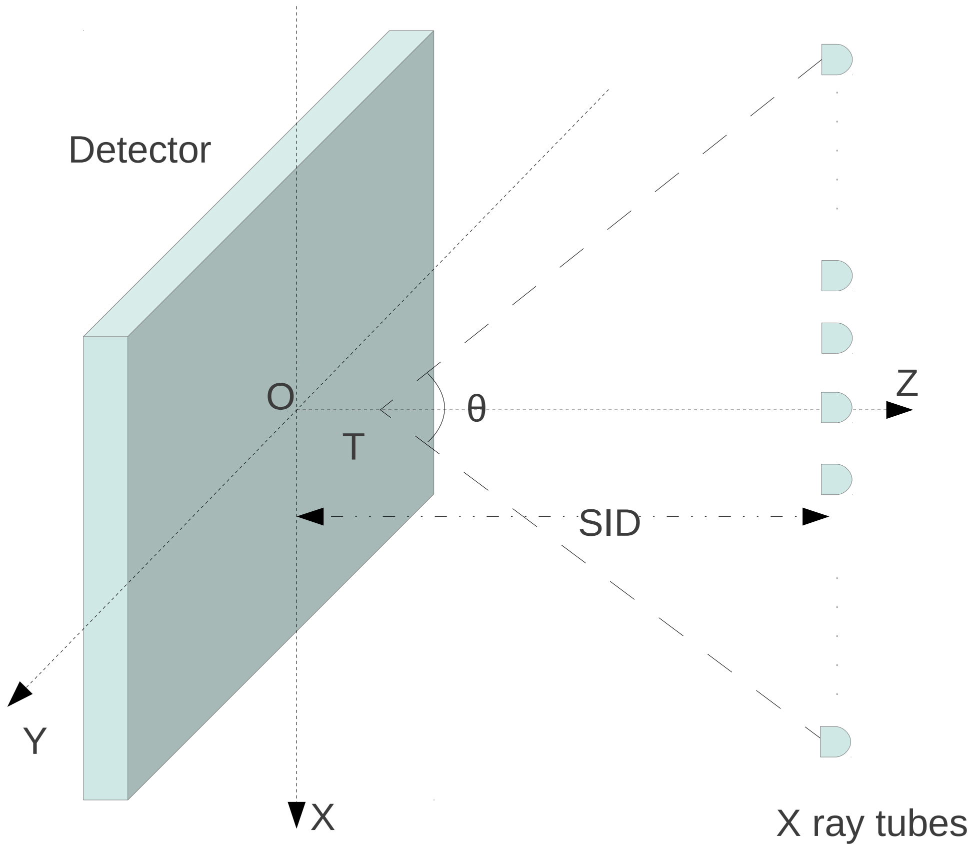

Figure 7.1. Geometry configuration of Digital Breast Tomosynthesis with multiple parallel X-ray beams.

gular spacing around the rotation center T. The system provides $\theta = 48°$ coverage around T.

The experimental phantom is with a linear attenuation coefficient of $0.005mm^{-1}$ and with the side length of $20cm$ and the thickness of $2cm$. Two focus planes appear at the thickness of $0.5cm$ and $1.5cm$. On each of the planes, two cubes with the linear attenuation coefficients of $0.038mm^{-1}$ and $0.08mm^{-1}$ and with the side length of $6cm$ and the thickness of $0.25cm$ are located symmetrically. Four tiny balls are arranged vertically between the two cubes on each focus plane with the radius of $2.5mm$, $1.5mm$, $1.25mm$ and $0.56mm$, and with the linear attenuation coefficients of $0.02mm^{-1}$, $0.025mm^{-1}$, $0.05mm^{-1}$ and $0.1mm^{-1}$. The phantom is placed at $3cm$ away from the detector such that the focus planes appear at the height of 3.5cm and 4.5cm in the system. The projec-

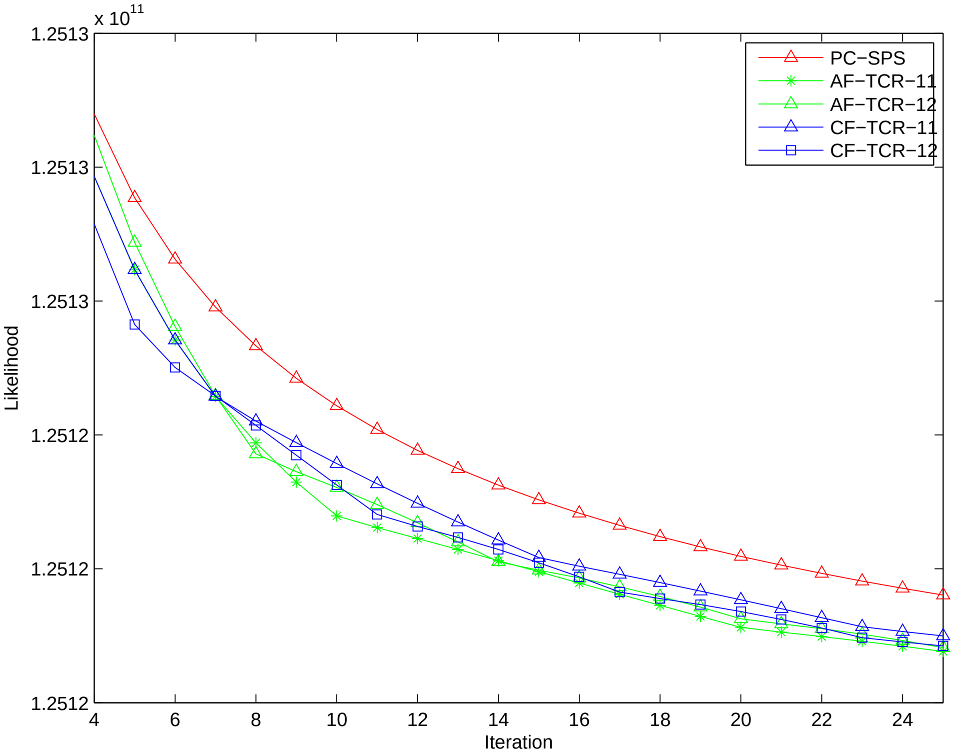

Figure 7.2. Comparisons of the objective functions of PC-SPS and proposed TCR.

tions are simulated by a ray-tracing method with additive Poisson noise. An illumination model is employed to simulate the nonuniform background.

In the first test case, images are reconstructed by PL reconstructions with PC-SPS method, AF-TCR and CF-TCR. All algorithms start from uniform initializations, and in turns iterate for 100 times. Both $a = 1.1$ and $a = 1.2$ are applied in AF-TCR and CF-TCR.

Fig. 7.2 presents the objective function for each algorithm. PC-SPS shows the slowest convergence among all. For constant factor based methods, both of them can exhibit local super-linear convergences in certain iterations. As well $a = 1.2$ produces slightly a better result than $a = 1.1$. In particular, CF-TCR-12 with 12 iterations outperforms PC-SPS with 18 iterations which produces an acceleration ratio of 1.5. For adaptive factor based methods, they produce a comparable performance with each other after 12 itera-

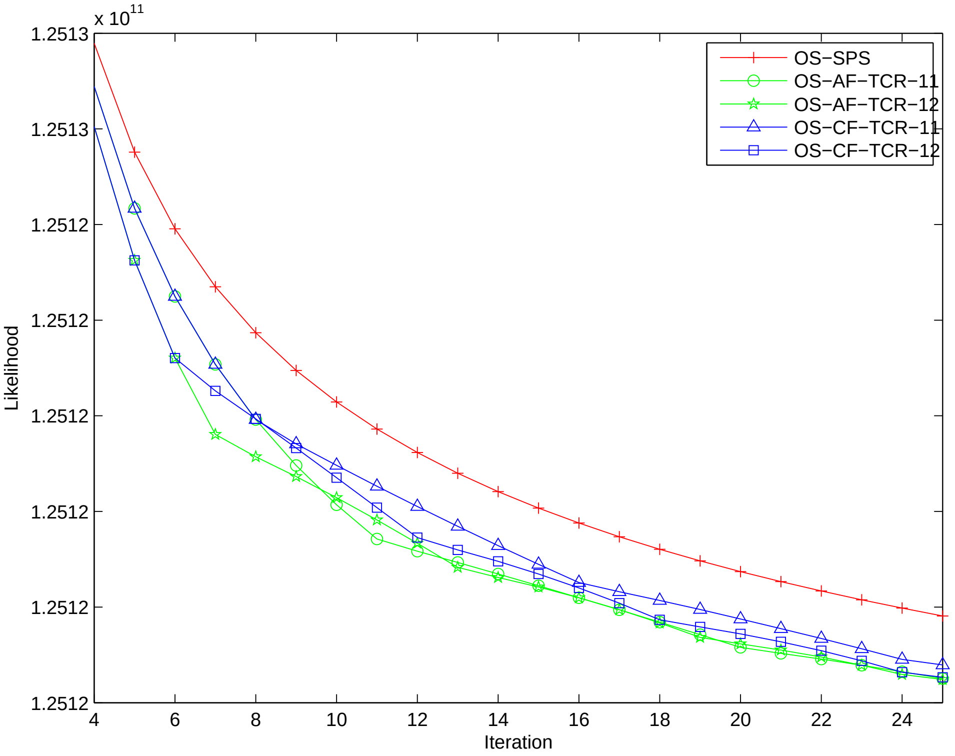

Figure 7.3. Comparisons of the objective functions of OS-blended PC-SPS and OS-blended TCR.

tions. In particular, the performance of AF-TCR-11 at 11 iterations is better than the one of PC-SPS at 18 iterations, which results in a 1.6-fold acceleration. In all, AF-TCR shows a slightly better performance than CF-ACR and with a smaller scaled factor, AF-TCR tends to gain a consistent performance, whereas CF-TCR with a larger scaled factor may yield a superior performance than the one with a smaller scaled factor.

In the second test case, OS framework is applied and is followed by each algorithm. Fig. 7.3 demonstrates the objective function of each OS initialized algorithm. Both OS-AF-TCR and OS-CF-TCR produce significant accelerations compared to OS-SPS. For OS-CF-TCR methods, $a = 1.2$ gets a better performance than $a = 1.1$. For OS-AF-TCR methods, both $a = 1.1$ and $a = 1.2$ exhibit similar results and slightly better than OS-CF-TCR methods. In particular, OS-AF-TCR-12 at the 11-th iteration produces a result which is equivalent to the one reconstructed by OS-SPS at the 18-th iteration, which presents a 1.6-fold increase.

The demonstrations above show both constant factor based methods and adaptive factor based methods can provide a superior local convergence rate. A useful strategy is summarized to chose a proper scaled factor: (1) If only few iterations are allowed, and computational cost is critical, CF-TCR with an aggressive scaled factor can be considered. (2) if the computational accuracy is critical, adaptive factor based methods with a conservative scaled factor is applicable.

7.5 PHANTOM STUDY

To demonstrate the performance of the algorithm, we compare our proposed algorithm to PC-SPS [1, 77]. Both algorithms are started by one-step OS-SPS to gain an initial speed-up. The data was collected with the sDBT prototype system [65, 82]. The origin of the 3-D coordinate system is located at the center of the detector. A flat panel detector is used for imaging acquisition. With a 140μm pixel pitch, the total image size is 2048x1661. The multiple X-ray beams are positioned along a straight line parallel to the detector plane. The source is designed to have 15 X-ray beams spanning a distance of 32.38cm from end to end. The linear spacing between the X-ray beams varies to provide an even 2° angular spacing. A 3-D breast phantom is placed on a stage with a 2.54 cm air gap. The images were acquired using: 28KVp, molybdenum filter, molybdenum target and 20mAs per projections.

Fig. 7.4 presents four sets of ROI reconstructed by ρ-OT with 5 iterations. Fig. 7.5 shows co-located ROIs reconstructed by PC-SPS with 8 iterations. One can see that our proposed algorithm with 5 iterations can produce comparable reconstructed results with PC-SPS. Although the time cost highly relies on the implementation of the algorithms, a 30% computing time was saved by our proposed method according to our current implementation.

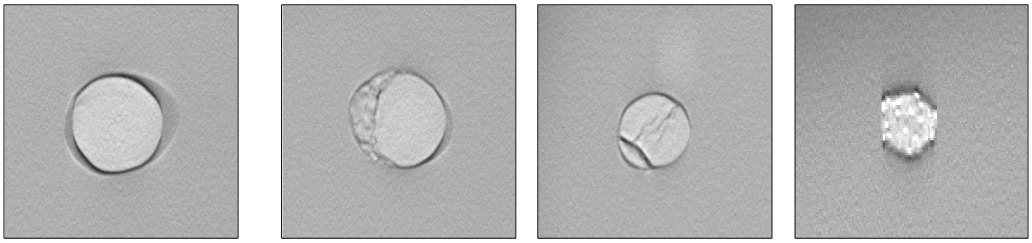

Figure 7.4. ROIs with ρ-OT with 5 iterations

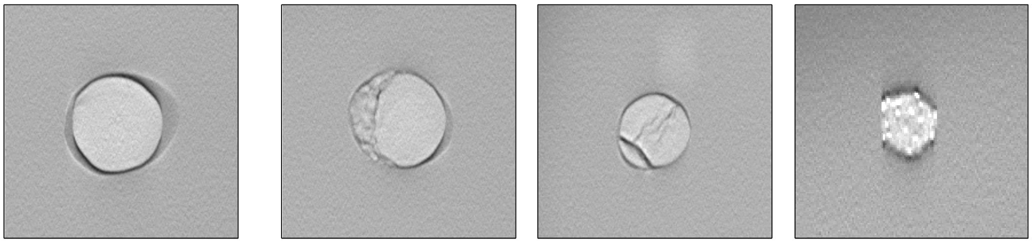

Figure 7.5. ROIs with PC-SPS with 8 iterations

7.6 DISCUSSION

A local convergence theorem was proposed with an analytical convergence rate matrix, by which the relationship between quasi-Newton method and the optimization transfer was established. Theoretical convergence analysis on MLEM method and OS-EM method were provided by applying the theory. According to the analytical results, some system-related strategies were discussed for a convergence boosting. However, system dependence is somewhat impractical. We presented a new contraction mapping with an undetermined factor instead of the original mapping of the optimization transfer. Theoretical studies showed that a careful estimation on the factor can result in the global optimal yet improved convergence. Instead of an exhausted evaluation, we proposed adaptive factor based method AF-TCR and constant factor based method CF-TCR. Both of them ensure “almost always monotonicity” instead of “bounded”, which produces a locally super-linear convergence compared to the sub-linearity of the original optimization transfer. Simulated experiments showed that both two methods outperform PC-SPS. As well, these methods can be blended with an OS framework for a boosted start. As a result, both of OS-TCRs gain superior convergence compared to OS-SPS, which implies that the hybrid methods have a tremendous potential to be an iterative method with a parallel computation, a fast convergence (sometimes locally sup-linear convergence) and comparable computational cost in each iteration.

CHAPTER 8

IMAGE QUALITY ASSESSMENT

8.1 SYSTEM DESCRIPTION

We acquire data on the stationary DBT prototype system [65, 82] to assess the performance of the proposed method. The origin of the 3-D coordinate system is located at the center of the detector. The geometry corresponds to 690 mm source to detector distance. A flat panel detector is used for imaging acquisition. With a 140μm detector element pitch, the total projection size is 2048x1661. The multiple X-ray beams are positioned along a straight line parallel to the detector plane. The source is designed to have 15 X-ray beams spanning a distance of 32.38cm from end to end. The linear spacing between the X-ray beams varies to provide an even 2° angular step size. The testing breast phantoms are placed on a stage with a 2.54 cm air gap. The projections were acquired using: 28KVp, molybdenum filter, molybdenum target and 20mAs per projections.

8.2 RECONSTRUCTIONS FOR COMPARISON STUDY

In the comparison study, we compare FBP, SART and OS MLEM (OS-EM) with the proposed statistical IR. We refer to the successively increasing over-relaxation (ρ) based OT (ρ-OT) algorithm to solve the estimation problem posed by the statistical IR (SIR) as 'SIR-ρ-OT' in the remainder of this paper. FBP based reconstruction is widely used in current commercial DBT product. Since FBP enjoys a linear response, by tuning the filter kernel a desired trade-off of resolution and noise is achievable. As a standard reference method, the filter composes of a sampling density based ramp filter [78] and a Hanning filter to remove the ring effect and the high frequency noise. The kernel is then applied on each row of projection data in the path direction of X-ray tube, then the 3D volume is reconstructed by a pixel-driven based backprojection. Iterative algorithms such as SART and OS-EM perform the reconstruction in a recursive fashion unlike the one-step operation in the FBP algorithm. During the iterative reconstruction, a 3D ray-driven model is employed for forward and backprojection and multiple iterations are needed to be convergent to the optimal solution. SART as a reference algorithm is initiated by a backprojection and turns to eight iterations, each of which is completed by going through all projections sequentially. For OS based method, it usually converges fast at the early iterations but oscillates around the global optimal solution. To gain the initial acceleration and avoid the oscillation, OS-EM is initiated by three iterations of ordered subsets in advance. Each subset composes of an individual projection. Sequentially eight iterations with full data sets are proceeding.

Our proposed statistical IR is solved by the successively increasing over-relaxation OT framework described in chapter 7, where $G(\Theta, \Theta^t)$ is the surrogate function of $\Psi(\Theta)$ in Eq. 3.2 with the gGMRF prior model. Θ_T is resolved by a OT based algorithm given in literature [6] which was derived as below:

$$\mu_j^{(n+1)} = \mu_j^{(n)} - \frac{\sum_{i=1}^{M} l_{ij}(-d_i e^{-<\mu^{(n)},l_i>} + y_i)}{\sum_{i=1}^{M}(l_{ij}\sum_{j=1}^{N} l_{ij} d_i e^{-<\mu^{(n)},l_i>})} \frac{+\lambda\kappa_j^2 \sum_{k\in N_j} \frac{p|\mu_j^{(n)}-\mu_k^{(n)}|^{p-1}}{c^p} sign(\Delta_{jk})}{+2p(p-1)\lambda\kappa_j^2 \sum_{k\in N_j} \frac{|\mu_j^{(n)}-\mu_k^{(n)}|^{p-2}}{c^p}},$$

where κ is pre-calculated before all iterations by the backprojection operation as shown in Eq. 4.8. The p and c as important parameter to control the trade-offs between the edge-preserving behavior and noise reduction have been studied in the chapter 5. λ is preset as 8 according to the discussions in the literature [3]. Three iterations with ordered subsets, each of which composes of an individual projection, is used to start up and in turn five iterations with full data sets are performed with the ρ-OT framework. One trick is noticeable in our implementation, where instead of scaling up step size for all voxels in the same manner, we only enlarge the step size of those presenting high frequency features. Therefore, the voxel update in the most changeable regions such as edges between high and low contrast and details within a complex background contributes more to the decrease of objective function value, which helps to a faster convergence in these region. Figs. 8.1 8.2, 8.3, and 8.4 illustrates focus planes with mass and

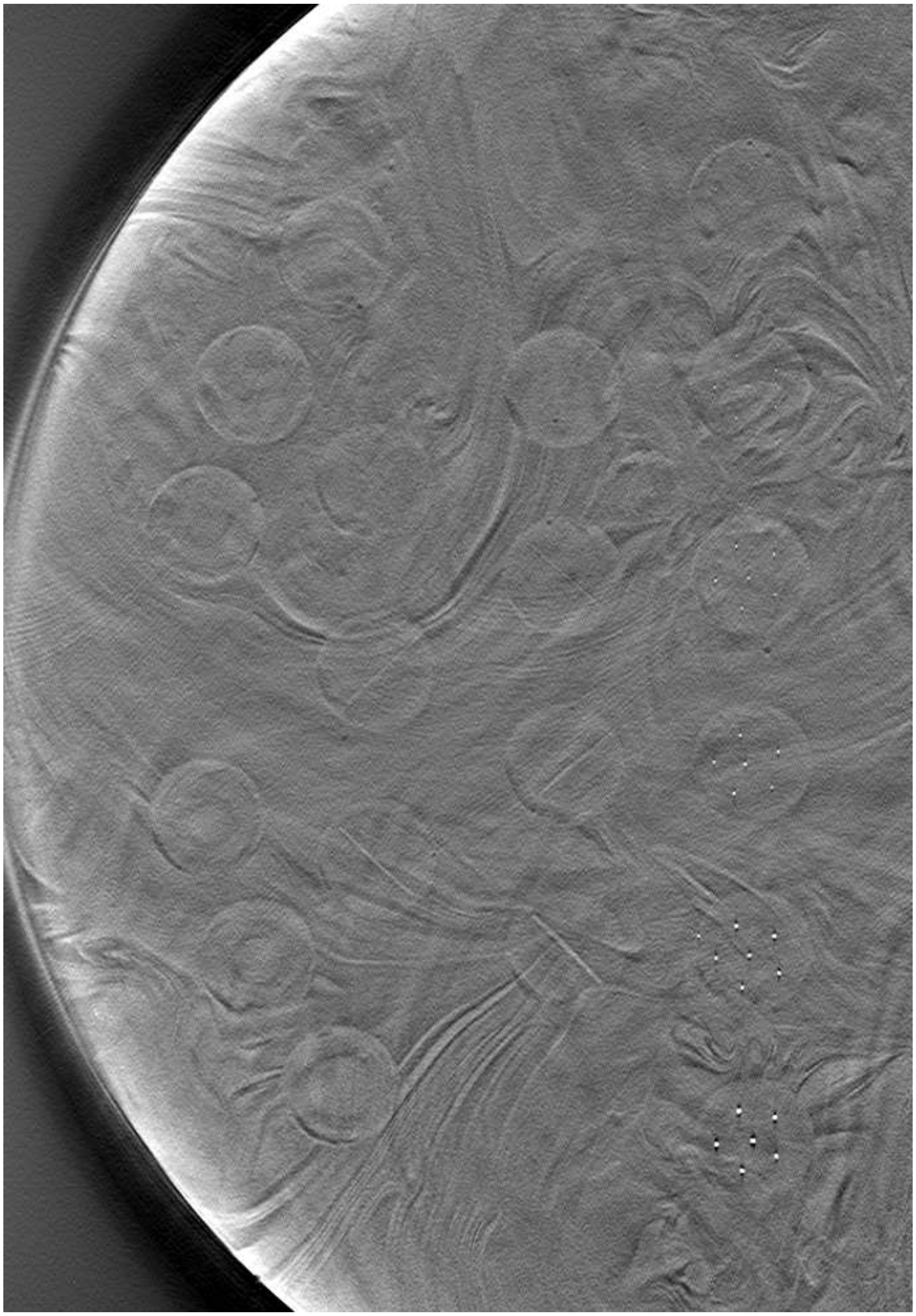

Figure 8.1. A focus plane reconstructed by FBP

micro-calcifications reconstructed by FBP, OS-EM, SIR-ρ-OT and SART with the original voxel size of 0.14 mm.

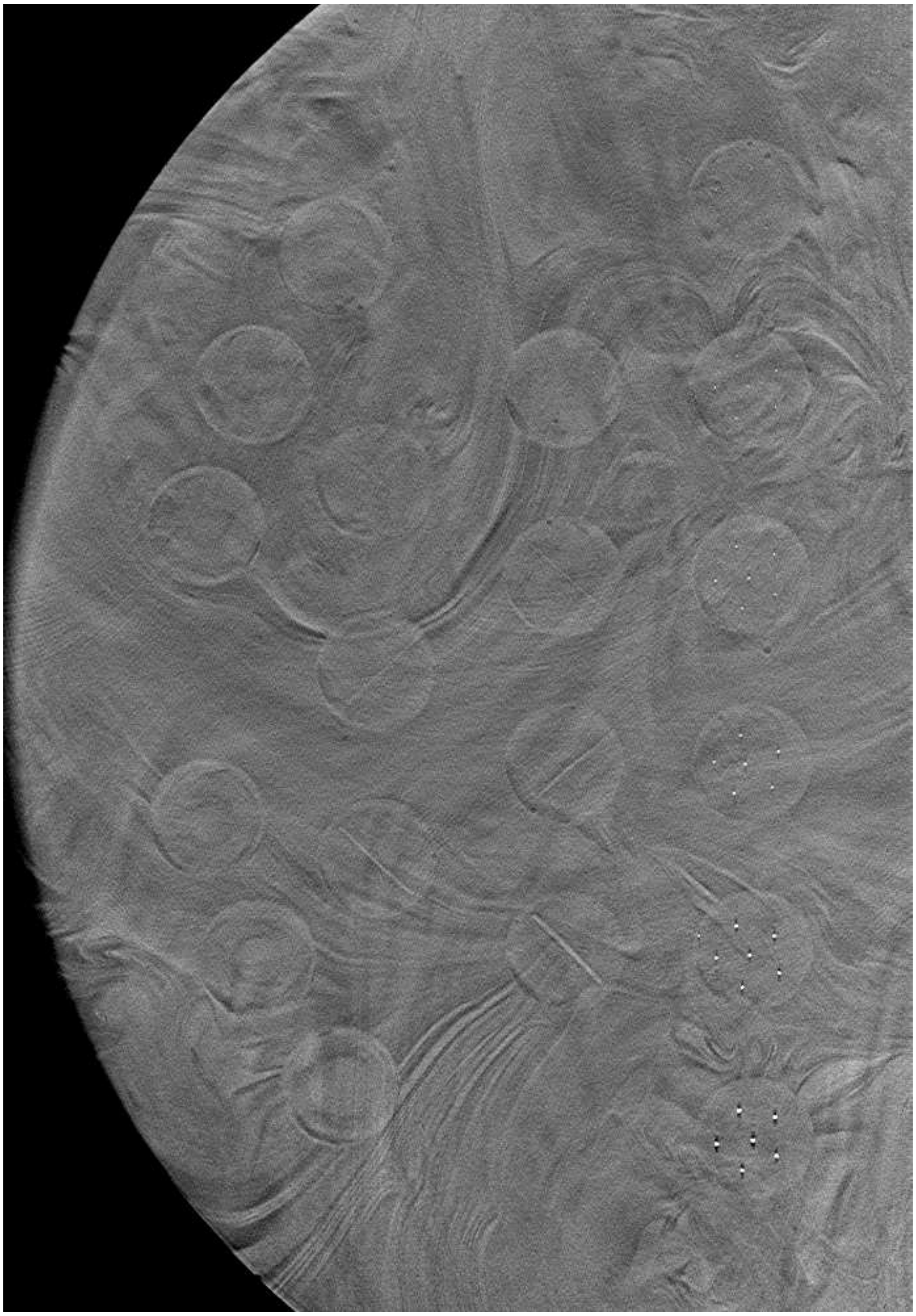

Figure 8.2. A focus plane reconstructed by OS-EM

8.3 IMPROVEMENT IN DETECTABILITY

In this section, experiments for visual detectability are conducted with the breast phantom composing of a tissue equivalent, complex, heterogeneous background, which

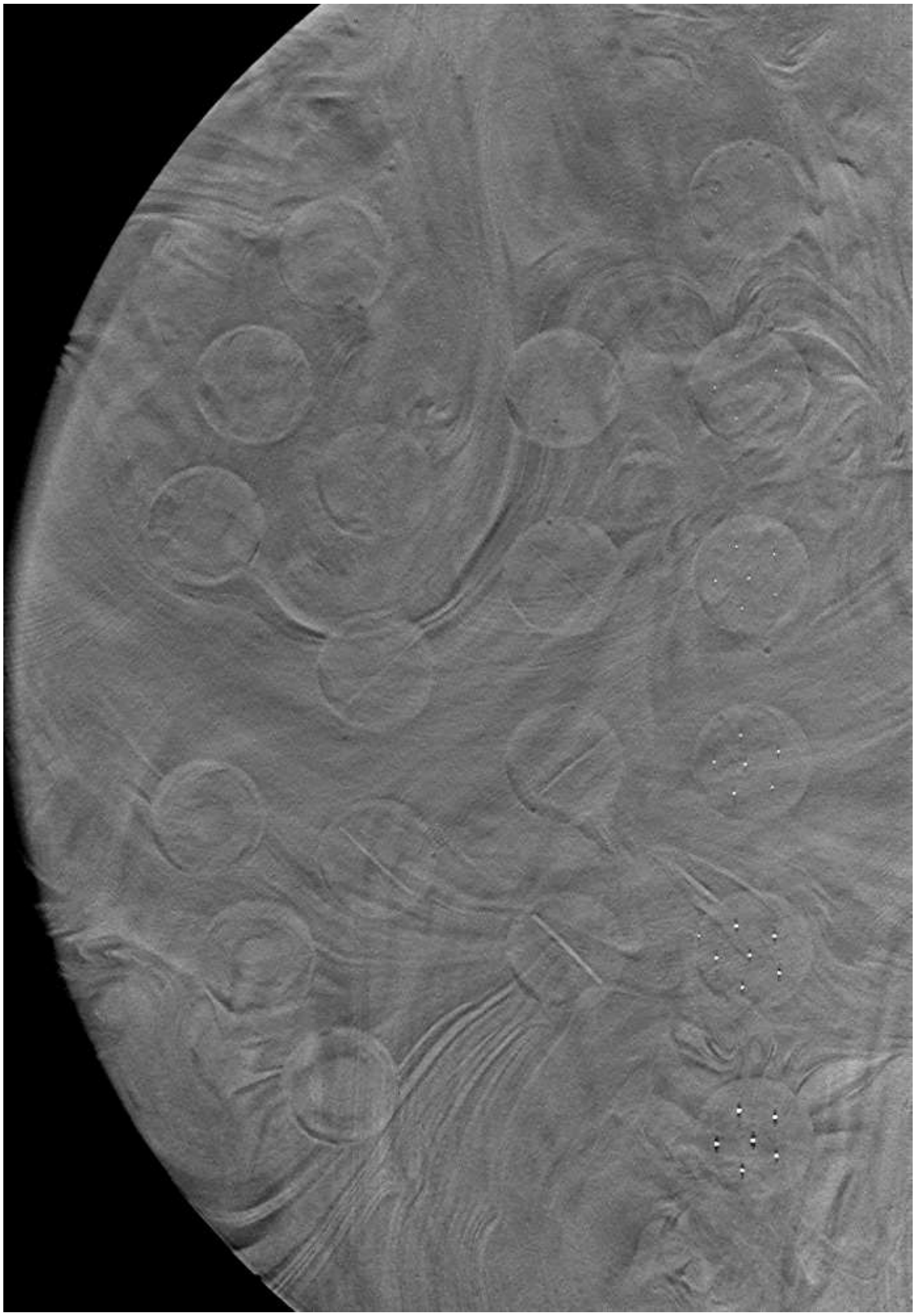

Figure 8.3. A focus plane reconstructed by SIR-ρ-OT

contains an assortment of micro-calcifications, fibrils and masses. SIR-ρ-OT reconstruction with the optimized parameters are compared against the reference methods at the

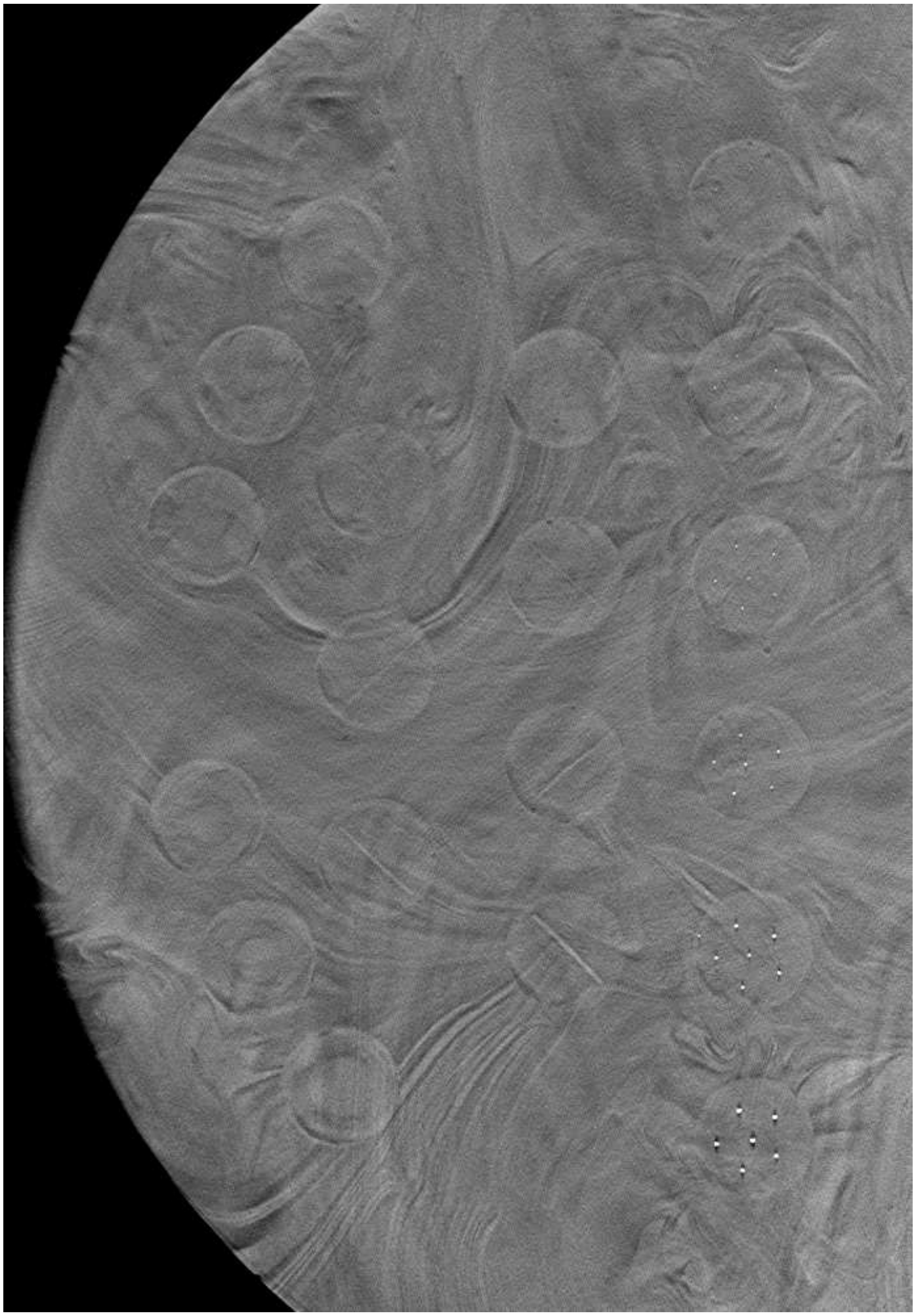

Figure 8.4. A focus plane reconstructed by SART

equal resolution. Furthermore, In order to fully demonstrate the advantage of SIR-ρ-OT, ROI reconstruction with super resolution is deployed as well. The voxel size in ROI is

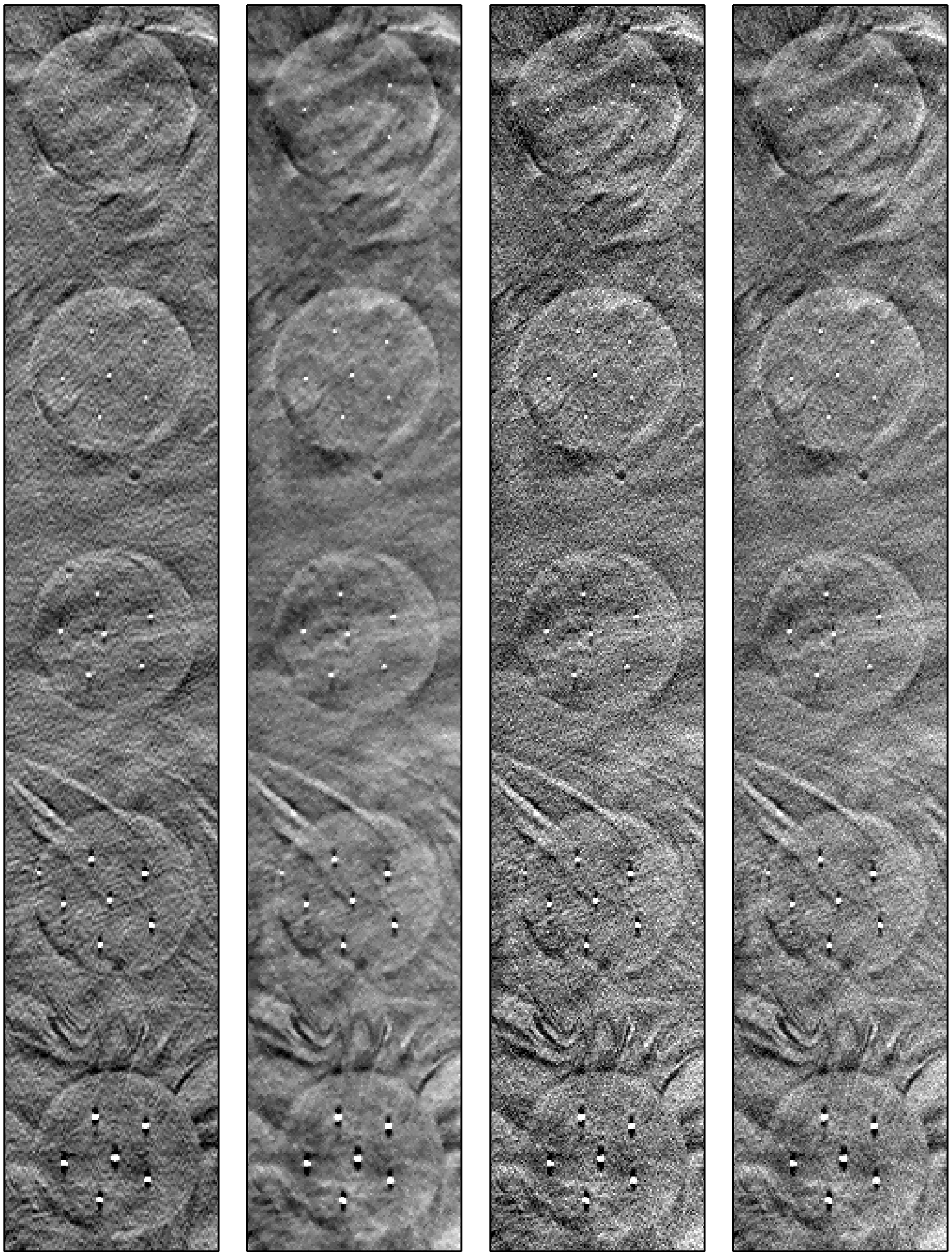

(a) (b) (c) (d)

Figure 8.5. Comparison of micro-calcification in mass reconstructed by different methods. (a) shows results reconstructed by FBP; (b) shows results reconstructed by SIR-ρ-OT; (c) shows results reconstructed by OS-EM; (d) shows results reconstructed by SART;

reduced to 0.07 mm, which is half of the original voxel size which is 0.14 mm. The reconstructed results is then compared with those with the original voxel size.

Fig. 8.5 presents the comparison of micro-calcifications in circular mass reconstructed by each method. In the first row, the six micro-calcifications in the lesion reconstructed by SIR-ρ-OT in (b) are able to be seen clearly, while they are not easily detected in the result of FBP in (a). This undetectability is caused by the limited pixel precision. Although OS-EM in (c) and SART in (d) produce the the resolution as high as the proposed method, these micro-calcifications are hidden in the noisy background. Similar situations can be observed in the second and third rows. The micro-calcifications in the forth and fifth rows are large enough to be detected among all methods.

Fig. 8.6 presents the comparison of fibrils in circular mass reconstructed by each method. All fibrils in these results are detectable. Compared with the results of FBP reconstruction in (a), SIR-ρ-OT produces clear boundary and enhanced contrast for each lesion. The results by OS-EM in (c) and SART in (d) reconstructions present relatively high noise which makes the boundaries of lesion more obscure.

Fig. 8.7 shows an image including multiple micro-calcifications embedded in a mass of a homogeneous breast phantom in a 8.4 mm ROI region. Fig. 8.7 (a) shows the SIR-ρ-OT with the voxel size of 0.14 mm. Compared with FBP reconstruction shown in Fig. 8.7 (c), it significantly reduces the noise in the soft tissue area. The image reconstructed by SIR-ρ-OT with half of the voxel size, which is 0.07 mm, is shown in Fig. 8.7 (b). Compared (b) to (a) and (c), we notice that the slowly varying area in the image presents a little higher noise than (a) but still lower than (c). The most significant difference is the reconstruction of the micro-calcifications. (b) shows sharpest edge and clearest boundary for each micro-calcifications among all competitors.

The high spatial resolution reconstruction is also applied onto the ROI with the small objects which are barely visible. Fig. 8.8 presents reconstructed image where six smaller micro-calcifications essentially locate in a circular mass in a 14 mm ROI region. Parts of these small objects are hardly observed in the results of both FBP shown in (a) and low resolution IR shown in (c). The non-visibility is mainly caused by the limited

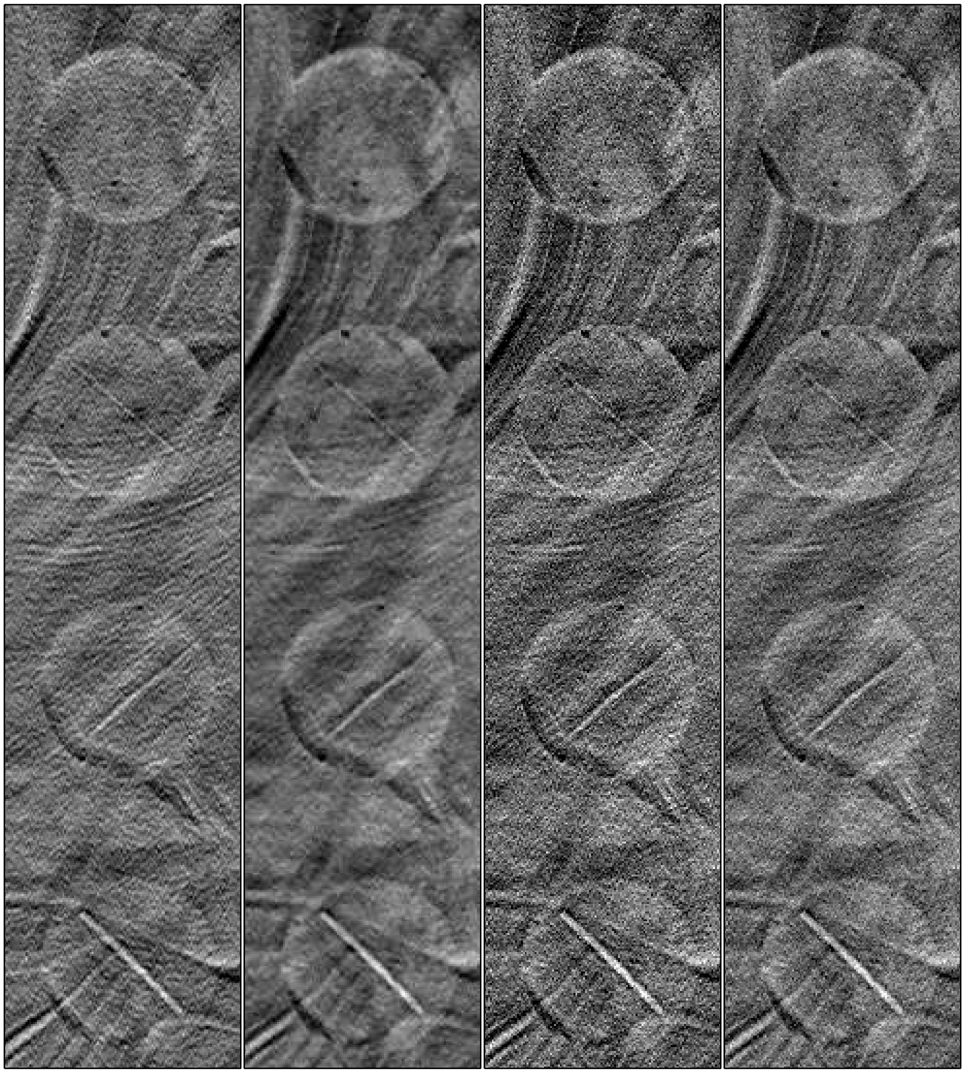

(a) (b) (c) (d)

Figure 8.6. Comparison of fibrils in mass reconstructed by different methods. (a) shows results reconstructed by FBP; (b) shows results reconstructed by SIR-ρ-OT; (c) shows results reconstructed by OS-EM; (d) shows results reconstructed by SART;

pixel precision. As shown in (b), SIR-ρ-OT with super resolution produces superior results against the other two. All of these small objects become visible. In addition, high resolution reconstruction also provides sharper and clearer boundary of the lesion.

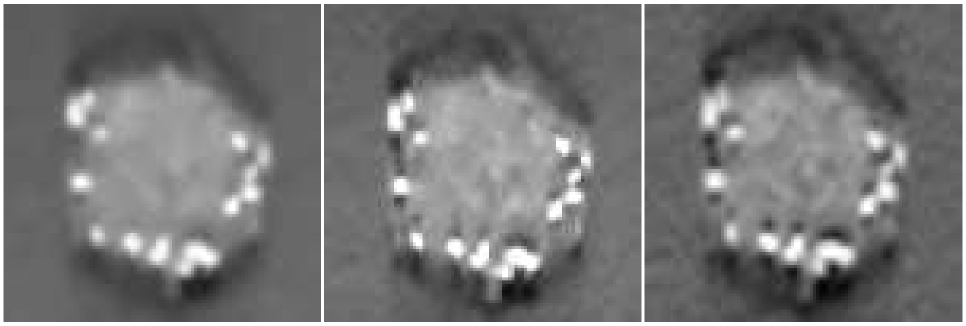

(a) (b) (c)

Figure 8.7. Zoomed focus plane with a mass and several granular micro-calcifications. (a) shows results reconstructed by SIR-ρ-OT with low resolution; (b) shows results reconstructed by SIR-ρ-OT with high resolution; (c) shows results reconstructed by FBP;

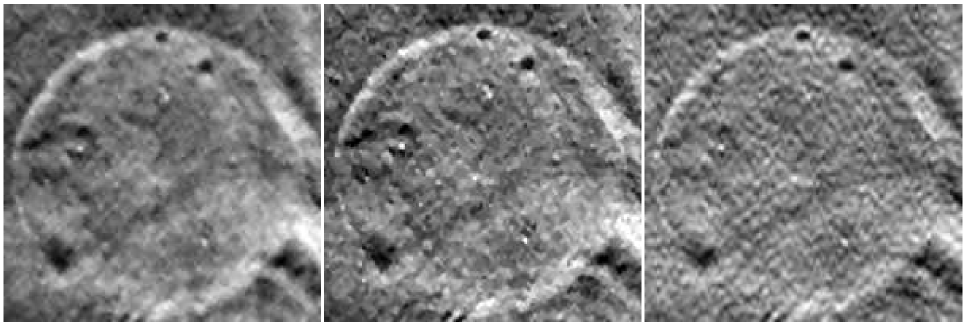

(a) (b) (c)

Figure 8.8. Zoomed focus plane with a circular mass and six tiny micro-calcifications. (a) shows results reconstructed by SIR-ρ-OT with low resolution; (b) shows results reconstructed by SIR-ρ-OT with high resolution; (c) shows results reconstructed by FBP;

8.4 PERFORMANCE FOR IN-PLANE RESOLUTION/NOISE TRADE-OFFS

For a comparison of in-plane properties at equal resolution between the reference methods and the proposed method, we reconstructed the image shown in Fig. 5.2 (a). In-plane Modulation Transfer Function (MTF) is calculated. The standard deviation of noise is measured in a homogeneous region shown in Fig. 5.2 (b). The CNR is evaluated upon the regions in Fig. 5.2 (b). Results are presented in Fig. 8.9 and Table. 8.1. The

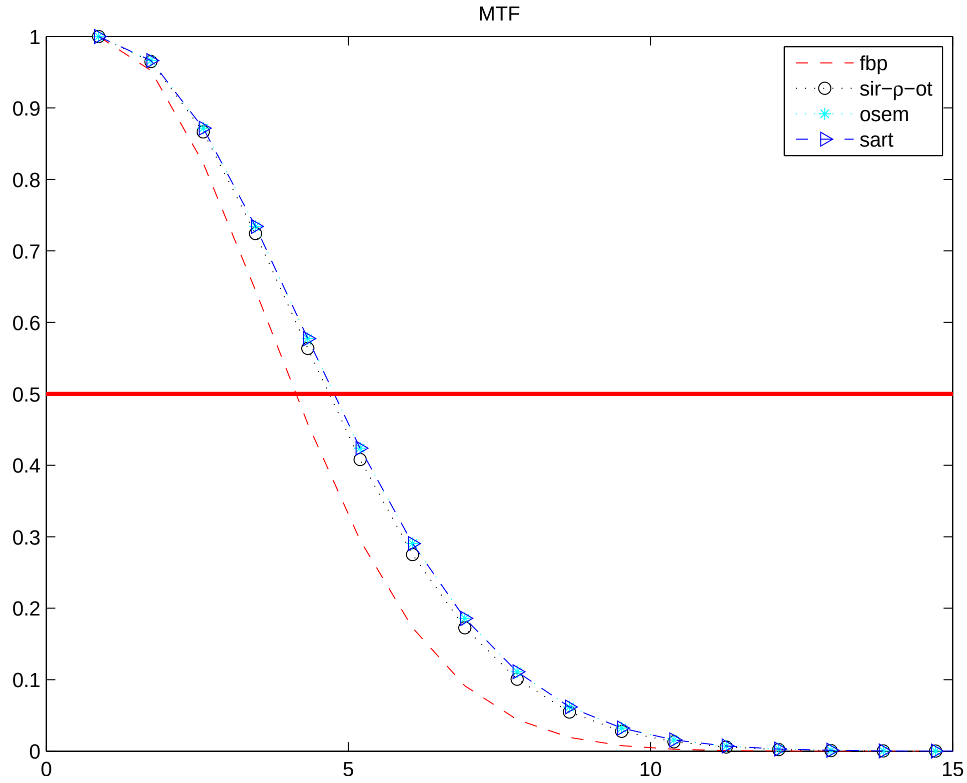

Figure 8.9. In-plane MTF measured along micro-calcification on a focus plane reconstructed by SIR-ρ-OT, FBP, SART and OS-EM

measured in-plane MTF for SIR-ρ-OT is comparable to those of the SART and OS-EM images and better than FBP image. SIR-ρ-OT present a $60 \sim 70\%$ noise reduction compared with the SART and OS-EM. For CNR comparison, one can notice that SART and OS-EM produces a similar CNR performance which is 1.7 times as much as FBP does since IR has been proven to provide a superior contrast. Overall, SIR-ρ-OT can produce the best CNR performance significantly among all methods, which is close to 1.7 times as high as the performance of SART and OS-EM and as three times as the property of FBP.

8.5 REDUCTION OF CROSS-PLANE ARTIFACTS

we calculate artifact spread function (ASF) [102] to evaluate image blur in the Z direction which perpendicular to the X-Y detector plane. ASF is defined as the ratio of

Table 8.1. Comparison of noise, CNR and in-plane MTF for SIR-ρ-OT and the reference methods

	FBP	SIR-ρ-OT	SART	OSEM
50% MTF	4.1344	4.6825	4.7655	4.7655
10% MTF	6.8362	7.8070	7.9882	7.9882
Std. Dev. (10^{-4})	7.747	6.644	18.713	17.532
CNR	2.6633	7.5906	4.5502	4.4981

the CNR values between the off-plane layer and the in-plane layer. The measurement was performed on the breast phantom with a uniform background.

Fig. 8.10 and Fig. 8.11 show the ASF curves of the selected mass and micro-calcification shown in Fig. 5.2. The layers with negative distance denote the image slices below the feature layer and vice versa. It is seen that the FBP results have strong inter-plane blurring effect for the mass object, represented by a slowly decreasing ASF curve. SIR-ρ-OT, OS-EM and SART were superior in suppressing inter-plane blurring. The corresponding ASF curves dropped quickly as the distance from the feature increased. One can notice that SIR-ρ-OT shows slightly less cross-plane artifacts than the other IRs. For micro-calcifications, all four methods have comparable ASF behaviors at the off-plane close to the in-plane layer. But the curve from FBP reconstruction tends to decrease slowly at the off-planes away from the in-plane layer, whereas the other three methods are mitigating the cross-plane artifacts quickly.

8.6 NOISE POWER SPECTRUM ANALYSIS

The Noise power spectrum analysis (NPS) is one of the most common metrics characterizing the noise property of imaging systems. The frequency-dependent NPS(f) is defined as the variance per frequency bin of a stochastic signal in the spatial frequency do-

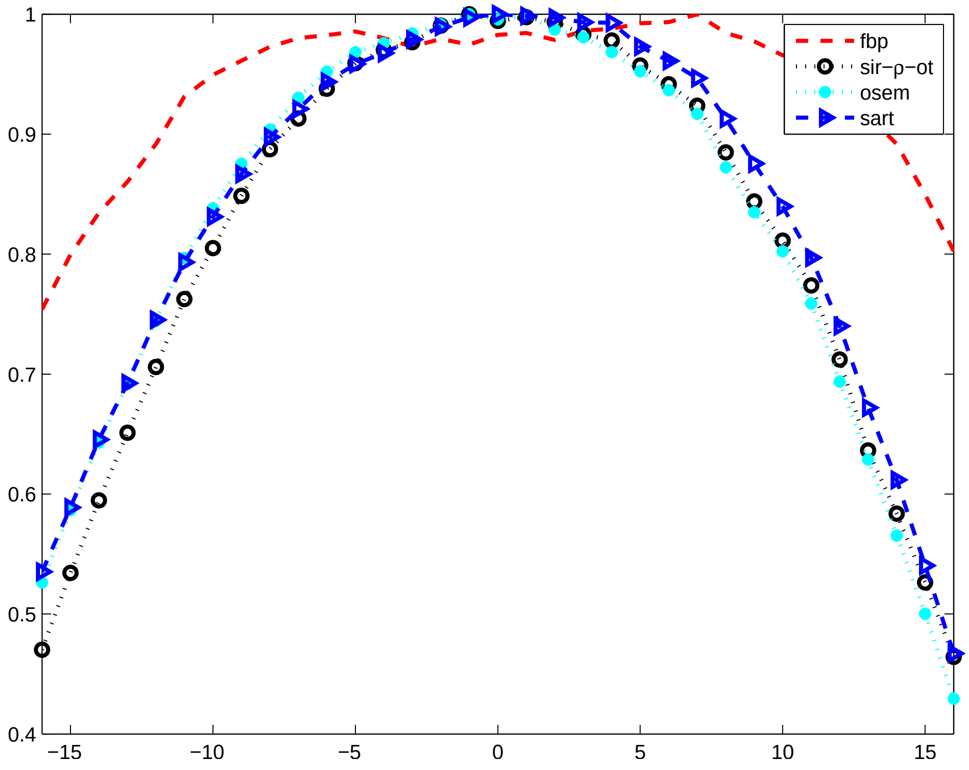

Figure 8.10. Comparison of ASF curves of the selected mass in the results reconstructed by FBP, SIR-ρ-OT, OS-EM and SART.

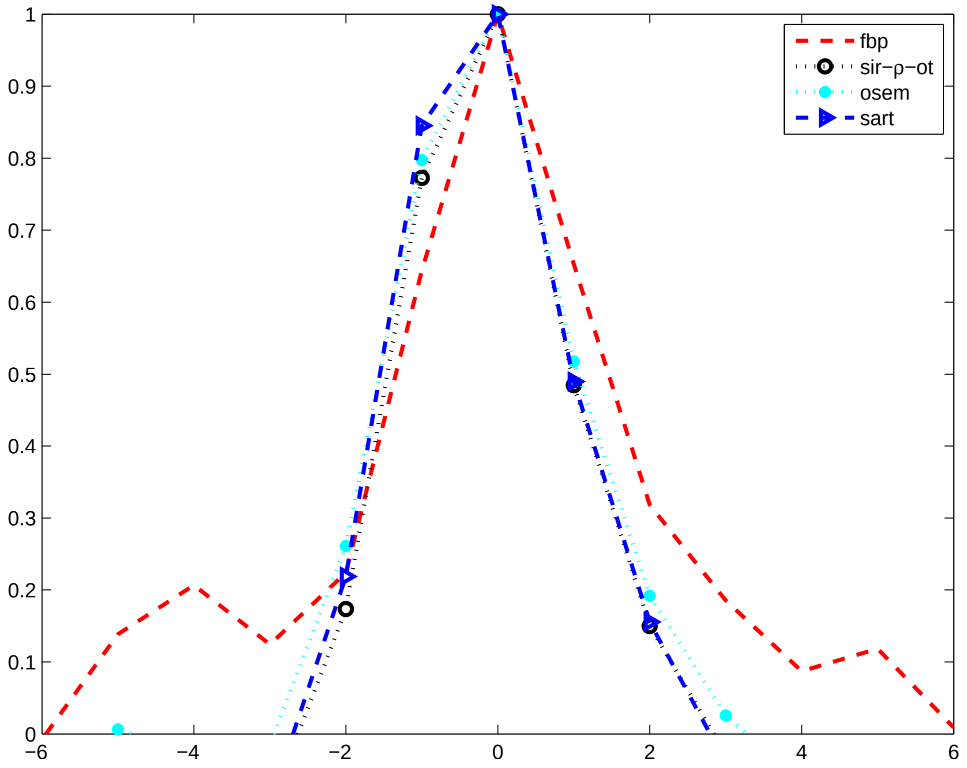

Figure 8.11. Comparison of ASF curves of the selected micro-calcifications in the results reconstructed by FBP, SIR-ρ-OT, OS-EM and SART.

main [24]. It can be directly computed from the squared Fourier amplitude of 2D imaging data as follows:

$$NPS(w_x, w_y) = \lim_{M,N,K \to +\infty} \frac{MN\Delta X \Delta Y}{K} \sum_{k=1}^{K} |FT(I(x,y) - \hat{I})|^2, \tag{8.1}$$

where, $I(x, y)$ is the image intensity at the pixel location (x, y). $\hat{I}$ denotes the global mean intensity. Operator FT means applying a discrete Fourier transformation on the difference. w_x and w_y are the spatial frequencies conjugate to x and y axes. M and N are the numbers of pixels in the x and y directions of the digital image.ΔX and ΔY are the pixel spacings in the x and y directions. And K is the number of ROIs used for analysis.

According to this equation, it is easy to implement a mean-subtracted NPS(f) measurement method. It has formed a methodology to assess the noise response of the system. In this methodology, noise propagation was evaluated by investigating the reconstructed slice images of a breast tissue equivalent phantom with the prototype system. In our experiments, a NPS measurement phantom, with the thickness of 40 mm, was placed above the surface of the detector. For each reconstruction algorithm, all the slice images with 1 mm slice thickness were reconstructed to cover the entire breast phantom. Fig. 8.12 illustrated a reconstructed plane for NPS measurement.

In NPS calculation, regions of interest (ROIs) with the size of 1024 by 1024 pixels were cut from the reconstructed planes with the same height above the detector. Each ROI was evenly divided into 8 blocks with a size of 128 by 128 pixels. For each block, a line curve fitting through the ensemble-averaged NPS estimate was used to obtain an approximation to the greatest slope of the true NPS. Finally, we extracted the frequency components from each block and formed the smoothed NPS curves.

In Fig. 8.13, the mean-subtracted NPS(f) curves for all the reconstruction algorithms are presented. We can observe that:

(1) FBP performs the best within the low-frequency noise, which is consistent to our

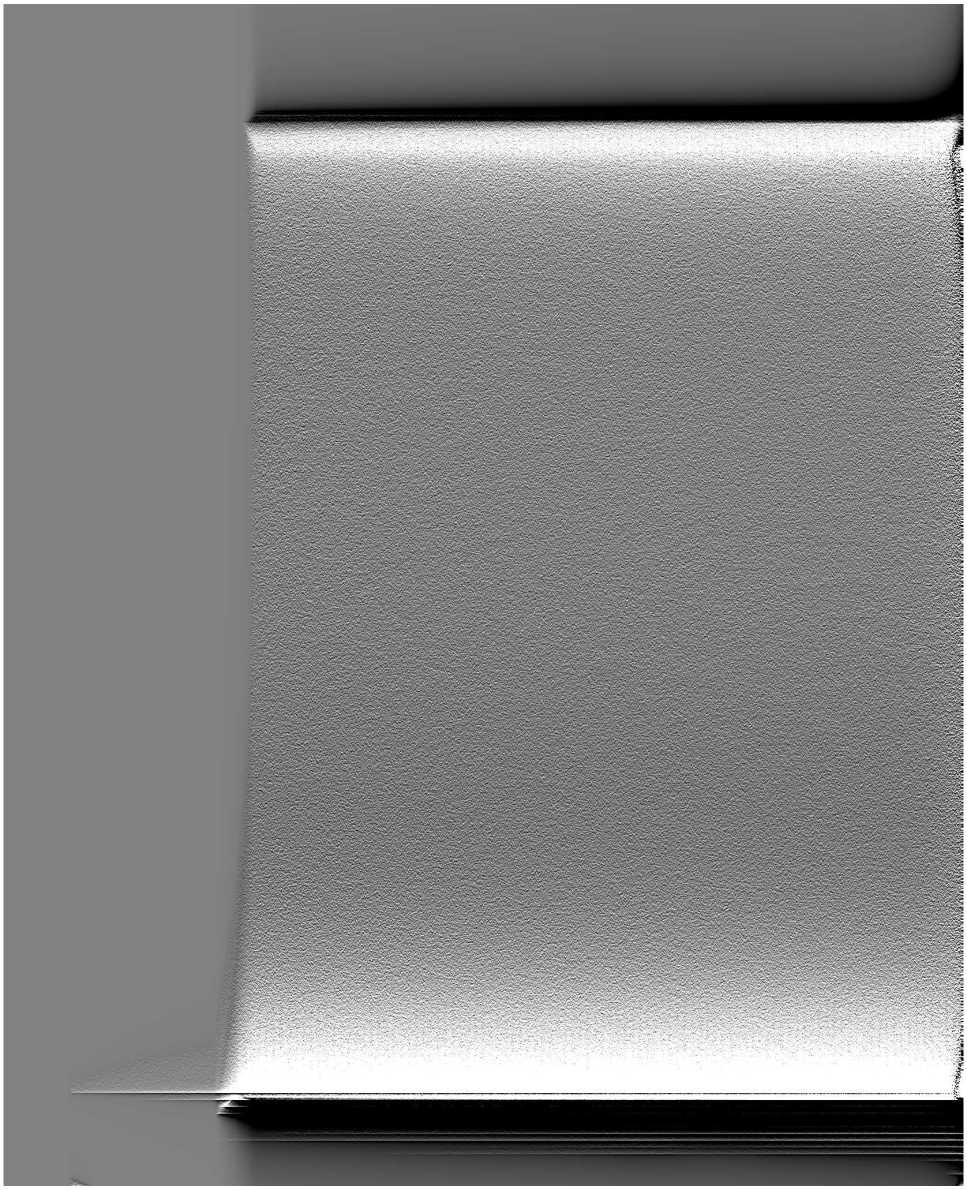

Figure 8.12. A reconstructed plane for NPS measurement

recognition that the ramp filter suppresses the low frequency and encourages the high frequency. But in our implementation, a 40% hanning low pass filter is combined with the ramp filter resulting in an acceptable noise pattern in high frequency part. (2) OS-EM and SART present a similar noise pattern in all frequency bands. The results are sensitive to iteration times, since more iterations lead to more over-fitting to the noisy data, which will present higher noise in the reconstructed results. (3) Our proposed sta-

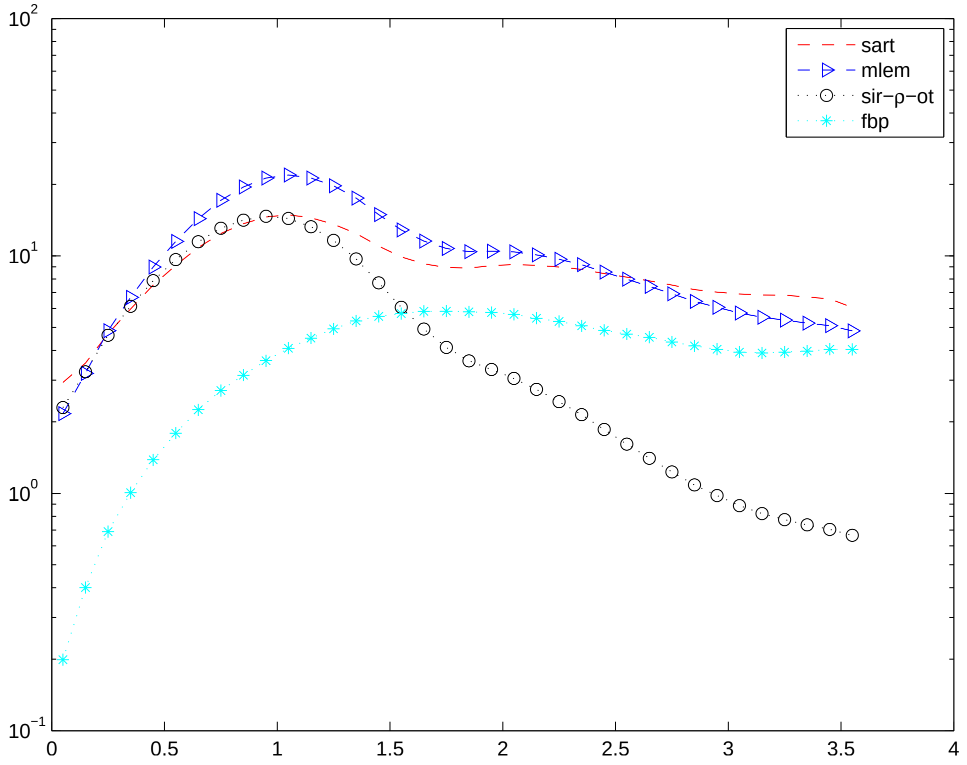

Figure 8.13. Mean-subtracted NPS analysis for different reconstruction methods

tistical IR (sir-rho-ot) demonstrates a slightly lower noise in low frequency than SART and OS-EM, but a prominent noise suppression in high frequency part compared to all other methods due to the effectiveness of the regularization.

8.7 MODULATION TRANSFER FUNCTION (MTF)

The Modulation Transfer Function (MTF) is used to analyze the resolution of imaging system in frequency domain. Technically, the resolution of a system is the minimum distance that two objects can be distinguished. In practice, an impulse function can be simulated to evaluate the response of the system or algorithm to be investigated [24].

The MTF is a handy descriptor of system spatial response because the stages of system response and reconstruction can be considered as the procedures of image degrading. Furthermore, the composite MTF of a tomosynthesis imaging system is the prod-

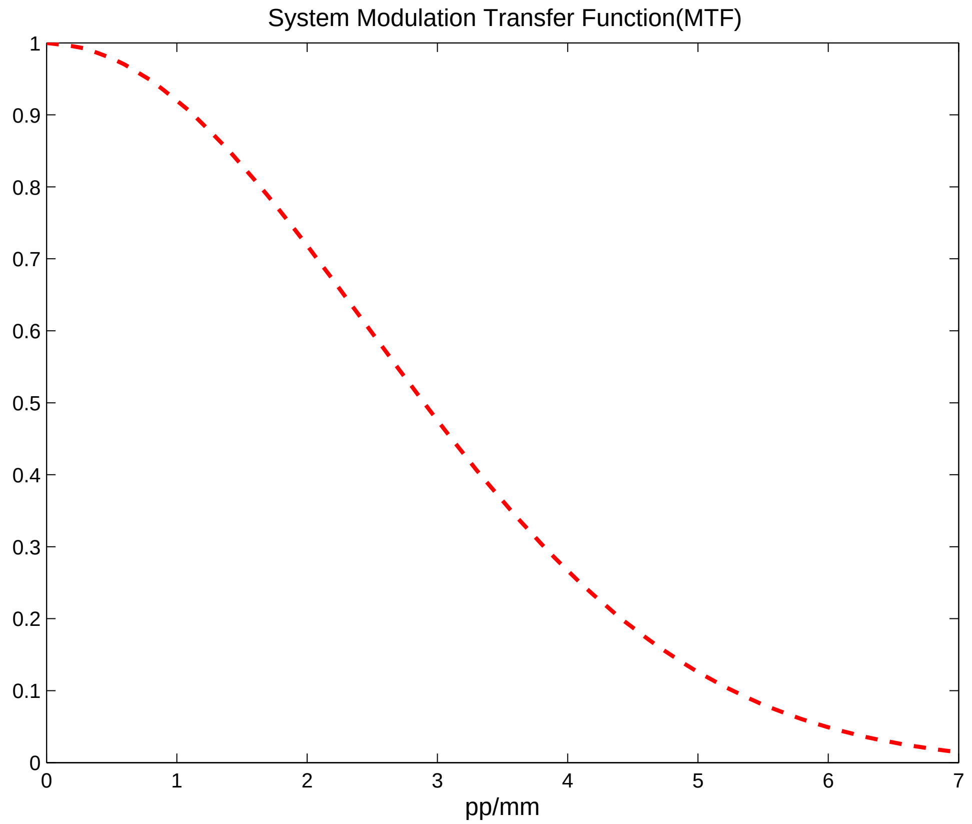

Figure 8.14. Projection MTF of the stationary Digital Breast Tomosynthesis

uct of the MTFs coming from all individual stages including both image acquisition and image reconstruction. In this section, we call the MTF from image acquisition as system MTF $MTF_{sys}(f)$ and the MTF from image reconstruction as reconstruction MTF $MTF_{recon}(f)$.

8.7.1 System MTF

In system MTF measurement, two methods, slit method and edge method, are recommended [24]. The system MTF of our stationary breast tomosynthesis prototype system was tested with a slit method. Fig. 8.14 shows the system MTF curve measured from the central projection[66].

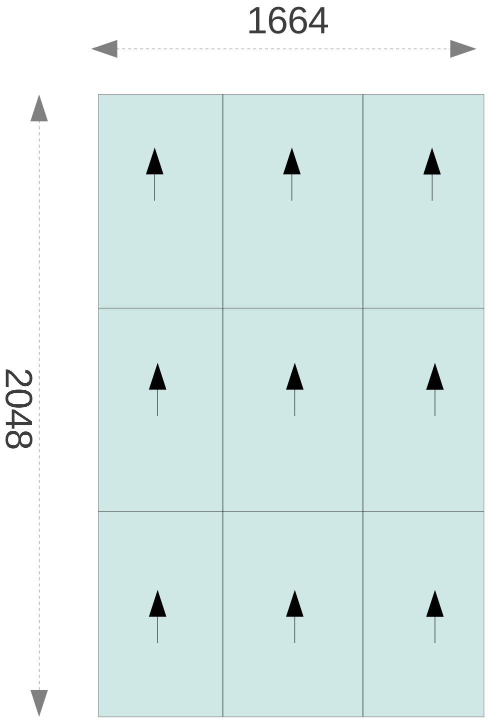

Figure 8.15. Regions of simulated impulses for relative reconstruction MTF

8.7.2 Relative reconstruction MTF

The relative reconstruction MTF describes the calculated relative MTF associated with specific algorithm and acquisition parameters. A simulated delta function was used as a standard signal input, and was projected in the proper locations on a series of simulated projection images, based on a given set of tomosynthesis acquisition parameters. A raytracing simulation method was used to project the single delta function onto the detector to simulate the tomosynthesis sequence of projection images [17]. Since the response of tomosysthesis system and reconstruction method are location-invariant, in our experiments the impulse responses at multiple locations in a reconstructed focus-plane were investigated.

Given the system geometry and image acquisition parameters described in section 8.1, datasets of projection images without background were simulated according to the delta functions with all X-ray views. Three different areas were considered and shown in

Fig. 8.15: 1) at the height of 45 mm above the detector, three impulses were located in the area close to the chest wall and individually distributed into three different regions which are top region, middle region and bottom region; 2) three impulses were located at the top, middle and bottom in the area of the central column with the height of 45 mm above the detector; 3) three impulses were located far away to the chest wall and 45 mm above the detector. During impulse simulations, if the impulse was projected onto a noninteger location on the projection, a linear interpolation among neighboring four pixels was performed to model the detector response. The simulated projection datasets were reconstructed by the representative reconstruction algorithms described in section 8.2 and the proposed statistical IR for comparison.

The 2-D Fourier transformation is then applied on each impulse region with the size of $128 * 128$. The relative reconstruction MTF along tube alignment (V) direction for the entire focus plane is calculated by averaging 1-D frequency responses along V in all regions. The relative reconstruction MTFs along V direction for each area (chest wall, central column and far-away chest wall) are respectively calculated by averaging the frequency responses of the three impulse regions in each area. The reconstructed MTF along the U direction which is perpendicular to tube alignment direction could be evaluated in a same manner. Fig. 8.16 and Fig. 8.17 demonstrate the normalized reconstruction MTF for the entire focus-plane along V direction and U direction respectively. In Fig. 8.16, one can see that most power of the frequency response for FBP reconstruction are concentrating in the frequency range of 2 4 pp/mm, and the power is low at low frequency range since the effectiveness of the ramp filter and reduced dramatically quickly at high frequency range due to the hanning filter. For the IR methods, MLEM and SIR-ρ-OT presents a similar monotonic decreasing frequency response. In the high frequency range, both MLEM and SIR-ρ-OT demonstrate superior performance than SART and FBP. Fig. 8.17 shows that along U direction, MLEM and SIR-ρ-OT still perform the best among all selective reconstruction methods. SART shows better frequency response than

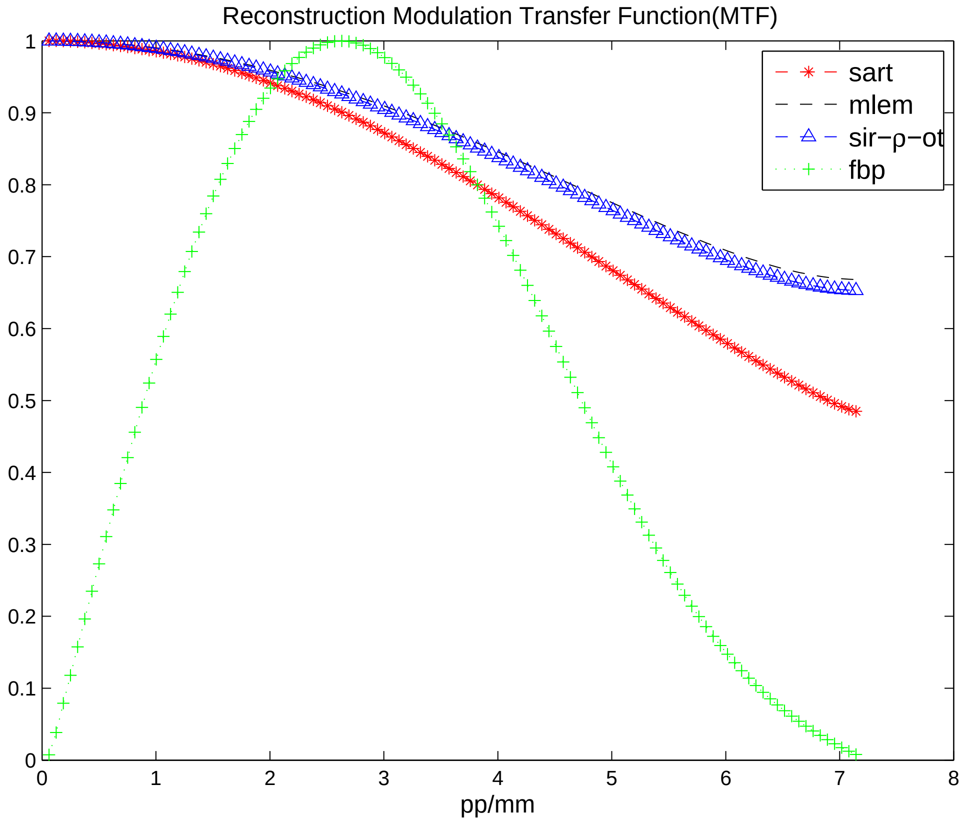

Figure 8.16. Normalized reconstruction MTF for the entire focus-plane along V direction

FBP. Because of the absence of ramp filter and hanning filter along U direction, the frequency response of FBP shows a monotonic decreasing trend. Fig. 8.18, Fig. 8.19 and Fig. 8.20 show the relative reconstruction MTFs in the area of chest wall, central column and far-away chest wall along V direction. Consistently, in all three areas, MLEM and SIR-ρ-OT demonstrate excellent frequency response, especially for the high frequency part.

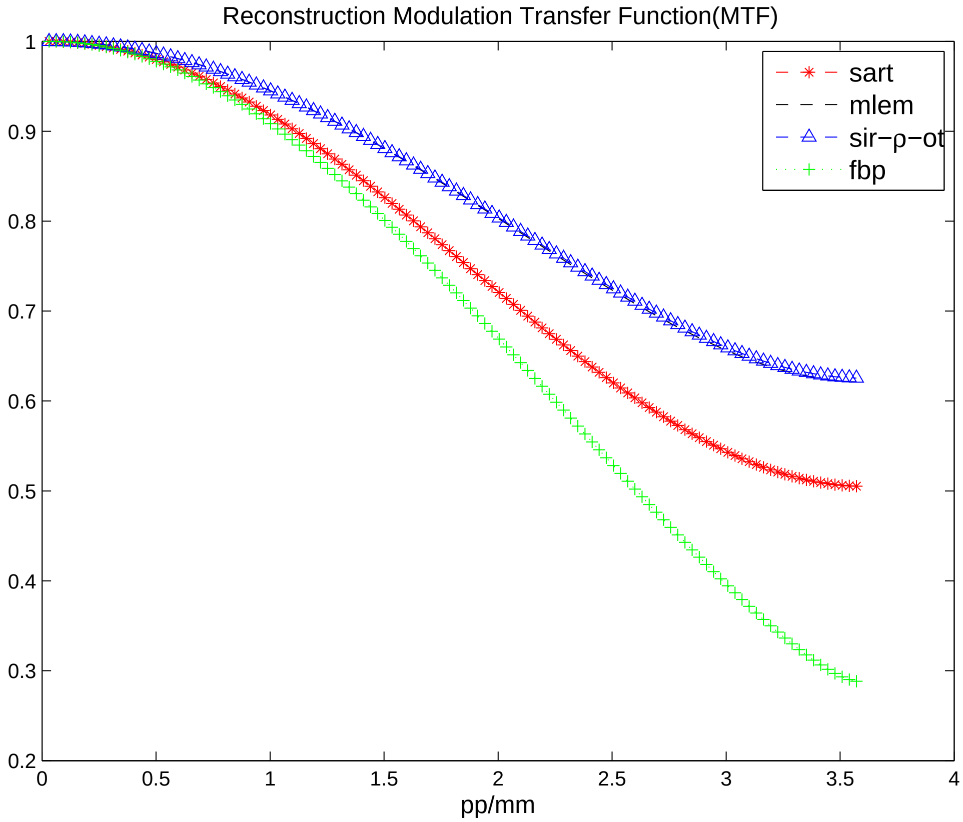

Figure 8.17. Normalized reconstruction MTF for the entire focus-plane along U direction

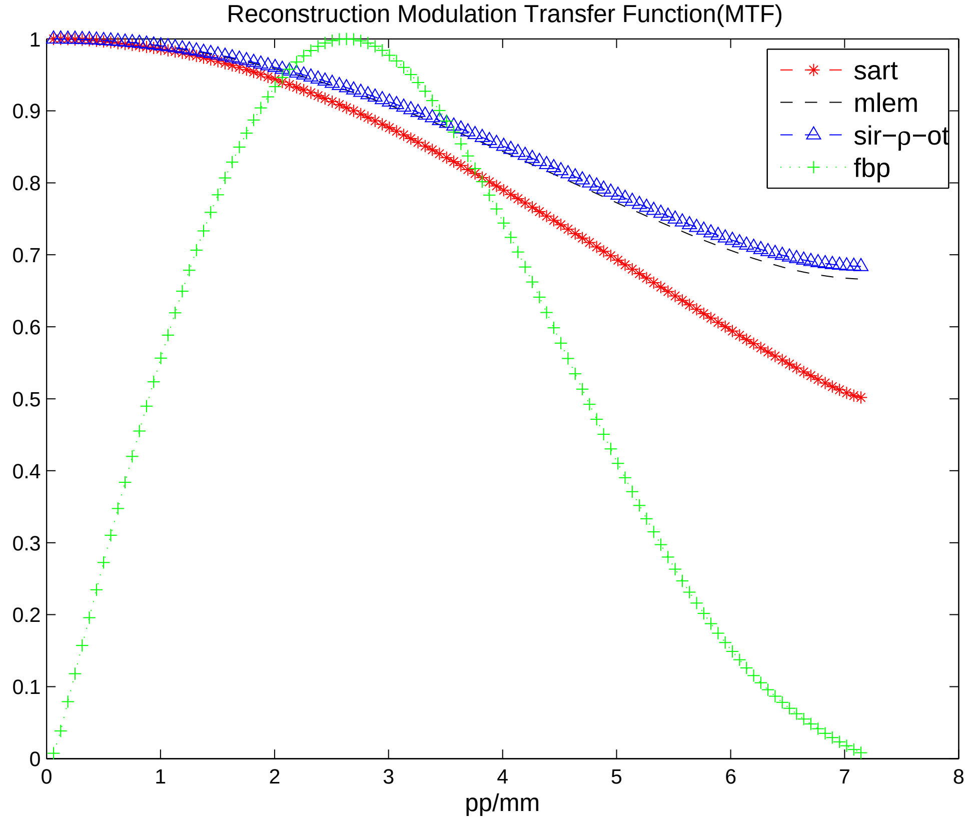

Figure 8.18. Normalized reconstruction MTF for the chest wall area along V direction

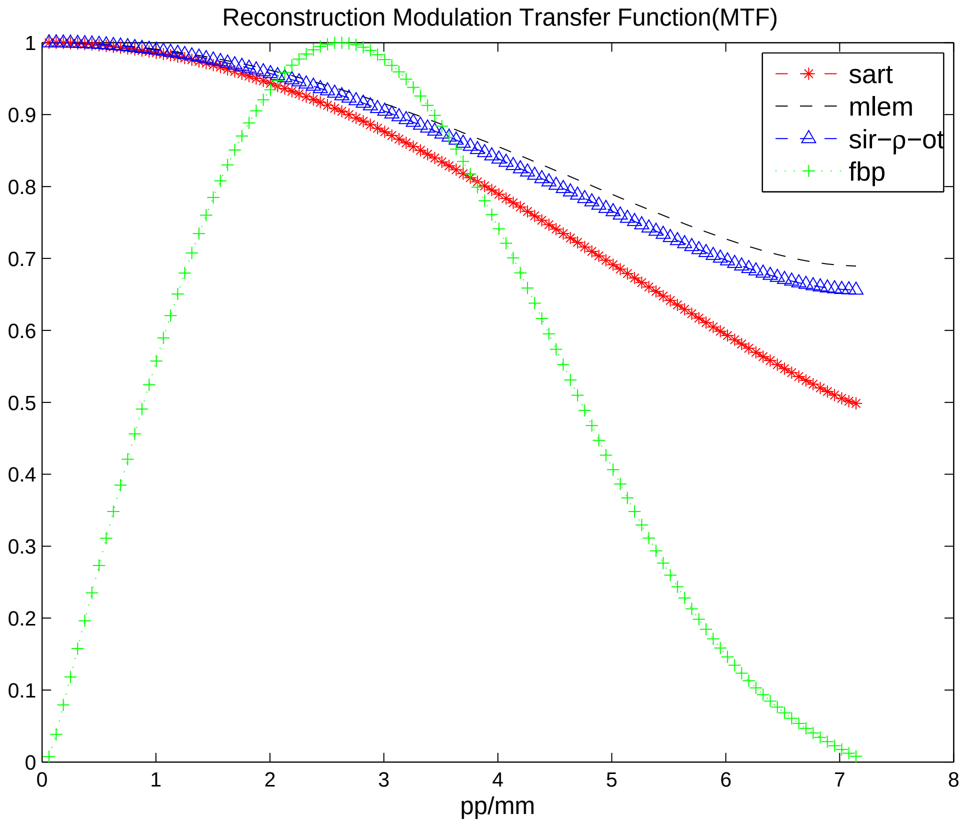

Figure 8.19. Normalized reconstruction MTF for the central column area along V direction

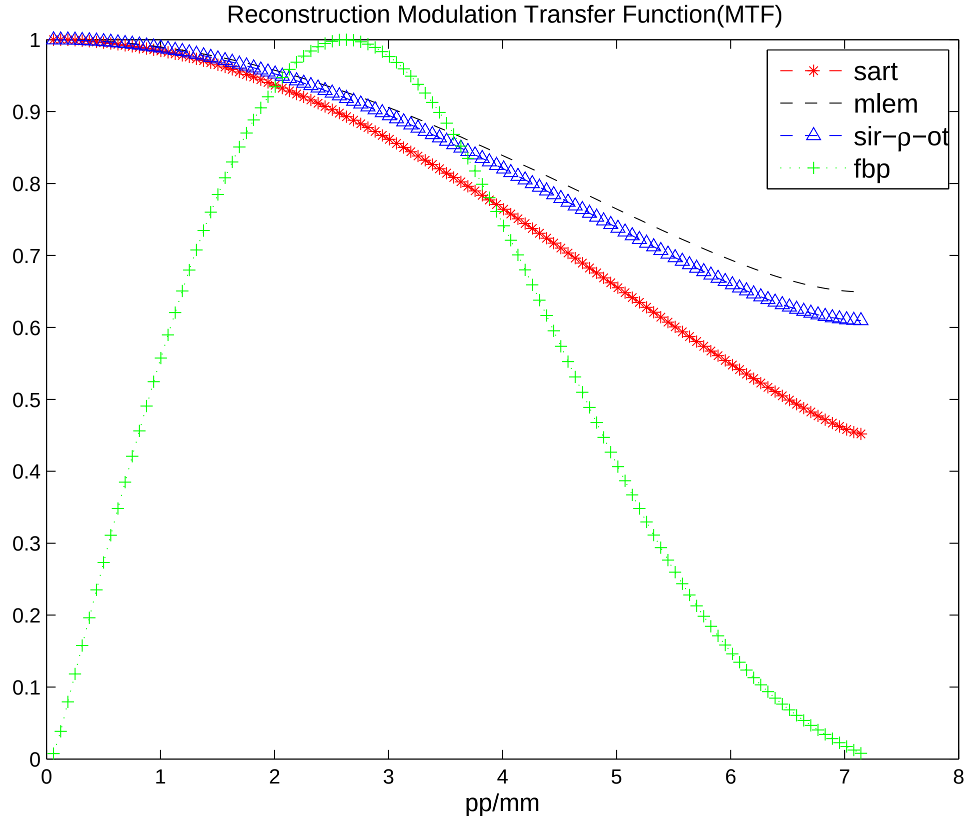

Figure 8.20. Normalized reconstruction MTF for the far-away chest wall area along V direction

CHAPTER 9

CONCLUSIONS AND DISCUSSIONS

The dissertation has focused on the theoretical studies and multiple key techniques of statistical IR for Digital Breast Tomosynthesis (DBT) image reconstruction. Several representative DBT image reconstruction algorithms were also derived, implemented and optimized. Meanwhile a comprehensive tools of image quality (IQ) assessment have been implemented and applied on the results reconstructed by different reconstruction methods. Both of these reconstruction algorithms and the IQ tools have established a thorough comparable study platform to demonstrate the pros and cons of each algorithm in DBT system. Part of these works have been documented in the literatures [9, 1, 5, 3, 2, 4, 6, 7, 8, 11, 10]. Filtered backprojection method (FBP) as a traditional deterministic reconstruction algorithm is mathematically precise upon central slice theorem in a continuous system, when the sampling rate is high enough to satisfy the Shannon Nyquist theorem. However, in DBT system, the geometric configuration has already determined that this system is with a highly incomplete sampling. FBP reconstruction with such a system could lead to serious out-of-plane artifacts, high noise and mean value shift which yields poor capability of low contrast detection. A least square method with a simple X-ray attenuation model confirming to the observed dataset is well known as Simultaneous algebraic reconstruction technique (SART). SART reconstruction applies a discrete system descriptor to model the X-ray interaction with objects, which provides the flexibility to model and improve the physical imaging process. Maximum likelihood (ML) further incorporates the photon statistics into the discrete system descriptor. Definitely both SART and ML method could improve the accuracy of reconstruction results with better low contrast detection and pixel precision. However, since X-ray system is a typical high noise modality. Noise from scattering and electric circus corrupts the datasets. Without any de-noise and correction techniques, SART and ML could lead to over-fitting to the noise data.

Statistical IR exhibits particularly promising. Recent commercial IR technique applied in computed tomography (CT), Model based iterative reconstruction (MBIR) [80, 100], significantly improves image quality (IQ) compared with conventional analytical techniques. It offers the potential of combined noise reduction, high spatial resolution, contrast enhancement and artifact reduction for low-dose imaging or enhanced image clarity for improved diagnostic confidence. These techniques are also able to be translated into statistical IR with DBT system. In particular, the likelihood part models the X-ray imaging process by confirming to the photon statistics, formalizing the interaction between X-ray and objects as well as describing the photon response of the detector. A prior model plays a very important role to provide the capability to control IQ. The generalized Gaussian Markov Random Field (gGMRF) analytical prior we introduced in our study provides necessary flexibility in its parameters to control the behavior both around the origin and at the tails of the distribution. Its parameterization through p and c is understood well enough to produce promising preliminary results. The parameter λ which controls the trade-off between the likelihood part and prior was also fully investigated based on a quadratic prior in our works where a pre-computed backprojection based regularization with the parameter κ was introduced to remove the data-dependence for a linearized impulse response. This κ was also extended to incorporate with the proposed gGMRF. The system coefficients which model the interaction between X-ray and objects were calculated by an efficient ray-driven method. The efficiency of it benefits to the computations of forward and backprojection, which are the most computational intensive parts in IR methods. Through over-sampling the detector element, the accuracy of ray-driven model for smaller voxel could be improved, which leads to the high spatial resolution reconstruction to fully develop the benefits of statistical IR. A practical solution for ROI reconstruction was applied into the high resolution technique to reduce the number of rays and the number of reconstructed voxels. This solution profoundly lowers the computational complexity and the used memory. Since IR based method still needs multiple iterations to be convergent, thereby, a relaxed order subsets (OS) framework was proposed in order to accelerate the algorithm. The relaxation used in this framework were fully studied in our study and a semi-quantitative method was presented as well to optimize the relaxation. The OS based method can not guarantee a global optimal solution even the relaxation is used. Most practical applications employ an OS based method with partial dataset followed by an optimization transfer (OT) based algorithm with full datasets in order to make sure the convergence. Thereby the convergence rate remains a particular challenge for OT based method with monotonic convergence. An efficient OT framework with a successively increasing over-relaxation was proposed according to the convergence analysis. This method potentially allows less iterations to achieve a decent IQ and an acceptable convergence.

The proposed statistical IR with these important techniques provide significant advantages over other representative methods in DBT system in terms of noise, resolution, CNR and inter-plane artifacts. In particular, noise power spectrum analysis (NPS) indicates a superior noise spectral property of our proposed statistical IR, especially in the high frequency range. With the decent noise property, statistical IR also provides a remarkable reconstruction MTF in general and in different areas in a focus plane.

Recent progress of hardware and parallel computing allows the realization of the computationally expensive statistical IR in clinical applications [9, 71, 46]. Literature [9] investigated the feasibility and efficiency of applying graphic processor unit (GPU) technique on the ML-EM image reconstruction for Positron Emission Tomography. It shows that by using the proposed parallel architecture, the computing time is significantly reduced by the factor of 40∼50. Future works will be conducted to involve the hardware acceleration for the proposed statistical IR. Combined with these computationally efficient techniques, the superior IQ provided by the proposed statistical IR will be realized to benefit the diagnostics in real clinical applications.

REFERENCES

[1] Santae Ahn and Jeffrey A. Fessler. Globally convergent image reconstruction for emission tomography using relaxed ordered subsets algorithm. *IEEE Transactions on Medical Imaging*, 22:613–626, 2003.

[2] John Amanatides and Andrew Woo. A fast voxel traversal algorithm for ray tracing. *Proceedings of EUROGRAPHICS*, 87, 1987.

[3] A. H. Andersen. Algebraic reconstruction in CT from limited views. *IEEE Transactions on Image Processing*, 8:50–55, 1989.

[4] A. H. Andersen and A. C. Kak. Simultaneous algebraic reconstruction technique(SART): A superior implementation of the art algorithm. *Ultrasonic Imaging*, 6:81–93, 1984.

[5] NORMAN A BAILV, ROBERT A KELLER, CHARLES V JAKOWATZ, and AVINASH C KAK. The capability of fluoroscopic systems for the production of computerized axial tomograms. *Investigative radiology*, 11(5):434–439, 1976.

[6] L. H. Baker. Breast cancer detection demonstration project: Fiveyear summary report. *CA: a cancer journal for clinicians*, 32(4):194–225, 1982.

[7] Harrison H Barrett and William Swindell. *Radiological imaging: the theory of image formation, detection, and processing.* Elsevier, 1996.

[8] Eric Bauer, Daphne Koller, and Yoram Singer. Update rules for parameter estimation in bayesian networks. *Proceedings of the 13th Conference on Uncertainty in Artifical Intelligence*, pages 3–13, 1997.

[9] Verrastro Belzunce and Cohen Venialgo. Cuda parallel implementation of image reconstruction algorithm for positron emission tomography. *Open Medical Imaging Journal*, 6:108–118, 2012.

[10] Mario Bertero, Tomaso A. Poggio, and Vincent Torre. Ill-posed problems in early vision. *Proceedings of the IEEE*, 76(8):869–889, 1988.

[11] Charles A. Bouman and Ken Sauer. A generalized guassian image model for edge-preserving map estimation. *IEEE Transactions on image processing*, 2:296–310, 1993.

[12] Charles A. Bouman and Ken Sauer. A unified approach to statistical tomography using coordinate descent optimization. *IEEE Transactions on image processing*, 5032:1839–1850, 2003.

[13] BreastCancer.org. Stages of Breast Cancer. `http://www.breastcancer.org`, 2012. [Online; accessed June-26-2014].

[14] Jerrold T Bushberg and John M Boone. *The essential physics of medical imaging.* Lippincott Williams & Wilkins, 2011.

[15] Emmanuel J. Candes, Justin Romberg, and Terence Tao. Robust uncertainty principles: Exact signal reconstruction from highly incomplete frequency information. *IEEE Transactions on Information Theory*, 52:489–509, 2006.

[16] Oncology Channel. Breast Cancer. `http://www.oncologychannel.com`, 2006. [Online; accessed June-26-2014].

[17] Ying Chen. *Digital Breast Tomosynthesis (DBT) - a novel imaging technology to improve early breast cancer detection: implementation, comparison and optimization.* PhD thesis, Department of Electrical Computer Engineering, Duke University, 2007.

[18] Ying Chen, Joseph Y Lo, and James T Dobbins. Impulse response analysis for several digital tomosynthesis mammography reconstruction algorithms. *Proc. SPIE*, 5745:541–549, 2005.

[19] Zang-Hee Cho, Joie P Jones, and Manbir Singh. *Foundations of medical imaging.* Wiley New York:, 1993.

[20] Yann Le Cun, Ido Kanter, and Sara A. Solla. Eigenvalues of covariance matrices: Application to neural network learning. *Physical Review Letters*, 66:2396–2399, 1991.

[21] Bruno De Man, Samit Basu, J-B Thibault, Jiang Hsieh, JA Fessier, Charles Bouman, and Ken Sauer. A study of four minimization approaches for iterative reconstruction in x-ray ct. In *Nuclear Science Symposium Conference Record, 2005 IEEE*, volume 5, pages 2708–2710. IEEE, 2005.

[22] James T Dobbins. Tomosynthesis imaging: At a translational crossroads,. *Med. Phys.*, 36(6):1956–1967, 2006.

[23] James T Dobbins and Devon J Godfrey. Digital X-ray tomosynthesis: current state of the art and clinical potential. *Phys. Med. Biol.*, 48(19):65–106, 2003.

[24] James T Dobbins III. Image quality metrics for digital systems. *Handbook of medical imaging*, 1:161–222, 2000.

[25] Idris A. Elbakri and Jeffrey A. Fessler. Efficient and accurate likelihood for iterative image reconstruction in X-ray computed tomography. *Proceedings of SPIE*, 5(3):480–492, 1996.

[26] Idris A. Elbakri and Jeffrey A. Fessler. Statistical X-ray computed tomography image reconstruction with beam hardening correction. *Proceedings of SPIE*, 4322:1–12, 2001.

[27] Idris A Elbakri and Jeffrey A Fessler. Statistical image reconstruction for polyenergetic x-ray computed tomography. *Medical Imaging, IEEE Transactions on*, 21(2):89–99, 2002.

[28] H Erdogan and Jeffrey A. Fessler. Ordered subsets algorithms for transmission tomography. *Phys. Med. Biol*, 44:2835–2851, 1999.

[29] Hakan Erdogan and Jeffrey A. Fessler. Monotonic algorithms for transmission tomography. *IEEE Transactions on Medical Imaging*, 18:801–814, 1999.

[30] Stephen A. Feig. Decreased breast cancer mortality through mammographic screening: results of clinical trials. *Radiology*, 167(3):659–665, 1988.

[31] Stephen A. Feig. Estimation of currently attainable benefit from mammographic screening of women aged 4049 years. *Cancer*, 75(10):2412–2419, 1995.

[32] LA Feldkamp, LC Davis, and JW Kress. Practical cone-beam algorithm. *JOSA A*, 1(6):612–619, 1984.

[33] Jeffrey A. Fessler. Penalized weighted least-squares image reconstruction for positron emission tomography. *IEEE Transactions on Medical imaging*, 13:290–300, 1994.

[34] Jeffrey A. Fessler. Mean and variance of implicitly defined biased estimators (such as penalized maximum likelihood): Application to tomography. *IEEE Transactions on Image Processing*, pages 493–506, 1996.

[35] Jeffrey A. Fessler. Grouped coordinate descent algorithms for robust edge-preserving image restoration. *Proceedings of SPIE*, 3071:184–194, 1997.

[36] Jeffrey A. Fessler. Iterative method for image reconstruction. Technical report, EECS Department, Univ. of Michigan. Ann Arbor, 2006.

[37] Jeffrey A. Fessler and W.Leslie Rogers. Resolution properties of regularized image reconstruction method. Technical report, Comm. and Sign. Proc. Lab., Dept. of EECS, Univ. of Michigan. Ann Arbor, 1995. in Technical Report 297.

[38] Sarah M Friedewald, Elizabeth A Rafferty, Stephen L Rose, Melissa A Durand, Donna M Plecha, Julianne S Greenberg, Mary K Hayes, Debra S Copit, Kara L Carlson, Thomas M Cink, et al. Breast cancer screening using tomosynthesis in combination with digital mammography. *Jama*, 311(24):2499–2507, 2014.

[39] JB Garrison, DG Grant, WH Guier, and RJ Johns. Three dimensional roentgenography. *American Journal of Roentgenology*, 105(4):903–908, 1969.

[40] David G Grant. Tomosynthesis: a three-dimensional radiographic imaging technique. *Biomedical Engineering, IEEE Transactions on*, (1):20–28, 1972.

[41] G Groh. Tomosynthesis and coded aperture imaging: new approaches to three-dimensional imaging in diagnostic radiography. *Proceedings of the Royal Society of London. Series B. Biological Sciences*, 195(1119):299–306, 1977.

[42] Benoit Hamelin, Yves Goussard, Jean-Pierre Dussaultand Guy Cloutier, Gilles

Beaudoin, and Gilles Soulez. Design of iterative ROI transmission tomography reconstruction procedures and image quality analysis. *Medical physics*, 37(9):4577–4589, 2010.

[43] Jiang Hsieh. *Computed tomography: principles, design, artifacts, and recent advances*. SPIE, Bellingham, WA., 2009.

[44] DoSik Hwang and Gengsheng L Zeng. Convergence study of an accelerated ml-em algorithm using bigger step size. *Phys. Med. Biol.*, 51:237–252, 2006.

[45] Christy R. Inscoe, Andrew W. Tucker, Jianping Lu, and Otto Z. Zhou. Demonstration of a scatter correction technique in digital breast tomosynthesis. *Proc. SPIE*, 8668:86680H, 2013.

[46] Xun Jia, Yifei Lou, Ruijiang Li, William Y Song, and Steve B Jiang. Gpu-based fast cone beam ct reconstruction from undersampled and noisy projection data via total variation. *Medical physics*, 37(4):1757–1760, 2010.

[47] Avinash C.. Kak and Malcolm Slaney. *Principles of computerized tomographic imaging*. Society for Industrial and Applied Mathematics, 2001.

[48] E Klotz and H Weiss. Three-dimensional coded aperture imaging using nonredundant point distributions. *Optics Communications*, 11(4):368–372, 1974.

[49] Daniel B. Kopans. *Breast Imaging*. Lippincott Williams and Wilkins, New York, 1997.

[50] Kenneth Lange, MARK BAHN, and RODERICK LITTLE. A theoretical study of some maximum likelihood algorithms for emission and transmission tomography. *IEEE Transactions on Image Processing*, MI-6:106–114, 1987.

[51] Kenneth Lange and Jeffrey A. Fessler. Globally convergent algorithms for maximum a posteriori transmission tomography. *IEEE Transactions on Image Processing*, 4(10):1430–1438, 1995.

[52] ELLIOTT C LASSER, NORMAN A BAILY, and RONALD L CREPEAU. A fluoroplanigraphy system for rapid presentation of single plane body sections. *Ameri-*

can Journal of Roentgenology, 113(3):574–577, 1971.

[53] Günter Lauritsch and Wolfgang H Härer. Theoretical framework for filtered back projection in tomosynthesis. In *Medical Imaging'98*, pages 1127–1137. International Society for Optics and Photonics, 1998.

[54] Bruno De Man and Samit Basu. Distance-driven projection and backprojection in three dimensions. *Physics in medicine and biology*, 49(11):2463, 2004.

[55] Thomas Mertelmeier, Jasmina Orman, Wolfgang Haerer, and Mithun K Dudam. Optimizing filtered backprojection reconstruction for a breast tomosynthesis prototype device. In *Medical Imaging*, pages 61420F–61420F. International Society for Optics and Photonics, 2006.

[56] Chuang Miao. *Comparative studies of different system models for iterative CT image reconstruction*. PhD thesis, Wake Forest University, 2013.

[57] Earl R Miller, Edward M MoCurry, and Bernard Hruska. An infinite number of laminagrams from a finite number of radiographs 1. *Radiology*, 98(2):249–255, 1971.

[58] Erkan U. Mumcuoglu, Richard Leahy, Simon R. Cherry, and Zhenyu Zhou. Fast gradient-based methods for bayesian reconstruction of transmission and emission pet images. *IEEE Transactions on Medical Imaging*, 13(4):687–701, 1994.

[59] M Nadjmi, H Weiss, E Klotz, and R Linde. Flashing tomosynthesisa new tomographic method. *Neuroradiology*, 19(3):113–117, 1980.

[60] Loren T Niklason, Bradley T Christian, Laura E Niklason, Daniel B Kopans, Donald E Castleberry, BH Opsahl-Ong, Cynthia E Landberg, Priscilla J Slanetz, Angela A Giardino, Richard Moore, et al. Digital tomosynthesis in breast imaging. *Radiology*, 205(2):399–406, 1997.

[61] John M Ollinger and Jeffrey A Fessler. Positron-emission tomography. 1997.

[62] Jeong Mi Park, Edmund A Franken Jr, Megha Garg, Laurie L Fajardo, and Loren T Niklason. Breast tomosynthesis: present considerations and future applications 1. *Radiographics*, 27(suppl_1):S231–S240, 2007.

[63] Alvaro De Pierro. On the relation between the ISRA and the EM algorithm for positron emission tomography. *IEEE Transactions on Medical Imaging*, 12:328–333, 1993.

[64] Etta D Pisano, Constantine Gatsonis, Edward Hendrick, Martin Yaffe, Janet K Baum, Suddhasatta Acharyya, Emily F Conant, Laurie L Fajardo, Lawrence Bassett, Carl D'Orsi, et al. Diagnostic performance of digital versus film mammography for breast-cancer screening. *New England Journal of Medicine*, 353(17):1773–1783, 2005.

[65] Xin Qian, Ramya Rajaram, Xiomara Calderon-Colon, Guang Yang, Tuyen Phan, David S Lalush Jianping Lu, and Otto Zhou. Design and characterization of a spatially distributed multibeam field emission x-ray source for stationary digital breast tomosynthesis. *Medical Physics*, 36:4389–4399, 2009.

[66] Xin Qian, Andrew Tucker, Emily Gidcumb, Jing Shan, Guang Yang, Xiomara Calderon-Colon, Shabana Sultana, Jianping Lu, Otto Zhou, Derrek Spronk, et al. High resolution stationary digital breast tomosynthesis using distributed carbon nanotube x-ray source array. *Medical physics*, 39(4):2090–2099, 2012.

[67] Johann Radon. 1.1 über die bestimmung von funktionen durch ihre integralwerte längs gewisser mannigfaltigkeiten. *Classic papers in modern diagnostic radiology*, page 5, 2005.

[68] Baorui Ren, Chris Ruth, Jay Stein, Andrew Smith, Ian Shaw, and Zhenxue Jing. Design and performance of the prototype full field breast tomosynthesis system with selenium based flat panel detector. In *Medical Imaging*, pages 550–561. International Society for Optics and Photonics, 2005.

[69] Rusian Salakhutdinov and Zoubin Ghahramani. On the convergence of bound optimization algorithm. *Proceedings of the Nineteenth conference on Uncertainty in Artificial Intelligence*, pages 509–516, 2002.

[70] Ken Sauer and Charles Bouman. A local update strategy for iterative reconstruc-

tion from projections. *Signal Processing, IEEE Transactions on*, 41(2):534–548, 1993.

[71] Holger Scherl, Benjamin Keck, Markus Kowarschik, and Joachim Hornegger. Fast gpu-based ct reconstruction using the common unified device architecture (cuda). In *Nuclear Science Symposium Conference Record, 2007. NSS'07. IEEE*, volume 6, pages 4464–4466. IEEE, 2007.

[72] Hartmut Sklebitz and J Haendle. Tomoscopy: dynamic layer imaging without mechanical movements. *American journal of roentgenology*, 140(6):1247–1252, 1983.

[73] Andrew P Smith. Fundamentals of digital mammography. *Physics, technology and practical considerations. Available from: http://www. hologic. com/oem/pdf*, 2003.

[74] Bruce D Smith. Image reconstruction from cone-beam projections: necessary and sufficient conditions and reconstruction methods. *Medical Imaging, IEEE Transactions on*, 4(1):14–25, 1985.

[75] Donald L Snyder, Carl W Helstrom, Aaron D Lanterman, Mohammad Faisal, and Richard L White. Compensation for readout noise in ccd images. *JOSA A*, 12(2):272–283, 1995.

[76] American Cancer Society. Cancer facts and figures. `http://www.cancer.org`, 2014. [Online; accessed June-26-2014].

[77] Saowapak Sotthivirat and Jeffrey A. Fessler. Relaxed ordered-subset algorithm for penalized-likelihood image restoration. *J. Opt. Soc. Am. A*, 20:439–449, 2003.

[78] Grant M. Stevens, Rebecca Fahrig, and Norbert J. Pelc. Filtered backprojection for modifying the impulse response of circular tomosynthesis. *Medical physics*, 28(3):372–380, 2001.

[79] Georg M Stiel, LSG Stiel, E Klotz, and CA Nienaber. Digital flashing tomosynthesis: a promising technique for angiocardiographic screening. *Medical Imaging, IEEE Transactions on*, 12(2):314–321, 1993.

[80] Jean-Baptiste Thibault, Ken D. Sauer, Chales A. Bouman, and Jiang Hsien. A

three-dimensional statistical approach to improved image quality for multislice helical CT. *Med. Phys*, 34(11):4526–4544, 2007.

[81] Zhen Tian, Xun Jia, Kehong Yuan, Tinsu Pan, and Steve B Jiang. Low-dose ct reconstruction via edge-preserving total variation regularization. *Physics in medicine and biology*, 56(18):5949, 2011.

[82] Andrew W. Tucker, Jianping Lu, and Otto Zhou. Dependency of image quality on system configuration parameters in a stationary dgital breast tomosynthesis system. *Medical Physics*, 40(3):031917, 2013.

[83] Henrik Turbell. *Cone-Beam Reconstruction Using Filtered Backprojection.* PhD thesis, Department of Electrical Engineering, Linkoping University, 2001.

[84] Bruce R. Whiting. Signal statistics in X-ray computed tomography. *Proceedings of SPIE*, 4682:53–60, 2002.

[85] Tao Wu. Tomographic mammography using a limited number of low-dose cone-beam projection images. *Med. Phys*, 30:365–380, 2003.

[86] Tao Wu, Richard H Moore, Elizabeth A Rafferty, and Daniel B Kopans. A comparison of reconstruction algorithms for breast tomosynthesis. *Medical physics*, 31(9):2636–2647, 2004.

[87] Shiyu Xu and Ying Chen. Compton scattering suppression based image reconstruction method for digital breast tomosynthesis. *IEEE International Workshop on Genomic Signal Processing and Statistics*, pages 190–193, 2011.

[88] Shiyu Xu and Ying Chen. An simulation based image reconstruction strategy with predictable image quality in limited-angle X-ray. *Proc. SPIE*, 8668:86685p, 2013.

[89] Shiyu Xu and Ying Chen. Local convergence analysis of the optimization transfer and its acceleration in limited view x-ray tomography. *IEEE transaction image processing*, under revision.

[90] Shiyu Xu, Ying Chen, Jianping Lu, and Otto Zhou. An application of pre-computed backprojection based penalized-likelihood image reconstruction on sta-

tionary digital breast tomosynthesis. *Proc. SPIE*, 8668:86680v, 2013.

[91] Shiyu Xu, Linlin Cong, Ying Chen, Jianping Lu, and Otto Zhou. Breast tomosynthesis imaging configuration optimization based on computer simulatio. *Journal of electronic imaging*, 23(1):013017, 2014.

[92] Shiyu Xu, Christy Redmon Inscoe, Jianping Lu, Otto Zhou, and Ying Chen. Pre-computed backprojection based penalized-likelihood (PPL) reconstruction with an edge-preserved regularizer with stationary Digital Breast Tomosynthesis. *Proc. SPIE*, 9033:903359, 2014.

[93] Shiyu Xu, Jianping Lu, Otto Zhou, and Ying Chen. An effective technique for high resolution iterative reconstruction with stationary digital breast tomosynthesis. *IEEE MIC*, under submission.

[94] Shiyu Xu, Jianping Lu, Otto Zhou, and Ying Chen. Statistical iterative reconstruction to improve image quality for Digital Breast Tomosynthesis. *Medical Physics*, under submission.

[95] Shiyu Xu, Debashish Pal, and Jean-Baptiste Thibault. An efficient technique for multi-phase model based iterative reconstruction. *Proceeding of CT meeting*, pages 343–346, 2014.

[96] Shiyu Xu, Henri Schurz, and Ying Chen. Parameter optimization of relaxed ordered subsets pre-computed back projection (BP) based penalized-likelihood (OS-PPL) reconstruction in limited-angle X-ray tomography. *Computerized Medical Imaging and Graphics*, 37(4):304–312, 2013.

[97] Shiyu Xu, Zhenxi Zhang, and Ying Chen. Statistical iterative reconstruction using fast optimization transfer algorithm with successively increasing factor in digital breast tomosynthesis. *Proc. SPIE*, 9033:90335c, 2014.

[98] M. J. Yaffe. Digital mammography. In *Handbook of medical imaging*, volume 1. SPIE, Washington, DC, 2002.

[99] Zhou Yu, Jean-Baptiste Thibault, C. A. Bouman, Ken Sauer, and Jiang Hsieh.

Edge localized iterative reconstruction for computed tomography. *Proc 10th International Meeting on Fully 3D Img Recon Radiol and Nucl Med*, 2009.

[100] Zhou Yu, Jean-Baptiste Thibault, Chales A. Bouman, Ken D. Sauer, and Jiang Hsien. Fast model-based x-ray CT reconstruction using spatially non-homogeneous icd optimization. *IEEE Transactions on image processing*, 20(1):161–75, 2011.

[101] Gengsheng L. Zeng. A filtered backprojection algorithm with characteristics of the iterative landweber algorithm. *Med. Phys*, 39(2):603–607, 2012.

[102] Yiheng Zhang. A comparative study of limited-angle cone-beam reconstruction methods for breast tomosynthesis. *Med. Phys*, 33:3781–3795, 2006.

[103] W. Zhuang, S. Gopal, and T. J. Hebert. Numerical evaluation of methods for computing tomographic projections. *IEEE Transactions on Nuclear Science*, 41(4):1660–1665, 1994.

VITA

Graduate School
Southern Illinois University

Shiyu Xu

shiyu.xu@gmail.com

Beijing Univeristy of Aeronautics and Astronautics (BUAA), China
Bachelor of Science, Applied Mathematics, June 2004

Florida International University (FIU), Beijing
Master of Science, Electrical Engineering, April 2008

Beijing Univeristy of Aeronautics and Astronautics (BUAA), China
Master of Science, Software Engineering, September 2008

Special Honors and Awards:
Won 'dissertation research award' at southern Illinois university Carbondale, 2014
Won the title of 'Excellent Graduate' at Beijing University of Aeronautics and Astronautics (BUAA), China, 2004
Won the title of 'Merit Student' for several times and People Fellowships at Beijing University of Aeronautics and Astronautics, China, 2000 $\sim$ 2008

Dissertation Paper Title:
Tomographic image reconstruction: implementation, optimization, application and comparison in digital breast tomosynthesis

Major Professor: Dr. Ying Chen

Selected publications

[1] Shiyu Xu and Ying Chen. Compton scattering suppression based image reconstruction method for digital breast tomosynthesis. *IEEE International Workshop on Genomic Signal Processing and Statistics*, pages 190–193, 2011.

[2] Shiyu Xu and Ying Chen. An simulation based image reconstruction strategy with predictable image quality in limited-angle X-ray. *Proc. SPIE*, 8668:86685p, 2013.

[3] Shiyu Xu, Ying Chen, Jianping Lu, and Otto Zhou. An application of pre-computed backprojection based penalized-likelihood image reconstruction on stationary digital breast tomosynthesis. *Proc. SPIE*, 8668:86680v, 2013.

[4] Shiyu Xu, Henri Schurz, and Ying Chen. Parameter optimization of relaxed ordered subsets pre-computed back projection (BP) based penalized-likelihood (OS-PPL) reconstruction in limited-angle X-ray tomography. *Computerized Medical Imaging and Graphics*, 37(4):304–312, 2013.

[5] Shiyu Xu, Linlin Cong, Ying Chen, Jianping Lu, and Otto Zhou. Breast tomosynthesis imaging configuration optimization based on computer simulatio. *Journal of electronic imaging*, 23(1):013017, 2014.

[6] Shiyu Xu, Christy Redmon Inscoe, Jianping Lu, Otto Zhou, and Ying Chen. Pre-computed backprojection based penalized-likelihood (PPL) reconstruction with an edge-preserved regularizer with stationary Digital Breast Tomosynthesis. *Proc. SPIE*, 9033:903359, 2014.

[7] Shiyu Xu, Zhenxi Zhang, and Ying Chen. Statistical iterative reconstruction using fast optimization transfer algorithm with successively increasing factor in digital breast tomosynthesis. *Proc. SPIE*, 9033:90335c, 2014.

[8] Shiyu Xu, Debashish Pal, and Jean-Baptiste Thibault. An efficient technique for multi-phase model based iterative reconstruction. *Proceeding of CT meeting*, pages 343–346, 2014.

[9] Shiyu Xu and Ying Chen. Local convergence analysis of the optimization transfer and its acceleration in limited view x-ray tomography. *IEEE transaction image processing*, under revision.

[10] Shiyu Xu, Jianping Lu, Otto Zhou, and Ying Chen. An effective technique for high resolution iterative reconstruction with stationary digital breast tomosynthesis. *IEEE MIC*, accepted, 2014.

[11] Shiyu Xu, Jianping Lu, Otto Zhou, and Ying Chen. Statistical iterative reconstruction to improve image quality for Digital Breast Tomosynthesis. *Medical Physics*, conditionally accepted, 2014.